HERIOT WATT UNIVERSITY

Synthesis and design of periodic mm- to nano-scale gratings and their application in antenna systems

María Lorente Crespo

Submitted for the degree of Doctor of Philosophy

School of Engineering and Physical Sciences

Heriot-Watt University

May 2017

Abstract

This thesis investigates the application of 2D periodic arrays of passive elements for future millimetre and nanometre waves antenna applications, and aims to provide guidelines for researchers dealing with the electromagnetic response of this type of structures in next generation communication systems.

Novel configurations are here reported driven by the power requirements at each frequency band, as well as adapted analysis methods for its synthesis and analysis. All-dielectric structures based on form-birefringence and gradient index optics are considered in the first part of this dissertation, for their application to highly directive circularly polarised antennas for transmission and reception of high power millimetre waves. Higher frequency nanometre waves are the focus of the second part, where the utilisation of 2D arrays of metallic nanoparticles as building blocks for optical leaky wave and magnetic antenna systems is thoroughly studied.

This thesis was fully funded by EPSRC and the School of Engineering and Physical Sciences, Heriot-Watt University.

A mis padres,

a Guillem,

a Bessel,

Acknowledgements

Firstly, I would like to thank my supervisor, Dr Carolina Mateo-Segura, for giving me the opportunity to pursue my PhD at Heriot-Watt University, as well as for her guidance and support during these years, and my second supervisor, Prof George Goussetis, for fruitful and encouraging discussions.

I would also like to thank my colleagues Ross Aitken, David Watson, Francisco Cervera, Jia Ni, Wenxing Tang, Julia Faerber, Jun Gao, Shilong Qiang, Ibrahim Alotaibi, Hassan Al Aqil, Zhou Zhou and Constantin Constantinidis for all the shared moments; and the murcianos José A. García Pérez, Salvador Mercader Pellicer, Chechu Cañavate Sánchez, Victoria Gómez-Guillamón Buendía, Pascual Hilario Re and Adrián Ayastuy Rodríguez (murciano de adopción) for filling the office with laughs and challenging questions.

Thanks to my friends from NTC Valencia Francisco J. Rodríguez Fortuño, Rubén Ortuño and Alejandro Martínez for welcoming me into this world; particularly to Carlos García Meca for his never ending patience and all his good advice. I would also like to thank Prof Nader Engheta and his group at University of Pennsylvania for their hospitality during my short stay with them, and Mikhail Odit from St Petersburg Electrotechnical University for his work and collaboration during his visit to Heriot-Watt University.

Gracias a mi familia, los que están y los que no, sobre todo a mis papás. Os quiero.

Last but not least, I would like to thank Guillem C. Ballesteros for not being just a co-author. I would not be here if it wasn't for him. And Bessel (probably not the one you are thinking about), because no one listens as he does!

ACADEMIC REGISTRY

Research Thesis Submission

Name*:*			
School:			
Version: *(i.e. First, Resubmission, Final)*		Degree Sought:	

Declaration

In accordance with the appropriate regulations I hereby submit my thesis and I declare that:

1) the thesis embodies the results of my own work and has been composed by myself
2) where appropriate, I have made acknowledgement of the work of others and have made reference to work carried out in collaboration with other persons
3) the thesis is the correct version of the thesis for submission and is the same version as any electronic versions submitted*.
4) my thesis for the award referred to, deposited in the Heriot-Watt University Library, should be made available for loan or photocopying and be available via the Institutional Repository, subject to such conditions as the Librarian may require
5) I understand that as a student of the University I am required to abide by the Regulations of the University and to conform to its discipline.
6) I confirm that the thesis has been verified against plagiarism via an approved plagiarism detection application e.g. Turnitin.

* *Please note that it is the responsibility of the candidate to ensure that the correct version of the thesis is submitted.*

Signature of Candidate*:*		Date:	

Submission

Submitted By *(name in capitals):*	
Signature of Individual Submitting:	
Date Submitted:	

For Completion in the Student Service Centre (SSC)

Received in the SSC by *(name in capitals):*			
Method of Submission *(Handed in to SSC; posted through internal/external mail):*			
*E-thesis Submitted (**mandatory for final theses**)*			
Signature:		Date:	

Please note this form should be bound into the submitted thesis.

Contents

List of Figures

List of Tables

List of Publications by the Candidate

Journal papers

[J1] M. Lorente-Crespo, G. C. Ballesteros, G. Goussetis, and C. Mateo-Segura, *Experimental validation of all-dielectric mm-wave polarization conversion based on form birefringence,* IEEE Microw. Compon. Lett. **26**(10), 759–761 (2016).

[J2] M. Lorente-Crespo, G. C. Ballesteros, G. Goussetis, and C. Mateo-Segura, *Ka-band all-dielectric multilayer metamaterial for broadband linear-to-circular polarization conversion*, in preparation.

[J3] M. Lorente-Crespo, G. C. Ballesteros, and C. Mateo-Segura, *Transparent all-dielectric gradient index waveplates with compact profiles*, Appl. Phys. Lett. **109**, 111105 (2016).

[J4] M. Lorente-Crespo, G. C. Ballesteros, and C. Mateo-Segura, *An all-dielectric circularly polarized highly directive Luneburg lens antenna*, in preparation.

[J5] M. Lorente-Crespo, and C. Mateo-Segura, *Highly directive Fabry-Perot leaky-wave nanoantennas based on optical partially reflective surfaces,* Appl. Phys. Lett. **106**, 183104 (2015).

[J6] M. Lorente-Crespo, G. C. Ballesteros, C. Mateo-Segura, and C. Garcia-Meca, *High order localized surface plasmon resonances in nanodisks,* in preparation.

[J7] M. Lorente-Crespo, L. Wang, R. Ortuño, C. García-Meca, Y. Ekinci, and A. Martínez, *Magnetic hot spots in closely spaced thick gold nanorings,* Nano Lett. **13** (6), 2654-2661 (2013).

[J8] M. Lorente-Crespo, G. C. Ballesteros, C. Mateo-Segura, and C. Garcia-Meca, *Edge Plasmon Whispering Gallery Modes in nanoholes*, submitted for publication.

[J9] M. Lorente-Crespo, and C. Mateo-Segura, *Simple closed-form solution to predict short-range surface plasmons in thin films bounded by asymmetric media and its application to hole arrays*, IEEE Photon. J. **8**(1), 1–8 (2016).

Conferences

[C1] M. Lorente-Crespo, G. C. Ballesteros, and C. Mateo-Segura, *All-dielectric Broadband Microwave Polarization Conversion based on Form Birefringence*, Advanced Electromagnetic Materials in Microwaves and Optics (METAMATERIALS), 2015 9th International Congress on, pp. 184-186, 7-12 Sept. 2015

[C2] C. Mateo-Segura, M. Lorente-Crespo, and Y. Hao, *All dielectric conformal Luneburg lens based antenna,* Antennas and Propagation (EuCAP), 2014 8th European Conference on, pp.3001-3004, 6-11 April 2014

[C3] M. Lorente-Crespo, and C. Mateo-Segura, *Analysis of 2-D periodic leaky-wave nano-antennas in the NIR,* Antennas and Propagation Society International Symposium (APSURSI), 2014 IEEE , pp. 83-84, 6-11 July 2014

[C4] M. Lorente-Crespo, G. C. Ballesteros, C. Mateo-Segura, and C. García-Meca, *Analysis of localized plasmonic resonances of nano-disk arrays*, Radio Science Conference (URSI AT-RASC), 2015 1st URSI Atlantic, pp. 1-1, 16-24 May 2015

Additional Work to this Thesis

[W1] J. Marqués, W. Tang, M. Lorente-Crespo, G. Goussetis, and M. Desmulliez, *3D printing by FDM of composites of tunable dielectric constant for high frequency devices*, ESA Industry Days Additive Manufacturing for RF/Microwave Hardware, 22-23 November 2016

[W2] M. Lorente-Crespo, and C. Mateo-Segura, *All Dielectric Flat Directive Antenna with Integrated Linear to Circular Polarisation Converter*, IET 4th Technical

Workshop on RF technology for Aerospace: Trends, Challenges and Opportunities, 06 March 2015

[W3] M. Lorente-Crespo, C. Mateo-Segura, and M. Odit, *Near field enhancement and focusing properties of multilayer arrays of plasmonics nano-ellipsoids*, Antennas and Propagation Society International Symposium (APSURSI), 2013 IEEE , pp. 116-117, 7-13 July 2013

[W4] M. Lorente-Crespo, L. Wang, R. Ortuño, C. García-Meca, Y. Ekinci, and A. Martínez, *Strong magnetic field concentration in arrays of thick gold nanorings*, 3rd Conferencia Española de Nanofotonica (CEN), 1-4 Oct. 2012

[W5] M. Lorente-Crespo, R. Ortuño, I. Alepuz-Benaches, C. García-Meca, L. Wang, Y. Ekinci, and A. Martínez, *Strong magnetism by closely spaced gold nanohoops*, Proc. SPIE 8423, Metamaterials VII, 84231V, 1 May 2012

[W6] I. Alepuz-Benaches, C. García-Meca, F. J. Rodríguez-Fortunõ, R. Ortuño, M. Lorente-Crespo, A. Griol, and A. Martínez, *Strong magnetic resonance of coupled aluminum nanodisks on top of a silicon waveguide*, Proc. SPIE 8424, Nanophotonics IV, 84242J, 30 April 2012

[W7] M. Lorente-Crespo, R. Ortuño, C. García-Meca, and A. Martínez, *Strong magnetic enhancement in the visible range by Al nanohoops*, Metamaterials, Photonic Cystals and Plasmonics (META'12), 3rd International Conference on, 19-22 April 2012

List of Acronyms

AR Axial Ratio

BTF Birefringent Thin Films

CMA Covariance Matrix Adaptation

CoP Co-Polarisation

CP Circular Polarisation

DUT Device Under Test

EELS Electron Energy Loss Spectroscopy

EMA Effective Medium Approximation

EOT Extraordinary Optical Transmission

EP Edge Plasmon

ES Evolution Strategy

FD Frequency Domain

FDTD Finite-Difference Time-Difference

FIT Finite Integration Technique

FOM Figure of Merit

FP Fabry-Pérot

FSS Frequency Selective Surface

FTIR Fourier-Transform Interferometer

GP Ground Plane

GPS Global Positioning Systems

GRIN Gradient Index

HIS High Impedance Surface

IL Insertion Loss

LL Luneburg Lens

LP Linear Polarisation

LR- Long Range

LSP Localised Surface Plasmon

LSPR Localised Surface Plasmon Resonance

LW Leaky-Wave

mm millimetre

NIR Near Infrared

PRS Partially Reflecting Surface

PEC Perfect Electric Conductor

PTFE Polytetrafluoroethylene

RF Radio Frequency

SEM Scanning Electron Microscopy

SLL Side Lobe Level

SPP Surface Plasmon Polariton

SR- Short Range

STEM Scanning Transmission Electron Microscope

TE Transverse Electric

TFM Transfer Matrix Method

TL Transmission Line

TLM Transmission Line Model

TM Transverse Magnetic

T-matrix Transfer Matrix

TFSF Total-Field Scattered-Field

VCL Virtual Current Loop

WA Wood's Anomaly

WGM Whispering Gallery Mode

XP Cross-Polarisation

A child of five would understand this. Send someone to fetch a child of five.

Groucho Marx

1 Introduction

1.1 Introduction to periodic arrays

Periodic structures play a key role in physics and engineering due to their wide applicability and theoretical importance [1]. They are frequently encountered as filters [2–4], polarisers [5–7] and polarisation rotators [8–10], in imaging [11–13], sensing [14–16], cloaking [17,18] and energy harvesting systems [19,20], among other interesting applications.

Of particular relevance is their role in antenna engineering, where arrays of radiating elements placed along a straight line, a 2D plane or in a conformal distribution can dramatically alter the antennas radiation pattern [21]. For instance, such arrays are often used to enlarge the electrical size, providing higher directivity values than the individual elements; a sought-after feature for long range communications. Examples of this are some Leaky-Wave (LW) [22,23], microstrip [24,25] and reflector antennas [26,27].

In addition, arrays offer extra degrees of freedom for tailoring the radiation characteristics. Controlling the separation between the elements of the array, the overall geometrical configuration, and/or the excitation (phase and amplitude) of the individual elements, broadens the range of specifications that can be met. For example, arrays of antennas offer enhanced beam-forming and beam-steering capabilities, adding more flexibility to signal transmission and reception [28, 29].

Having seen that periodic arrays can contribute to improving signal transfer, it is worth considering the broader scenario in which they operate. The discussion in the next section will put forward the motivation behind this thesis.

1.2 Motivation for the work

The range of services provided by telecommunication companies is continuously evolving, and so are the specifications for guaranteeing the sufficient quality of service. In this sense, current applications, e.g. multimedia and/or interactive, are much more demanding than traditional voice transfer; a problem expected to worsen even further in the future (e.g. 8K ultra HD video streaming will require higher datarates than current standards). To satisfy these needs, increasing efforts are being made for migrating the operating frequencies of next generation communication systems towards less saturated higher frequency bands of the electromagnetic spectrum. Novel technologies must be envisaged for accommodating antenna systems to this change.

The focus of this thesis is the study of 2D periodic arrays of passive elements for high frequency antenna applications, contributing to the development of future antenna systems. Even if the theory behind their general analysis and design is well known, this thesis aims to provide guidelines for researchers dealing with the electromagnetic response of 2D periodic arrays in both the mm- and nm- wavelength range. With the background and motivation laid out above, novel configurations and adapted analysis methods will be presented in the coming chapters, driven by the requirements of each frequency band, which will also be discussed in the following.

1.3 Outline of the thesis

The uniqueness of this thesis lies on the consideration of the electromagnetic properties of periodic arrays at two different frequency regimes for their application to future antenna systems. Understanding the physics behind the excitation and scattering response of mm- to nm-scale gratings is crucial and complex, as the electromagnetic response of the materials employed is generally frequency dispersive and may be dramatically different depending on the range at hand. For instance, whereas metals resemble perfect conductors in the mm-scale, their response to nm-waves is better described by a complex dielectric function. Similarly, the power handling requirements for typical mm-wave applications (e.g. satellite links) and those operating in the nm-scale (e.g. nano-antennas) differ by orders of magnitude. Per these considerations, this thesis has been structured in 7 chapters, including this introductory one, which can be grouped in two main parts; mm-waves are considered in chapters 2 and 3, whilst chapters 4-6 deal with nm-waves.

The first part of the thesis (chapters 2 and 3) focuses on mm-waves all-dielectric gratings. The literature dealing with all-dielectric gratings is rapidly growing, as suggested by Fig. 1.1. The number of publications, Fig. 1.1(a), and citations, Fig. 1.1(b), indexed in the Web of Science Core Collection [30] within the last 20 years, which include "all-dielectric" and "array" as topic terms, increased 4-fold between 2013 and 2015. This indicates the large interest this topic is attracting from the scientific community.

The singularity of this type of gratings, and the ultimate responsible for their increasing popularity, is that they can handle substantially higher powers than their metallic counterparts [31, 32], whilst addressing oxidation and corrosion problems typically associated with metals [33]. The breakdown field strength of air is 3MV/m, and for typical dielectrics such as Polytetrafluoroethylene (PTFE) or Polystyrene, it is in the 19MV/m range [34]. Therefore, the application of all-dielectric structures to antenna systems could be beneficial for long-range links typical, for instance, of satellite communications. Nonetheless, in some occasions, metallic gratings could outperform all-dielectric solutions, e.g. in terms of losses or cost, and depending on the specifications may be preferable.

Form-birefringent all-dielectric waveplates will be synthesised in chapter 2, where

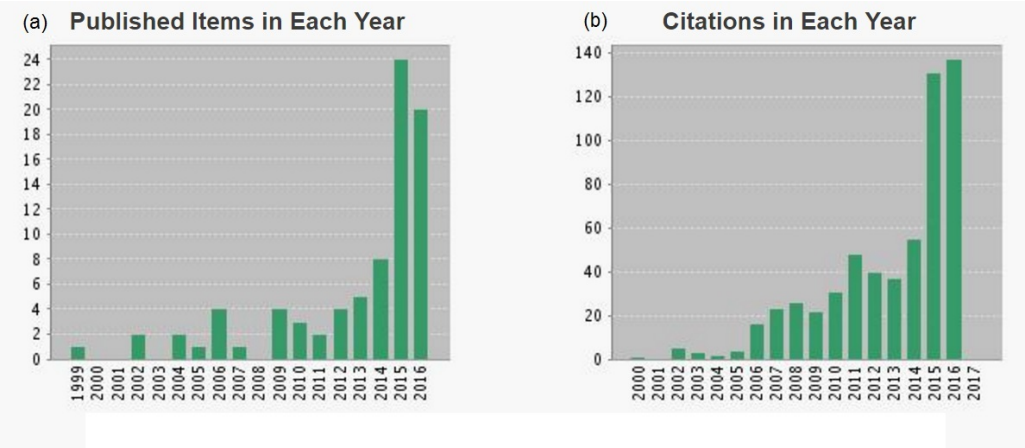

Figure 1.1: Citation report reproduced from Web of Science Core Collection reflecting (a) published items and (b) citations to source items per year [30]. Only the 20 latest years are displayed. The search criteria was based on the following TOPIC terms: "all-dielectric" and "array". Date: 15th September 2016.

the necessary theoretical framework will also be presented and discussed in thorough detail. Such novel waveplates are based on periodically cascading two homogeneous dielectric media and will find application as high purity low-loss polarisation converters, as will be suggested by the measurements reported. Lastly, a technique for increasing the bandwidth of operation of the converters, based on a multi-layer configuration, will be proposed for the first time and supported by experimental results. This innovative solution may provide an effective route towards achieving polarisation conversion without the need of complex feeds or additional circuitry, additionally benefiting from straightforward fabrication processes.

Motivated by the lack of compactness of the waveplates designed in chapter 2, a novel Gradient Index (GRIN)-based waveplate combining minimised Insertion Loss (IL) and reduced lateral dimensions will be reported in chapter 3. A simple adaptation of a classical transfer matrix formalism will be used to analyse its electromagnetic response. A potential implementation consisting of a 7-layered discretisation, will also be considered as a possible manufacturing approach, in preparation for a future practical realisation.

The second part of chapter 3 will comprise the integration of a conformal form-birefringent waveplate with a hemispherical Luneburg Lens (LL) to produce a compact circularly polarised lens antenna with remarkable beam-steering capabilities.

Such hemispherical Circular Polarisation (CP) lenses have never been proposed before. Nonetheless, the results of our initial study will suggest that this type of all-dielectric solutions hold promise for high power and robust CP long-range signal transfer.

The second part of this thesis (chapters 4-6) will analyse the electromagnetic response of 2D periodic metallic arrays operating at nm-waves, driven by the current need of increasing control over the radiation characteristics of optical sources. The design principles used for engineering similar structures at lower frequencies will be revisited to accommodate the fundamental differences in the response of materials within the nm-frequency range.

Along these lines, a Near Infrared (NIR) Partially Reflecting Surface (PRS) consisting of a planar 2D periodical distribution of metallic nano-patches will be designed in chapter 4 to be used as part of a novel miniaturised Fabry-Pérot (FP) LW nano-antenna. Our simulations will show that the high directivity and narrow beam-width typical of mm-waves LW antennas are maintained at the nm-scale, making this type of nano-antennas suitable for enhancing the extraction efficiency of optical sources. The design principles followed for designing the nano-antenna will also be summarised, emphasizing the main differences with respect to the operation of similar antennas at lower frequencies. Among these, it will be shown that the existence of unexpected bands of minimum reflectivity in the angular response of the PRS, which will be attributed to the plasmonic Brewster angle and/or localised Edge Plasmons (EPs), is particularly important as they may hinder the radiation characteristics of the nano-antenna.

EPs, as those supported by the PRS that forms part of the LW nano-antenna presented in chapter 4, will be the focus of chapter 5. There, the Localised Surface Plasmons (LSPs) supported by nano-rods, nano-disks and nano-rings will be thoroughly investigated, both for isolated nano-particles and when arranged forming 2D arrays. Whereas the literature dealing with this type of nano-particles is large, most of the published studies either focus on isolated particles, or limit to normal incidence plane-wave excitation. For their use as PRSs in LW nano-antennas, the response of 2D arrangements to obliquely incident radiation must be fully understood. A comprehensive analysis of the modes arising in such scenario was lacking in the literature and will be presented here. Three different types of modes will be

identified: a) cavity modes related to waveguide modes, b) EPs highly concentrated to the nano-particles ridges and c) FP modes. The latter are of particular interest since they can produce very high electric and magnetic field enhancements, strongly resembling magnetic loop antennas. As such, 2D periodic arrays of nano-disks or nano-rings could be envisaged as building blocks for future magnetic nano-antenna systems.

In chapter 6, the study will be extended to consider arrays of apertures on metallic films. Hole-arrays are particularly well known for exhibiting Extraordinary Optical Transmission (EOT). The first part of the chapter will focus on the study of EP-Whispering Gallery Modes (WGMs). Such modes, which will offer very narrow linewidths and high sensitivity to environmental changes, both promising features for high performance sensing, had not been reported to date.

Propagating Surface Plasmon Polaritons (SPPs), which can coexist with the localized modes, will be considered in the second part of the chapter, which comprises the derivation of a simple and accurate approximated analytical solution to the dispersion relation of Short Range (SR-) SPPs supported by thin metallic films embedded in asymmetric dielectric environments. Such a solution will be subsequently applied to calculate the frequencies at which light couples to SR-SPPs in hole arrays, and shows potential for simplifying and speeding up the design of the rapidly increasing number of SR-SPPs based devices.

Finally, the conclusions drawn from this thesis will be presented in chapter 7.

References

[1] E. Popov, *Gratings: Theory and Numeric Applications.* Presses universitaires de Provence (PUP), 2012.

[2] D. Inoue, A. Miura, T. Nomura, H. Fujikawa, K. Sato, N. Ikeda, D. Tsuya, Y. Sugimoto, and Y. Koide, "Polarization independent visible color filter comprising an aluminum film with surface-plasmon enhanced transmission through a subwavelength array of holes," *Appl. Phys. Lett.*, vol. 98, no. 9, 2011.

[3] B. E. Little, S. T. Chu, J. V. Hryniewicz, and P. P. Absil, "Filter synthesis for periodically coupled microring resonators," *Opt. Lett.*, vol. 25, no. 5, pp. 344–346, Mar 2000.

[4] H. Butt, Q. Dai, P. Farah, T. Butler, T. D. Wilkinson, J. J. Baumberg, and G. A. J. Amaratunga, "Metamaterial high pass filter based on periodic wire arrays of multiwalled carbon nanotubes," *Appl. Phys. Lett.*, vol. 97, no. 16, 2010.

[5] M. Beruete, M. N. Cía, I. Campillo, P. Goy, and M. Sorolla, "Quasioptical polarizer based on self-complementary sub-wavelength hole arrays," *IEEE Microw. Compon. Lett.*, vol. 17, no. 12, pp. 834–836, Dec 2007.

[6] J. Elliott, I. I. Smolyaninov, N. I. Zheludev, and A. V. Zayats, "Polarization control of optical transmission of a periodic array of elliptical nanoholes in a metal film," *Opt. Lett.*, vol. 29, no. 12, pp. 1414–1416, Jun 2004.

[7] X. Zhang, H. Liu, J. Tian, Y. Song, and L. Wang, "Band-selective optical polarizer based on gold-nanowire plasmonic diffraction gratings," *Nano Lett.*, vol. 8, no. 9, pp. 2653–2658, 2008.

[8] E. Doumanis, G. Goussetis, J. L. Gomez-Tornero, R. Cahill, and V. Fusco, "Anisotropic impedance surfaces for linear to circular polarization conversion," *IEEE Trans. Antennas Propag.*, vol. 60, no. 1, pp. 212–219, Jan 2012.

[9] M. Euler, V. Fusco, R. Cahill, and R. Dickie, "Comparison of frequency-selective screen-based linear to circular split-ring polarisation convertors," *IET Microwaves Antennas Propag.*, vol. 4, no. 11, pp. 1764–1772, November 2010.

[10] N. K. Grady, J. E. Heyes, D. R. Chowdhury, Y. Zeng, M. T. Reiten, A. K. Azad, A. J. Taylor, D. A. R. Dalvit, and H.-T. Chen, "Terahertz metamaterials for linear polarization conversion and anomalous refraction," *Science*, vol. 340, no. 6138, pp. 1304–1307, 2013.

[11] C. Mateo-Segura, C. R. Simovski, G. Goussetis, and S. Tretyakov, "Subwavelength resolution for horizontal and vertical polarization by coupled arrays of oblate nanoellipsoids," *Opt. Lett.*, vol. 34, no. 15, pp. 2333–2335, Aug 2009.

[12] J. Arai, F. Okano, H. Hoshino, and I. Yuyama, "Gradient-index lens-array method based on real-time integral photography for three-dimensional images," *Appl. Opt.*, vol. 37, no. 11, pp. 2034–2045, Apr 1998.

[13] Z. Liu, H. Lee, Y. Xiong, C. Sun, and X. Zhang, "Far-field optical hyperlens magnifying sub-diffraction-limited objects," *Science*, vol. 315, no. 5819, pp. 1686–1686, 2007.

[14] A. Lesuffleur, H. Im, N. C. Lindquist, and S.-H. Oh, "Periodic nanohole arrays with shape-enhanced plasmon resonance as real-time biosensors," *Appl. Phys. Lett.*, vol. 90, no. 24, 2007.

[15] E. Ekmekci and G. Turhan-Sayan, "Multi-functional metamaterial sensor based on a broad-side coupled SRR topology with a multi-layer substrate," *Appl. Phys. A*, vol. 110, no. 1, pp. 189–197, 2013.

[16] H. Im, H. Shao, Y. I. Park, V. M. Peterson, C. M. Castro, R. Weissleder, and H. Lee, "Label-free detection and molecular profiling of exosomes with a nano-plasmonic sensor," *Nat. Biotech.*, vol. 32, no. 1, pp. 490–495, 2014.

[17] B. Baumeier, T. A. Leskova, and A. A. Maradudin, "Cloaking from surface plasmon polaritons by a circular array of point scatterers," *Phys. Rev. Lett.*, vol. 103, p. 246803, Dec 2009.

[18] B. Edwards, A. Alù, M. G. Silveirinha, and N. Engheta, "Experimental verification of plasmonic cloaking at microwave frequencies with metamaterials," *Phys. Rev. Lett.*, vol. 103, p. 153901, Oct 2009.

[19] A. M. Hawkes, A. R. Katko, and S. A. Cummer, "A microwave metamaterial with integrated power harvesting functionality," *Appl. Phys. Lett.*, vol. 103, no. 16, 2013.

[20] J. Wallentin, N. Anttu, D. Asoli, M. Huffman, I. Åberg, M. H. Magnusson, G. Siefer, P. Fuss-Kailuweit, F. Dimroth, B. Witzigmann, H. Q. Xu, L. Samuelson, K. Deppert, and M. T. Borgström, "InP nanowire array solar cells achieving 13.8% efficiency by exceeding the ray optics limit," *Science*, vol. 339, no. 6123, pp. 1057–1060, 2013.

[21] C. A. Balanis, "Arrays: Linear, Planar and Circular," in *Antenna Theory: Analysis and Design*. John Wiley & Sons, 2012, ch. 6, pp. 283–384.

[22] F. Xu, K. Wu, and X. Zhang, "Periodic leaky-wave antenna for millimeter wave applications based on substrate integrated waveguide," *IEEE Trans. Antennas Propag.*, vol. 58, no. 2, pp. 340–347, Feb 2010.

[23] C. Mateo-Segura, G. Goussetis, and A. P. Feresidis, "Sub-wavelength profile 2-D leaky-wave antennas with two periodic layers," *IEEE Trans. Antennas Propag.*, vol. 59, no. 2, pp. 416–424, Feb 2011.

[24] P. S. Hall, "Multioctave bandwidth log-periodic microstrip antenna array," *IEE Proc.-H*, vol. 133, no. 2, pp. 127–136, April 1986.

[25] M. Rahman and M. A. Stuchly, "Circularly polarised patch antenna with periodic structure," *IEE P.-Microw. Anten. P.*, vol. 149, no. 3, pp. 141–146, June 2002.

[26] M. Thèvenot, A. Reineix, and B. Jecko, "A dielectric photonic parabolic reflector," *Microw. Opt. Technol. Lett.*, vol. 21, no. 6, pp. 411–414, 1999.

[27] W. Menzel, D. Pilz, and M. Al-Tikriti, "Millimeter-wave folded reflector antennas with high gain, low loss, and low profile," *IEEE Antennas and Propagation Magazine*, vol. 44, no. 3, pp. 24–29, Jun 2002.

[28] J. A. G. Akkermans and M. H. A. J. Herben, "Planar beam-forming array for broadband communication in the 60 Ghz band," *The Second European Conference on Antennas and Propagation, EuCAP*, pp. 1–6, November 2007.

[29] L. C. Godara, "Application of antenna arrays to mobile communications. ii. beam-forming and direction-of-arrival considerations," *Proceedings of the IEEE*, vol. 85, no. 8, pp. 1195–1245, Aug 1997.

[30] T. Reuters, "Web of science." [Online]. Available: http://apps.webofknowledge.com/

[31] B. W. Shore, M. D. Perry, J. A. Britten, R. D. Boyd, M. D. Feit, H. T. Nguyen, R. Chow, G. E. Loomis, and L. Li, "Design of high-efficiency dielectric reflection gratings," *J. Opt. Soc. Am. A*, vol. 14, no. 5, pp. 1124–1136, May 1997.

[32] J. H. Barton, C. R. Garcia, E. A. Berry, R. G. May, D. T. Gray, and R. C. Rumpf, "All-dielectric frequency selective surface for high power microwaves," *IEEE Trans. Antennas Propag.*, vol. 62, no. 7, pp. 3652–3656, July 2014.

[33] A. Jain, P. Tassin, T. Koschny, and C. M. Soukoulis, "Large quality factor in sheet metamaterials made from dark dielectric meta-atoms," *Phys. Rev. Lett.*, vol. 112, p. 117403, Mar 2014.

[34] R. C. Weast, M. J. Astle, W. H. Beyer *et al.*, *CRC handbook of chemistry and physics*. CRC press Boca Raton, FL, 1988, vol. 69.

If you wish to make an apple pie from scratch, you must first invent the universe.

Carl Sagan

2

Dielectric gratings as linear-to-circular polarisation converters

2.1 Introduction

The demand for continuous broadband connectivity has greatly increased in the last decade. Satellite communications have become the most appropriate infrastructure to support these needs in secluded locations (e.g. rural, suburban and remote areas) or mobile platforms such as aircraft, ships and land-based vehicles, complementing the more traditional terrestrial networks. Furthermore, the range of services offered by telecommunication providers has grown exponentially. New multimedia applications such as video-conference, interactive video-streaming, telemedicine, and distance learning require higher transmission capacity, carrier frequencies and reconfigurability than conventional voice and data transfer services. As a result, satellite communication systems are migrating towards less saturated frequency bands, such

as the Ka- (26.5–40 GHz) and Q/V-bands (35–75 GHz), allowing relatively wide frequency bandwidth and large channel capacity. However, data transmission at such high frequencies sets an extremely challenging landscape for the design of reliable propagation links. For instance, tropospheric propagation of electromagnetic waves in this frequency range is highly susceptible to precipitation and other meteorological events, which may produce random rotations of their polarisation state [1]. In that case, the signal originally intended for transmission in a certain state, Co-Polarisation (CoP), suffers partial or total power conversion into the orthogonal one, Cross-Polarisation (XP). Under these conditions, maximum power transfer between the antennas at both ends of the communication link is inhibited due to the polarisation mismatch. Combining antennas with Linear Polarisation (LP) and Circular Polarisation (CP) in the same link may alleviate this problem. Likewise, it may also prevent signal fading when antennas at both ends are misaligned. All this makes CP particularly suitable for applications where the user terminals are movable, such as in Global Positioning Systems (GPS).

Traditionally, CP has been obtained using radiators with non-canonical shapes and/or complicated feed configurations [2–5]. A simpler alternative consists in placing a polarisation converter operating in the transmit mode in front of a LP antenna, or integrating the converter with a metallic Ground Plane (GP) when operating in reflection. Polarisation converters are commonly encountered in satellite communication links [1, 6]. Likewise, they are essential components in a wide variety of applications within the Radio Frequency (RF) and microwave frequency bands of the electromagnetic spectrum [7–9]. Among these, their role in millimetre (mm) and sub-mm imaging systems for concealed weapon detection [8], environmental monitoring [10] and as isolators for protecting amplifiers [11], is particularly relevant. Nonetheless, it is in the optical range where polarisation converters –more usually referred to as waveplates in this context– have become more popular, forming part of a myriad of optical systems. These include wavelength division multiplexers [12,13], filters [14], polarimetry systems [15, 16] and displays [17], among others.

There are several alternatives to realise optical waveplates. Photonic metamaterials [18], chiral-nematic liquid-crystal films [19], or even light-emitting (active) glassy liquid-crystals [20] are among them. Here, we will focus on a more traditional approach involving birefringent uni-axial crystals [21,22]. Birefringence is the optical

property of a material having a refractive index that depends on the polarisation and propagation direction of light. Crystal birefringence arises from directionality of its crystalline structure, which results in anisotropic (directionally dependant) refractive indexes. In the simplest case, anisotropy is uni-axial, i.e. governed by a single direction: the optic axis [22]. Light propagation through uni-axial crystals is different along the optic axis than in other possible directions. Usually, waveplates are built by cutting the crystal so that the optic axis is parallel to the input and output interfaces. This results in the formation of two axes: one perpendicular to the optic axis (the extraordinary axis), and another one parallel to it (the ordinary axis). The mechanism behind polarisation conversion can be very intuitively understood by considering light as the result of the superposition of two orthogonal components, one along the ordinary axis (the ordinary ray) and another one along the extraordinary axis (the extraordinary ray). Since these two rays propagate with different phase-velocities, one will be phase-shifted with respect to the other upon transmission. As a result, the polarisation state at the output may be different to that at the input. By controlling the thickness and orientation of the waveplate, as well as the frequency of operation, the phase-delay introduced can be tailored to specific values, thus customizing the change in polarisation state.

Although there is a wide variety of crystals exhibiting birefringence in the optical range (e.g. calcite or quartz) [22], the level of birefringence available in natural media is very limited at lower frequencies. This makes the practical realisation of waveplates very challenging in the mm and sub-mm regimes. However, increased birefringence can be realised artificially at a much larger scale, form birefringence [21]. Frequency Selective Surfaces (FSSs) [10], anisotropic High Impedance Surfaces (HISs) [23] or lamellar gratings [9] may be sources of form birefringence and have been proposed to operate as polarisation converters. Most of these structures involve metallic gratings which usually suffer from power handling issues, oxidation and corrosion problems [24]. Furthermore, as the operating frequency band increases towards the Ka- or Q/V-band, the etching of the metallic layers becomes more expensive and critical, complicating substantially the fabrication process. The all-dielectric polarisation converters proposed in this chapter may overcome these limitations.

The outline of this chapter is as follows. Polarisation of electromagnetic waves and

its classification are introduced in section 2.2, together with the ratio used for discriminating among them. Isotropic and anisotropic media are introduced next, in section 2.3. There, it will also be shown how anisotropic media shall be synthesised using particular periodic arrangements of isotropic materials and their permittivity tensors retrieved via homogenization. Propagation through such form birefringent systems can be described by several analytical methods, an overview of which is available in section 2.4. Note that, although the three techniques analysed there – Jones' calculus, a transfer matrix method and Berreman's formalism– may be more commonly encountered in optics, they are equally valid in the microwave range. In section 2.5, all-dielectric form birefringent quarter- and half-plates are analytically synthesised and validated both via simulations and experimentally [J1, C1]. As discussed in sections 2.5.2 and 2.5.3, respectively, the quarter-plate exhibits excellent LP-to-CP polarisation conversion performance, whilst the half-plate acts as an efficient XP converter. In section 2.5.3, a technique for increasing the bandwidth of the converters, based on cascading waveplates with tailored thickness and orientation, is presented and validated experimentally by combining the previous quarter- and half-plates [J2]. Finally, the conclusions are summarized in section 2.8.

2.2 Polarisation of electromagnetic waves

The polarisation of an electromagnetic wave is given by the direction of its E-field. In general, when an electromagnetic wave propagates through an isotropic, homogeneous, source-free medium, the tip of its real time varying E-field vector traces an ellipse in a plane transverse to propagation. In this context, the wave is said to be elliptically polarised. LP, in which the E-field oscillates back and forth along a given direction, and CP, in which its tip traces a circle, may be simply understood as special cases of elliptical polarisation.

Without loss of generality, an electromagnetic wave propagating in the $-\hat{\rho}$ direction is considered, Fig. 2.1. Its E-field may be decomposed in two orthogonal components $\vec{E} = E_\theta\hat{\theta} + E_\varphi\hat{\varphi}$ which are given by

$$E_\theta = E_{\theta 0} \exp\left[j(\omega t - k_\rho \rho + \phi_\theta)\right] \tag{2.1}$$

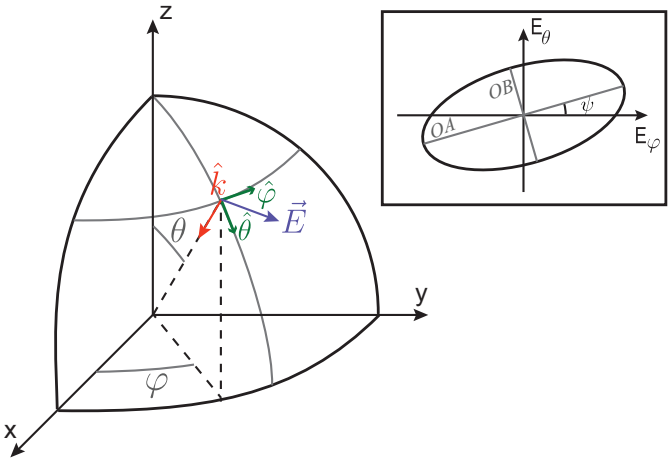

Figure 2.1: Schematic representation of an electromagnetic wave propagating in the $-\hat{\rho}$ direction of an spherical coordinate system. Inset: tilted polarisation ellipse.

$$E\varphi = E_{\varphi 0} \exp\left[j(\omega t - k_\rho \rho + \phi_\varphi)\right]. \tag{2.2}$$

In general, the polarisation ellipse of such a wave is not aligned with the coordinate axes, but tilted an angle ψ as shown in the inset of Fig. 6.13. The tilt angle can be obtained as

$$\psi = \frac{1}{2}\tan^{-1}\left(\frac{2E_{\theta 0}E_{\varphi 0}}{E_{\theta 0}^2 - E_{\varphi 0}^2}\cos\delta\right), \tag{2.3}$$

where $\delta = \phi_\theta - \phi_\varphi$ represents the phase-difference between both E-field components. Additionally, the major OA and minor OB axes of the ellipse can be written as [25]

$$OA = \left[\frac{1}{2}\left(E_{\theta 0}^2 + E_{\varphi 0}^2 + \sqrt{G}\right)\right]^{\frac{1}{2}}, \tag{2.4}$$

$$OB = \left[\frac{1}{2}\left(E_{\theta 0}^2 + E_{\varphi 0}^2 - \sqrt{G}\right)\right]^{\frac{1}{2}}, \tag{2.5}$$

where $G = E_{\theta 0}^4 + E_{\varphi 0}^4 + 2E_{\theta 0}^2 E_{\varphi 0}^2 \cos(2\delta)$. The polarisation ellipse, and therefore the polarisation state of its corresponding electromagnetic wave, is completely characterised by (2.3) and the ratio between (2.4) and (2.5). This Axial Ratio (AR)

$$AR = 20\log\frac{OA}{OB}, \tag{2.6}$$

tends to ∞ (in log-scale) for LP waves, whilst in the case of CP waves, $AR = 0$ dB. Anything in between this two values corresponds to elliptical polarisation. Therefore, the AR can be used to measure the purity of CP.

2.3 Anisotropic media

The response of a linear and homogeneous medium to electromagnetic radiation is described by its relative permittivity ϵ and relative permeability μ which are defined by the constitutive relations

$$\vec{D} = \epsilon \vec{E}, \tag{2.7}$$

$$\vec{B} = \mu \vec{H}, \tag{2.8}$$

which relate the electric and magnetic fields, $\vec{E}$ and $\vec{H}$, with the electric displacement, $\vec{D}$, and magnetic induction, $\vec{B}$. Note that the above equations are in gaussian units, i.e. $\epsilon_0 = \mu_0 = 1$ where ϵ_0 and μ_0 stand for the free-space permittivity and permeability, respectively.

However, anisotropic dielectric materials cannot be described in terms of a simple permittivity parameter. Instead, each component of $\vec{D}$ may be a function of every component of $\vec{E}$, and the relationship (2.7) must be replaced by the following three equations [21]

$$D_x = \epsilon_{xx} E_x + \epsilon_{xy} E_y + \epsilon_{xz} E_z, \tag{2.9}$$

$$D_x = \epsilon_{yx} E_x + \epsilon_{yy} E_y + \epsilon_{yz} E_z, \tag{2.10}$$

$$D_x = \epsilon_{zx} E_x + \epsilon_{zy} E_y + \epsilon_{zz} E_z. \tag{2.11}$$

The nine permittivity terms in (2.9)-(2.11) form a second rank tensor of the form

$$\tilde{\epsilon} = \begin{bmatrix} \epsilon_{xx} & \epsilon_{xy} & \epsilon_{xz} \\ \epsilon_{yx} & \epsilon_{yy} & \epsilon_{yz} \\ \epsilon_{zx} & \epsilon_{zy} & \epsilon_{zz} \end{bmatrix}, \tag{2.12}$$

and (2.9)-(2.11) may be expressed in a more compact notation as

$$\vec{D} = \tilde{\epsilon}\vec{E}. \tag{2.13}$$

Similarly, the magnetic induction in tensor form reads

$$\vec{B} = \tilde{\mu}\vec{H}, \tag{2.14}$$

where $\tilde{\mu}$ simplifies to the identity matrix in our case.

2.3.1 Form birefringence and effective medium approximation

Crystal birefringence may be explained in terms of anisotropy at the atomic level. However, anisotropy may also arise at larger scales, e.g. when considering arrangements of similar isotropic particles whose dimensions are much smaller than the free-space wavelength. This artificial birefringence is known as *form birefringence* [21].

A simple example of form birefringence is considered in the following. The structure under investigation is shown in Fig. 2.2. It consists of a 1D periodic assembly of thin planar sheets made of isotropic dielectrics with permittivity values ϵ_1 and ϵ_2, and widths w_1 and w_2. In the metamaterial regime, i.e. when the period is much smaller than the wavelength ($w_1 + w_2 \ll \lambda$), the electromagnetic characteristics of such a structure can be described using an Effective Medium Approximation (EMA) [21]. In this case, electromagnetic waves interact with the assembly as they would with a bulk homogeneous effective medium. Note that the equivalent medium is uni-axial, i.e. there is one privileged direction defining the optic axis of the crystal.

In the simplest case, the waveplate has its optic axis aligned with the coordinate axes. In this scenario, the dielectric tensor of the effective medium is diagonal. A waveplate with its optic axis parallel to the x-axis is depicted in Fig. 2.2(a). The permittivity tensor in this case is

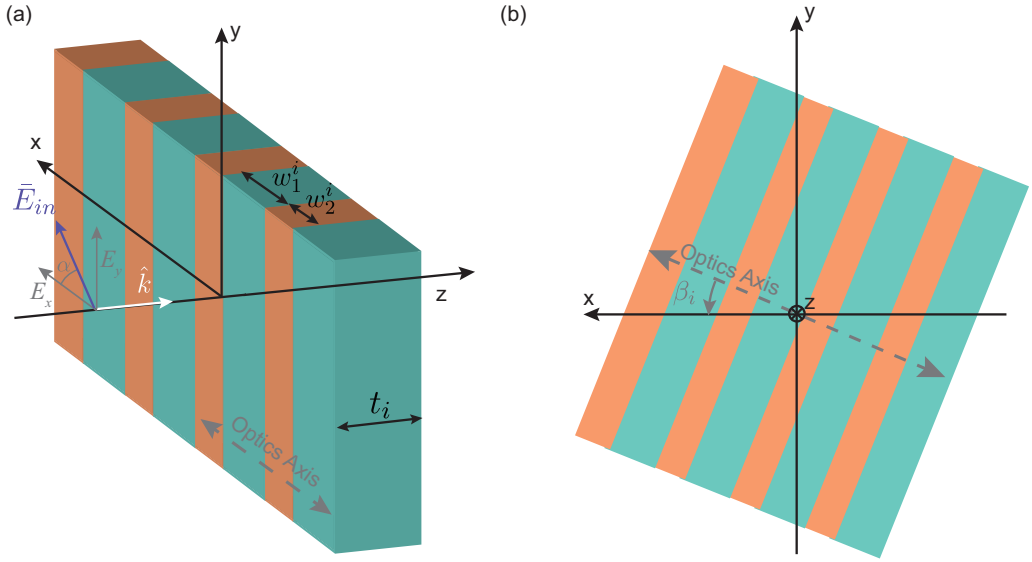

Figure 2.2: (a) All-dielectric form birefringent waveplate whose optic axis is parallel to the x-axis. The dielectric stack extends to infinity in the $\hat{y}$-direction and is repeated periodically along $\hat{x}$. An incoming plane-wave propagating along $\hat{z}$ whose E-field is contained in the xy-plane forming an angle α with the x-axis impinges the structure. (b) Front view of a waveplate whose optic axis is rotated anticlockwise an angle β_i about the z-axis.

$$\tilde{\epsilon} = \begin{bmatrix} \epsilon_{xx} & 0 & 0 \\ 0 & \epsilon_{yy} & 0 \\ 0 & 0 & \epsilon_{yy} \end{bmatrix}. \tag{2.15}$$

The values of ϵ_{xx} and ϵ_{yy} may be obtained by considering a normal incident plane wave with E-field $\vec{E} = E_x\hat{x} + E_y\hat{y}$ impinging the structure. From (2.13) and (2.15), the electric displacement obeys

$$D_x = \epsilon_{xx} E_x, \tag{2.16}$$

$$D_y = \epsilon_{yy} E_y. \tag{2.17}$$

These two components can be studied separately.

Initially, only the displacement produced by E_x is considered, Eq. (2.16). In the absence of charges, the boundary condition at the discontinuity between the two dielectric media can be derived from Gauss' law. This is, the normal component of $\vec{D}$ must be continuous across the interface. Hence, it must have the same value

inside the medium with ϵ_1 than in that with ϵ_2. Mathematically, the latter condition can be written as

$$D_x = E_1\epsilon_1 = E_2\epsilon_2, \tag{2.18}$$

being E_1 and E_2 the x-field components of the E-field in each medium. The effective E_x can be obtained as the average of this two

$$E_x = E_1 f_1 + E_2 f_2, \tag{2.19}$$

being f_1 and f_2 the fractions of volume occupied by the medium with ϵ_1 and ϵ_2 respectively, i.e. $f_1 = w_1/(w_1 + w_2)$ and $f_2 = 1 - f_1$. Substituting (2.18) and (2.19) in (2.16), the effective permittivity encountered by the x-polarised component may be obtained. This is

$$\epsilon_{xx} = \left(\frac{f_1}{\epsilon_1} + \frac{f_2}{\epsilon_2}\right)^{-1}. \tag{2.20}$$

Similarly, ϵ_{yy} can be calculated by independently considering the response of the structure to E_y which is given by (2.17). From Stokes' theorem it follows that the tangential components of the E-field must be continuous across the interface between the two dielectrics. This is

$$E_y = E_1 = E_2, \tag{2.21}$$

where E_1 and E_2 correspond to the y-components in this case. In this scenario, the effective electric displacement may be obtained via averaging

$$D_y = D_1 f_1 + D_2 f_2. \tag{2.22}$$

Finally, the permittivity ϵ_{yy} can be calculated by substituting (2.21) and (2.22) in (2.10)

$$\epsilon_{yy} = f_1\epsilon_1 + f_2\epsilon_2. \tag{2.23}$$

The relation $\epsilon_{yy} > \epsilon_{xx}$ can be used to identify the fast and slow axes of the structure –where fast and slow refer to phase velocity– with the x- and y-axis, respectively.

The more general case in which the optic axis of the waveplate is arbitrarily oriented in the XY plane is depicted in Fig. 2.2(b). Specifically, the waveplate has been rotated an angle β_i about the z-axis. In this situation, the effective permittivity tensor can be obtained from (2.15) via the rotation matrix [26]

$$\tilde{R}(\beta_i) = \begin{bmatrix} \cos(\beta_i) & -\sin(\beta_i) & 0 \\ \sin(\beta_i) & \cos(\beta_i) & 0 \\ 0 & 0 & 1 \end{bmatrix}, \tag{2.24}$$

as $\tilde{\epsilon}(\beta_i) = \tilde{R}(\beta_i)\tilde{\epsilon}\tilde{R}(-\beta_i)$ which produces the following permittivity tensor

$$\tilde{\epsilon}(\beta_i) = \begin{bmatrix} \epsilon_{xx}\cos^2(\beta_i) + \epsilon_{yy}\sin^2(\beta_i) & (\epsilon_{xx} - \epsilon_{yy})\cos(\beta_i)\sin(\beta_i) & 0 \\ (\epsilon_{xx} - \epsilon_{yy})\cos(\beta_i)\sin(\beta_i) & \epsilon_{xx}\sin^2(\beta_i) + \epsilon_{yy}\cos^2(\beta_i) & 0 \\ 0 & 0 & \epsilon_{yy} \end{bmatrix}. \tag{2.25}$$

2.3.2 Second order effective medium approximation

The expressions describing the effective permittivity values (2.20) and (2.23) are only valid when the period of the structure is deeply subwavelength. This is due to their derivation involving field averaging which is only meaningful for small variations of the field when the wave propagates distances of the order of the period along any arbitrary direction [27]. *Rytov* derived a more rigorous second order approximation to describe the effective permittivity values which include not only the physical properties of the structure but also the wavelength of operation, λ [27], leading to frequency dispersive homogenised materials. The effective permittivity values in this case can be calculated as

$$\epsilon_{xx}^{2nd} = \epsilon_{xx} + \frac{1}{3}\left[\frac{w_1 + w_2}{\lambda}\pi f_1 f_2 \left(\frac{1}{\epsilon_1} - \frac{1}{\epsilon_2}\right)\sqrt{\epsilon_{xx}\epsilon_{yy}^3}\right]^2, \tag{2.26}$$

$$\epsilon_{yy}^{2nd} = \epsilon_{yy} + \frac{1}{3}\left[\frac{w_1 + w_2}{\lambda}\pi f_1 f_2 \left(\epsilon_1 - \epsilon_2\right)\right]^2, \tag{2.27}$$

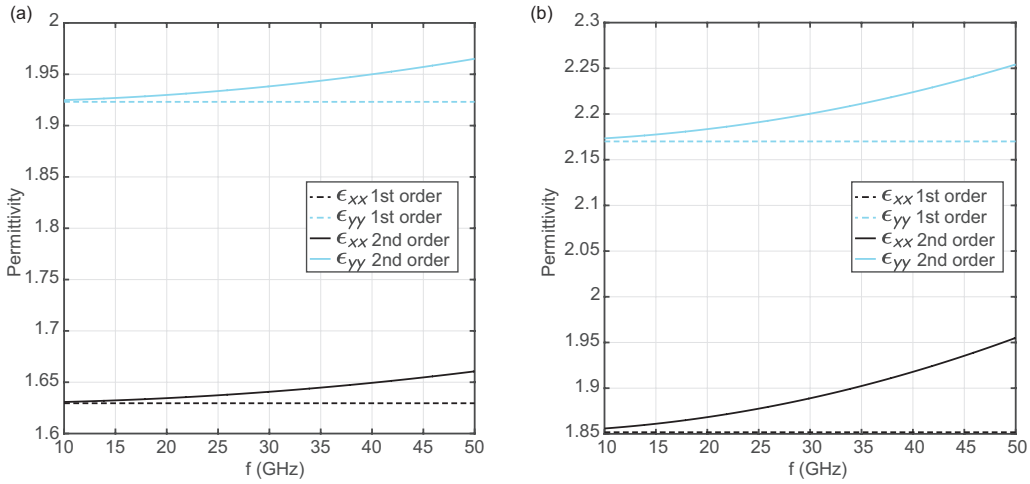

Figure 2.3: Effective permittivity estimated using the 1st order and 2nd order EMA when two dielectrics with relative permittivity values $\epsilon_1 = 1.21$ and $\epsilon_2 = 2.77$ are stacked as in Fig. 2.2(a). The widths of the layers are (a) $w_1 = 0.95$ mm ans $w_2 = 0.8$ mm, and (b) $w_1 = 1$ mm ans $w_2 = 1.6$ mm.

where ϵ_{xx} and ϵ_{yy} are given by (2.20) and (2.23), respectively. Note that this 2nd order approximation is still limited to subwavelength periodicities but is valid in a broader frequency range, as long as $w_1 + w_2 < \lambda$.

An example of the results obtained by homogenising the structure in Fig. 2.2(a) via the first and second order approximations is depicted in Fig. 2.3. Two different combinations of materials are considered and the results presented in Fig. 2.3(a) and 2.3(b), respectively. As can be seen, the values retrieved using both approximations are approximately equal at low frequencies for the two combinations studied. However, as the frequency shifts towards higher values, they increasingly deviate. Differences are more significant for the case shown in Fig. 2.3(b) than in Fig. 2.3(a), due to the longer periodicity employed in the former case.

2.4 Propagation through stratified anisotropic media

Propagation through dielectric stratified media can be described using different analytical models. In this thesis, three different models namely Jones' calculus, a Transfer Matrix Method (TFM) and Berreman's calculus have been analysed; a

summary of them is given in this section. Jones' calculus (section 2.4.1) is the preferred analytical model if only the polarisation state is of interest. The TFM yields more realistic results by considering reflections at the various dielectric interfaces at the expense of a higher analytical complexity. The TFM presented in section 2.4.2 neglects power conversion between XP components. Hence, it is valid only if the media can be described as in (2.15). The more general model, Berreman's calculus, is explained in section 2.4.3. This formalism widens the range of eligible materials by including randomly oriented anisotropic media described by (2.12). Nonetheless, it is considerably more convoluted incurring increased computational costs.

2.4.1 Jones' matrices

The polarisation state of a coherent electromagnetic wave such as that shown in Fig. 2.1 can be represented in a phasor form via its Jones' vector [22]

$$\bar{E}_{in} = \begin{bmatrix} E_{\theta 0} e^{j\phi_\theta} \\ E_{\varphi 0} e^{j\phi_\varphi} \end{bmatrix}. \tag{2.28}$$

Jones' calculus allows to easily estimate the effect that certain structures (e.g. waveplates) cause in the polarisation state of a wave propagating through them by means of a simple multiplication. As an example, we initially consider the case of propagation through a waveplate whose optic axis is tilted anticlockwise by an angle β_i, Fig. 2.2(b). The Jones' matrix of such a waveplate is [28]

$$J(\delta_i, \beta_i) = \begin{bmatrix} A & B \\ B & A^* \end{bmatrix}, \tag{2.29}$$

with $A = \cos(\delta_i/2) + j\cos(2\beta_i)\sin(\delta_i/2)$ and $B = j\sin(2\beta_i)\sin(\delta_i/2)$ and δ_i representing the phase-delay introduced upon transmission. In analogy to traditional waveplates, δ_i can be estimated from the product of the thickness t_i and the difference between the propagation constants

$$\delta_i = t_i(\sqrt{\epsilon_{yy}} - \sqrt{\epsilon_{xx}})\frac{\omega}{c}. \tag{2.30}$$

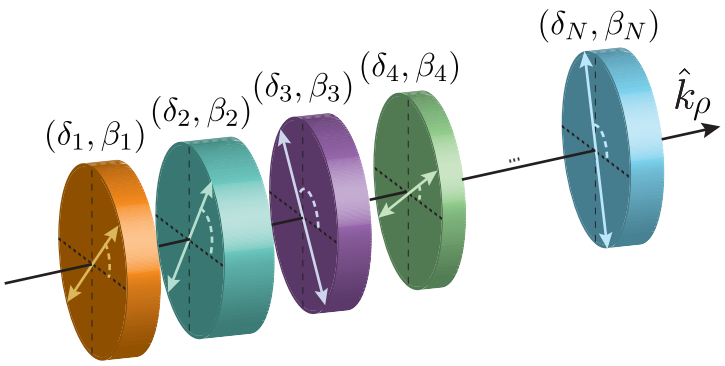

Figure 2.4: Schematic representation of a system consisting of N combined waveplates with different retardations δ_i and orientations β_i through which a plane-wave propagating along $-\hat{\rho}$ propagates.

Finally, the polarisation state at the output can be calculated as [26]

$$\bar{E}_{out} = J\left(\delta_i, \beta_i\right) \bar{E}_{in}. \tag{2.31}$$

More interestingly, Jones' equivalence theorem states that a system containing any number of retarders and rotators behaves, in terms of polarisation, as a simpler equivalent system consisting of a single retarder and a single rotator [26]. This allows to easily model propagation through multiple elements by means of an equivalent Jones' matrix, J_{tot}, which is given by the multiplication of the matrices of the individual elements. In particular, for a system consisting of N rotated waveplates as that shown in Fig. 2.4, J_{tot} reads

$$J_{tot} = \prod_{i=0}^{N-1} J\left(\delta_{N-i}, \beta_{N-i}\right), \tag{2.32}$$

where i indexes the layers and the individual Jones' matrices can be obtained using (2.29). Finally, the polarisation state after transmission through the system can be computed from

$$\bar{E}_{out} = J_{tot} \bar{E}_{in}. \tag{2.33}$$

2.4.2 Transfer matrix formalism

Reflections, which are neglected in Jones' formalism, can be accounted for using the TFM presented next. This TFM assumes that the permittivity tensors of all the

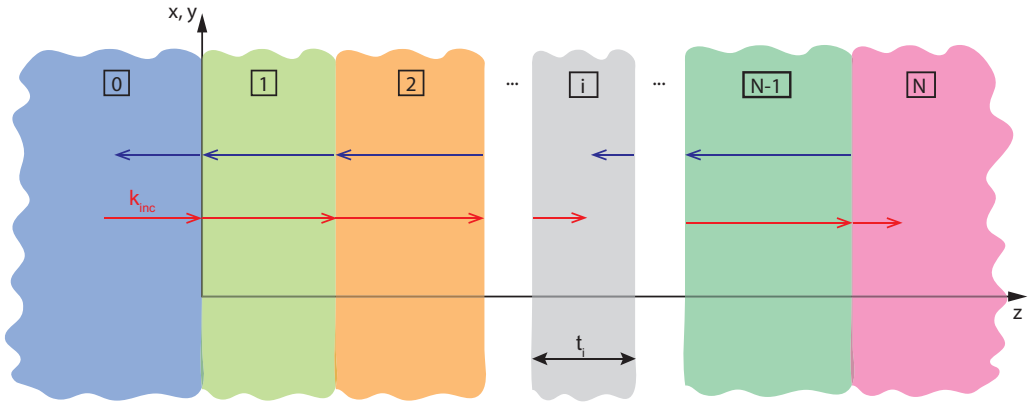

Figure 2.5: Electromagnetic wave propagation through a stratified dielectric medium when $\theta = 0^{\circ}$

materials involved are diagonal. Thus, it is only accurate if all the successive waveplates in Fig. 2.4 are axis aligned. Arbitrarily rotated off-axis aligned waveplates as those illustrated in Fig. 2.4 are not well described by such a simple TFM.

A normal incident wave propagating towards $+\hat{z}$ whose E-field is $\vec{E}_{in} = E_x\hat{x} + E_y\hat{y}$ propagating through a 1D stack of $i = 0, ..., N$ isotropic dielectric layers with thickness t_i and refractive index n_i is considered, Fig. 2.5. All the materials are assumed to be non-magnetic (relative permeability $\mu_i = 1$). Hence, the permittivity and the refractive index are directly related via $\epsilon_i = n_i^2 \in \mathbb{R}$. For a stack of birefringent media, the values of ϵ_i are polarisation dependent. In particular, in the E_x case, $\epsilon_i = \epsilon^i_{xx}$, whilst for E_y it is given by $\epsilon_i = \epsilon^i_{yy}$. Hence, the problem at hand can be significantly simplified by treating each polarisation separately.

The multilayer structure in Fig. 2.5 can be regarded as a two port system for which a Transfer Matrix (T-matrix) can be defined. Such a T-matrix relates forward and backward waves at the input and output ports. Moreover, since the structure can be built by cascading a series of layers and interfaces, its T-matrix may be computed by combining the individual matrices of the different interfaces and layers. Specifically, the T-matrix of the system can be obtained by simple multiplication of these individual matrices. Once the total T-matrix has been obtained, the reflection and transmission parameters for each polarisation can be computed algebraically. Next, the total transmitted field can be obtained in virtue of the superposition theorem and the AR from (2.6).

T-matrix of the interfaces

The interface between layer i and layer j (located at z_i) is considered first, Fig. 2.6(a). Due to the discontinuity, a plane wave impinging from the left $E_F(z_i^-)$ produces two waves: one transmitted to medium j and another one reflected backwards; namely, $E_F(z_i^+)$ and $E_B(z_i^-)$. Here, the F and B subscripts stand for forward or backward propagation, respectively, whilst the superscripts identify the direction from which the wave approaches the interface. Specifically, the superscript $-$ corresponds to waves propagating from the left, whilst the $+$ superscript indicates that they approach the interface from the right.

The backward and forward waves waves can be related through the complex Fresnel's coefficients r_{ij}, t_{ij}, r_{ji}, and t_{ji}, as

$$\begin{bmatrix} E_F(z_i^+) \\ E_B(z_i^-) \end{bmatrix} = \begin{bmatrix} t_{ij} & r_{ji} \\ r_{ij} & t_{ji} \end{bmatrix} \begin{bmatrix} E_F(z_i^-) \\ E_B(z_i^+) \end{bmatrix}. \tag{2.34}$$

Re-arranging (2.34) and considering the following identity relations [29]

$$r_{ij} = -rji, \tag{2.35}$$

$$t_{ij}t_{ji} - r_{ij}rji = 1, \tag{2.36}$$

the relation between the forward and backward waves propagating in layer i and those propagating in layer j can be described by

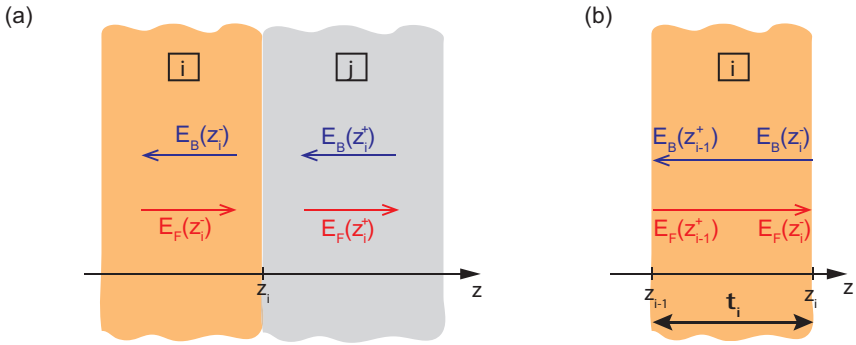

Figure 2.6: (a) Reflection and transmission at interface z_i. (b) Propagation through layer i.

$$\begin{bmatrix} E_F(z_i^-) \\ E_B(z_i^-) \end{bmatrix} = \frac{1}{t_{ij}} \begin{bmatrix} 1 & r_{ij} \\ r_{ij} & 1 \end{bmatrix} \begin{bmatrix} E_F(z_i^+) \\ E_B(z_i^+) \end{bmatrix}. \tag{2.37}$$

Hence, the T-matrix of the interface is

$$T_{ij} = \frac{1}{t_{ij}} \begin{bmatrix} 1 & r_{ij} \\ r_{ij} & 1 \end{bmatrix}, \tag{2.38}$$

With

$$r_{ij} = \frac{n_j - n_i}{n_j + n_i}, \tag{2.39}$$

$$t_{ij} = \frac{2n_j}{n_j + n_i}, \tag{2.40}$$

in the case of normal incidence [30].

T-matrix of the layers

Next, we consider the case of waves propagating through layer i illustrated in 2.6(b). The thickness of the layer is t_i and its refractive index n_i. At normal incidence, forward and backward waves propagating just before –$E_F(z_i^-)$ and $E_B(z_{i-1}^+)$– and just after the interfaces with adjacent layers –$E_F(z_{i-1}^+)$ and $E_B(z_i^-)$– may be related via

$$\begin{bmatrix} E_F(z_i^-) \\ E_B(z_{i-1}^+) \end{bmatrix} = \begin{bmatrix} \exp[j\phi_i] & 0 \\ 0 & \exp[-j\phi_i] \end{bmatrix} \begin{bmatrix} E_F(z_{i-1}^+) \\ E_B(z_i^-) \end{bmatrix}, \tag{2.41}$$

being $\phi_i = n_i t_i \omega / c$ the phase accumulated.

From (2.41), the T-matrix of the layer is

$$T_i = \begin{bmatrix} \exp[j\phi_i] & 0 \\ 0 & \exp[-j\phi_i] \end{bmatrix}. \tag{2.42}$$

Total T-Matrix

Lastly, the relation between forward and backward waves at the input (layer 0) and output (layer N) of the complete system may be described by the total T-matrix T_{0N} as follows

$$\begin{bmatrix} E_F(z_0^-) \\ E_B(z_0^-) \end{bmatrix} = T_{0N} \begin{bmatrix} E_F(z_{N-1}^+) \\ E_B(z_{N-1}^+) \end{bmatrix}, \tag{2.43}$$

with

$$T_{0N} = \begin{bmatrix} T_{11}^{0N} & T_{12}^{0N} \\ T_{21}^{0N} & T_{22}^{0N} \end{bmatrix} = T_{01}T_1T_{12}T_2 \cdot \ldots \cdot T_{N-1}T_{(N-1)N}. \tag{2.44}$$

In the case in which the incident field comes from the outer left media only (medium 0), $E_B(z_{N-1}^+) = 0$ and (2.43) simplifies to two equations with two unknowns from which the following transmission and reflection coefficients can be derived

$$r = \frac{E_B(z_0^-)}{E_F(x_0^-)} = \frac{T_{21}^{0N}}{T_{11}^{0N}}, \tag{2.45}$$

$$t = \frac{E_F(z_{N-1}^+)}{E_F(x_0^-)} = \frac{1}{T_{11}^{0N}}. \tag{2.46}$$

$$\tag{2.47}$$

Equivalent Circuit Network

An equivalent circuit model that produces the same results as the previous TFM is described next. From a circuit theory perspective the homogeneous effective medium equivalent to an axis aligned stack as that in Fig. 2.2 can be understood as a Transmission Line (TL) with length t_i, characteristic impedance Z_c and symmetric port impedance Z_0, Fig. 2.7.

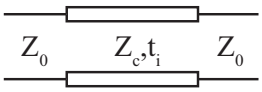

Figure 2.7: Equivalent circuit network to the structure in Fig. 2.2

The reflection coefficient of the air-dielectric interface is

$$\Gamma = \frac{Z_c - Z_0}{Z_c + Z_0}, \tag{2.48}$$

where the characteristic impedance of the equivalent transmission line is that of the effective medium $Z_c = Z_0/\sqrt{\epsilon_r}$ and Z_0 corresponds to the free-space impedance. The ABCD-matrix of the equivalent transmission line is [30]

$$\begin{bmatrix} A & B \\ C & D \end{bmatrix} = \begin{bmatrix} \cosh(j\phi) & Z_c \sinh(j\phi) \\ \sinh(j\phi)/Z_c & \cosh(j\phi) \end{bmatrix} \tag{2.49}$$

where the accumulated phase-shift upon transmission through the circuit is $\phi = t\sqrt{\epsilon_i}\omega/c$.

Given the ABCD representation, the S-parameters can be easily computed algebraically. In particular, the transmission S-parameter in (2.50) can be obtained using the relation $S_{21} = 2/(A + B/Z_0 + CZ_0 + D)$ [30]

$$S_{21} = \frac{(1 - \Gamma^2)\exp[-j\phi]}{1 - \Gamma^2 \exp[-2j\phi]}. \tag{2.50}$$

This equivalent model may be extended to describe multilayer structures (as long as all the cascaded waveplates are axis aligned) as that in Fig. 2.6 by concatenating sections of transmission lines with adequate lengths and impendances via their ABCD-matrices. From these, the retrieval of the total S-parameters is straightforward.

2.4.3 Berreman's calculus

Tailoring the relative rotation between various waveplates, Fig. 2.4, may serve to enhance the performance of the polarisation converters (see section 2.6). In consequence, a more flexible formalism that allows propagation through materials with non-diagonal permittivity tensors, which is not well described by the TFM, and accounts for reflections and interference effects (neglected by Jones' formalism) is required. Berreman's calculus overcomes such limitations.

Introduction to Berreman's calculus

In this section, the 4×4 matrix formalism proposed by *Berreman* to describe reflection and transmission through stratified anisotropic media is introduced [31]. The derivation starts from Maxwell equations in gaussian units

$$\nabla \times \vec{E} = -\frac{1}{c}\frac{\partial \vec{B}}{\partial t}, \tag{2.51}$$

$$\nabla \times \vec{H} = \frac{1}{c}\frac{\partial \vec{D}}{\partial t}. \tag{2.52}$$

Assuming a time dependence of the form $\exp[-j\omega t]$, the 6×6 representation in phasor form of (2.51) and (2.52) is

$$\begin{bmatrix} 0 & 0 & 0 & 0 & -\frac{\partial}{\partial z} & \frac{\partial}{\partial y} \\ 0 & 0 & 0 & \frac{\partial}{\partial z} & 0 & -\frac{\partial}{\partial x} \\ 0 & 0 & 0 & -\frac{\partial}{\partial y} & \frac{\partial}{\partial x} & 0 \\ 0 & \frac{\partial}{\partial z} & -\frac{\partial}{\partial y} & 0 & 0 & 0 \\ -\frac{\partial}{\partial z} & 0 & \frac{\partial}{\partial x} & 0 & 0 & 0 \\ \frac{\partial}{\partial y} & -\frac{\partial}{\partial x} & 0 & 0 & 0 & 0 \end{bmatrix} \begin{bmatrix} E_x \\ E_y \\ E_z \\ H_x \\ H_y \\ H_z \end{bmatrix} = \frac{-j\omega}{c} \begin{bmatrix} D_x \\ D_y \\ D_z \\ B_x \\ B_y \\ B_z \end{bmatrix}. \tag{2.53}$$

The formalism in [31] may include magneto-electric effects, i.e. bi-anisotropic materials with non-zero coupling tensors $\tilde{\xi}$ and $\tilde{\varsigma}$. For the sake of simplicity, we limit instead to anisotropic media ($\tilde{\xi} = \tilde{\varsigma} = 0$) which are defined by simpler constituent relations, (2.13) and (2.14). As a result, (2.53) can be simplified and rearranged to give the following sets of equations

$$\begin{bmatrix} 0 & -\frac{\partial}{\partial z} & \frac{\partial}{\partial y} \\ \frac{\partial}{\partial z} & 0 & -\frac{\partial}{\partial x} \\ -\frac{\partial}{\partial y} & \frac{\partial}{\partial x} & 0 \end{bmatrix} \begin{bmatrix} H_x \\ H_y \\ H_z \end{bmatrix} = \frac{-j\omega}{c}\tilde{\epsilon} \begin{bmatrix} E_x \\ E_y \\ E_z \end{bmatrix}, \tag{2.54}$$

$$\begin{bmatrix} 0 & \frac{\partial}{\partial z} & -\frac{\partial}{\partial y} \\ -\frac{\partial}{\partial z} & 0 & \frac{\partial}{\partial x} \\ \frac{\partial}{\partial y} & -\frac{\partial}{\partial x} & 0 \end{bmatrix} \begin{bmatrix} E_x \\ E_y \\ E_z \end{bmatrix} = \frac{-j\omega}{c}\tilde{\mu} \begin{bmatrix} H_x \\ H_y \\ H_z \end{bmatrix}, \tag{2.55}$$

where $\tilde{\epsilon}$ is given by (2.12). Similarly, the permeability tensor is

$$\tilde{\mu} = \begin{bmatrix} \mu_{xx} & \mu_{xy} & \mu_{xz} \\ \mu_{yx} & \mu_{yy} & \mu_{yz} \\ \mu_{zx} & \mu_{zy} & \mu_{zz} \end{bmatrix}, \tag{2.56}$$

which in our case may be simplified to the 3×3 identity matrix $\tilde{I}$ (no magnetic activity is considered). Likewise, the problem can be further simplified by considering that the fields only vary along $\hat{z}$ and incidence is in the xz-plane, Fig. 2.2. This is, solutions of the form

$$E(x, y, z) = E(z) \exp[jk_x x], \tag{2.57}$$

$$H(x, y, z) = H(z) \exp[jk_x x], \tag{2.58}$$

where k_x represents the wavevector. In this scenario, (2.54) and (2.55) can be written as

$$\begin{bmatrix} 0 & -\frac{\partial}{\partial z} & 0 \\ \frac{\partial}{\partial z} & 0 & -jk_x \\ 0 & jk_x & 0 \end{bmatrix} \begin{bmatrix} H_x \\ H_y \\ H_z \end{bmatrix} = \frac{-j\omega}{c} \tilde{\epsilon} \begin{bmatrix} E_x \\ E_y \\ E_z \end{bmatrix}, \tag{2.59}$$

$$\begin{bmatrix} 0 & \frac{\partial}{\partial z} & 0 \\ -\frac{\partial}{\partial z} & 0 & jk_x \\ 0 & -jk_x & 0 \end{bmatrix} \begin{bmatrix} E_x \\ E_y \\ E_z \end{bmatrix} = \frac{-j\omega}{c} \begin{bmatrix} H_x \\ H_y \\ H_z \end{bmatrix}. \tag{2.60}$$

The components normal to the interfaces

$$H_z = \frac{c}{\omega} k_x E_y, \tag{2.61}$$

$$E_z = -\frac{\epsilon_{zx} E_x + \epsilon_{zy} E_y + (c/\omega) k_x H_y}{\epsilon_{zz}}, \tag{2.62}$$

are not required for matching the boundary conditions. By substituting (2.61) and (2.62), they can be eliminated from (2.59) and (2.60) so that the 3×3 systems reduce to 2×2. These may be subsequently combined to give the following first order linear system of differential equations

$$\frac{\partial}{\partial z}\begin{bmatrix} E_x \\ H_y \\ E_y \\ H_x \end{bmatrix} = \frac{j\omega}{c}\begin{bmatrix} -\upsilon\frac{\epsilon_{zx}}{\epsilon_{zz}} & 1-\frac{\upsilon^2}{\epsilon_{zz}} & -\upsilon\frac{\epsilon_{zy}}{\epsilon_{zz}} & 0 \\ \epsilon_{xx}-\frac{\epsilon_{zx}\epsilon_{xz}}{\epsilon_{zz}} & -\upsilon\frac{\epsilon_{xz}}{\epsilon_{zz}} & \epsilon_{xy}-\frac{\epsilon_{xz}\epsilon_{zy}}{\epsilon_{zz}} & 0 \\ 0 & 0 & 1 & 0 \\ -\epsilon_{yx}+\frac{\epsilon_{yz}\epsilon_{zx}}{\epsilon_{zz}} & \upsilon\frac{\epsilon_{yz}}{\epsilon_{zz}} & -\epsilon_{yy}+\frac{\epsilon_{zy}\epsilon_{yz}}{\epsilon_{zz}}+\upsilon^2 & 0 \end{bmatrix}\begin{bmatrix} E_x \\ H_y \\ E_y \\ H_x \end{bmatrix}, \tag{2.63}$$

with $\upsilon = k_x(c/\omega) = n_i \sin\theta_i$, being n_i the index of refraction of the medium at the input and θ_i the angle of incidence. In consequence, in the case of normal incidence $\theta_i = 0°$ and υ vanishes.

For simplicity, it is convenient to abbreviate (2.63) as

$$\frac{\partial \vec{F}}{\partial z} = \frac{j\omega}{c}\hat{L}\vec{F}. \tag{2.64}$$

The solutions to (2.64) may be obtained via diagonalisation. This is $\hat{L} = \hat{F}\hat{\alpha}\hat{F}^{-1}$ with field matrix

$$\hat{F} = \begin{bmatrix} E_{x1}^{+} & E_{x1}^{-} & E_{x2}^{+} & E_{x2}^{-} \\ H_{y1}^{+} & H_{y1}^{-} & H_{y2}^{+} & H_{y2}^{-} \\ E_{y1}^{+} & E_{y1}^{-} & E_{y2}^{+} & E_{y2}^{-} \\ H_{x1}^{+} & H_{x1}^{-} & H_{x2}^{+} & H_{x2}^{-} \end{bmatrix} \tag{2.65}$$

and diagonal matrix

$$\hat{\alpha} = \begin{bmatrix} \alpha_1^{+} & 0 & 0 & 0 \\ 0 & \alpha_1^{-} & 0 & 0 \\ 0 & 0 & \alpha_2^{+} & 0 \\ 0 & 0 & 0 & \alpha_2^{-} \end{bmatrix}, \tag{2.66}$$

where $\hat{F}$ and $\hat{\alpha}$ are the eigenvectors and eigenvalues of $\hat{L}$, respectively, and the superscripts $+$ and $-$ indicate forward and backward propagation whilst the subscripts 1 and 2 are associated with waves polarised along x or y.

Calculating $\hat{F}$ of an isotropic medium with refractive index n is substantially simpler, since the fields are directly related by

$$\frac{H_y^{+}}{E_x^{+}} = -\frac{H_y^{+}}{E_x^{+}} = -\frac{H_x^{+}}{E_y^{+}} = \frac{H_x^{+}}{E_y^{+}} = n/\eta_0 \cos(\theta), \tag{2.67}$$

being η_0 the free-space impedance [32].

From the auxiliary matrix $\hat{L}$ in (2.63), calculating the transmitted and reflected fields through multilayer systems as that in Fig. 2.4 is straightforward. The detailed derivation is available in [32] and will not be repeated here. Reference [32] is accompanied by the Birefringent Thin Films (BTF) MATLAB toolbox [33], which will be employed later on this chapter. The calculation of the transmission and reflection parameters using the BTF toolbox is described in appendix A.

2.5 Synthesis and experimental realisation of form birefringent waveplates

In section 2.3.1, we proposed a possible realisation of a birefringent medium consisting of a periodic arrangement of isotropic dielectric materials. Here, we will show how such a simple artificial birefringent media can be used to synthesise microwave waveplates. To this end, the reflection and transmission coefficients shall be retrieved using any of the analytical models discussed in section 2.4 (Jones', the TFM/TL or Berreman's method). The waveplates can be synthesised combining any of these models with an optimization algorithm. In particular, an Evolution Strategy (ES) with Covariance Matrix Adaptation (CMA) technique has been used [34]. This algorithm is stochastic, derivative-free and broadly based in biological evolution. In each iteration, new candidate solutions are generated via random variation of the current potential solutions. This helps avoiding getting trapped in local minima.

Among the three models presented, Jones' is considerably simpler, requiring in turn less computational resources and assuring the fast convergence of the CMA-ES algorithm. Regardless of its abovementioned limitations, optimization is greatly simplified and the values estimated following this procedure may provide a good starting point for a subsequent optimization using a more precise model or a commercial electromagnetic solver in case higher precision is needed. Some examples of the computational costs associated with the different methods described in this chapter can be found in section 2.7.

Without loss of generality, a LP incident plane wave propagating along $-\hat{z}$ whose E-field is oriented at $\alpha = 45^\circ$ impinging the t_i-thick axis aligned waveplate depicted

in Fig. 2.2(a) is considered. The Jones' vector of such a wave is given by (2.28). After propagation through the waveplate, the polarisation state at the output can be computed from (2.31). From this, it is clear that by choosing an approriate value of t_i, the waveplate may produce a tailored rotation of the polarisation state (e.g. to achieve LP-to-CP conversion). The most suitable value of t_i can be estimated with the CMA-ES algorithm, by simply customizing the goal function to fit the intended performance, e.g. AR = 0 dB for pure LP-to-CP conversion.

2.5.1 Measurement set-up

A PNA Microwave Network Analyzer (Agilent N5225A) was used for measuring the magnitude and phase of the transmission coefficient using the set-up depicted in Fig. 2.8(a). It consists of two Ka-band standard gain 22240 Flann horn antennas positioned $d = 80$ cm away from each other acting as the transmitter and the receiver. Customized antenna holders were designed and fabricated via 3D-printing (see appendix B). The Device Under Test (DUT) is located at the central position, $\sim d/2$. The 45° polarised input was obtained via superposition of the individual responses of the DUT to x- and y-polarised radiation. For simplicity, polarisation was shifted between these two by rotating the DUT 90° about the direction of propagation. In this manner, rotating the antennas is unnecessary, minimizing, for instance, the risk of misalignment.

The area illuminated by the transmitter within this configuration can be estimated geometrically, based on the diagram depicted in Fig. 2.8(b). Since the 3dB beamwidth $\theta_{-3\text{dB}}$ of a pyramidal horn is different in the E- and H-planes, the area illuminated by such a transmitting antenna can be approximated by an ellipse. However, for the set-up only the worst case (that illuminating a bigger surface) needs to be considered, i.e. the E-plane case. Fig. 2.8(c) shows the radius of the illuminated area estimated as $R = (d/2)\tan(\theta_{-3\text{dB}})$, where $\theta_{-3\text{dB}}$ corresponds to the E-plane beamwidth. The fraction of power radiated that propagates through the DUT may be approximated from the figure. The lower the frequency, the bigger the illuminated area. When this exceeds the lateral dimensions of the DUT, its response may deviate from the infinite case due to border effects. To alleviate diffraction as well as reflections at the DUT holder, an absorbing window was included in the

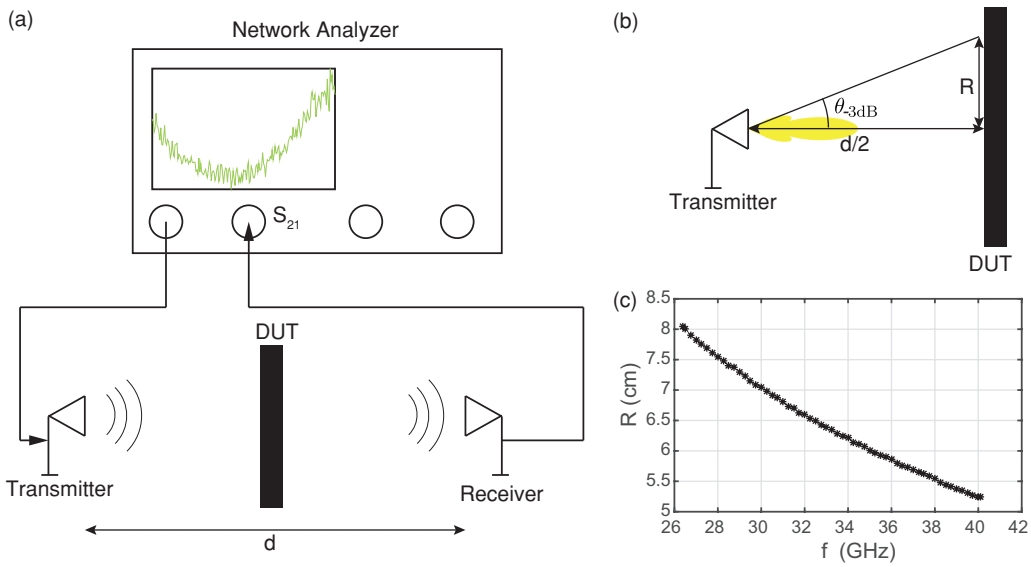

Figure 2.8: (a) Schematic of the measurement set-up. Two horn antennas are separated a distance d. The DUT is located between them, at the central position. (b) Area illuminated by the receiving antenna. (c) Estimated illumination radius.

measurements.

Since there are no pre-defined commercial standards for free-space measurements, calibration is quite challenging. However, measurements of the AR and phase-delay are quite robust against calibration uncertainty, as they involve relative values between two measurements. Per contra, Insertion Loss (IL) measurements are much more affected by calibration errors and other problems caused by the set-up. To reduce uncertainty, a *frequency response calibration* which allows the antennas to remain static, thus minimizing possible missalignment and/or missplacement effects, was employed. Additionally, this type of calibration includes the whole system (even the horns) and avoids connecting and disconnecting any elements. This allows to directly visualize the response of the DUT on the PNA screen which considerably facilitates the measurement process. For increased accuracy in measuring the IL, transmission through the DUT was subsequently normalized to measured transmission when only the absorbing window is present. Finally, time-gating using a Hann window –which typically offers a good trade-off between spectral resolution and dynamic range– is used in order to filter background noise (e.g. reflections in the connectors and losses in the cables that were not removed by the calibration). No multipath interference was identified.

2.5.2 A quarter-plate for linear-to-circular polarisation conversion

Initially, a waveplate consisting of alternating layers of $w_1 = 0.95$ mm ROHACELL 31 HF rigid foam and $w_2 = 0.8$-mm-wide Taconic TLY-5 Polytetrafluoroethylene (PTFE) was designed, Fig. 2.2. The electric permittivity of both materials was characterised at the central frequency using a free-space characterization technique [35]. This consists in retrieving the permittivity of a slab of free-standing material from the measured phase-shift upon transmission. The permittivity values were found to be $\epsilon_1 = 1.21$ and $\epsilon_2 = 2.77$, which show non-negligible deviations from those indicated by the manufacturers at lower frequencies. These two media cause the effective dielectric constants in (2.20) and (2.23) to be $\epsilon_{xx} = 1.63$ and $\epsilon_{yy} = 1.92$. Note that these two values are very close to unity, thus minimizing loses through better free-space matching. The estimated loss tangents obtained by adjusting the measurements to full-wave simulations were $\tan(\delta_{xx}) = 0.0046$ and $\tan(\delta_{yy}) = 0.0072$.

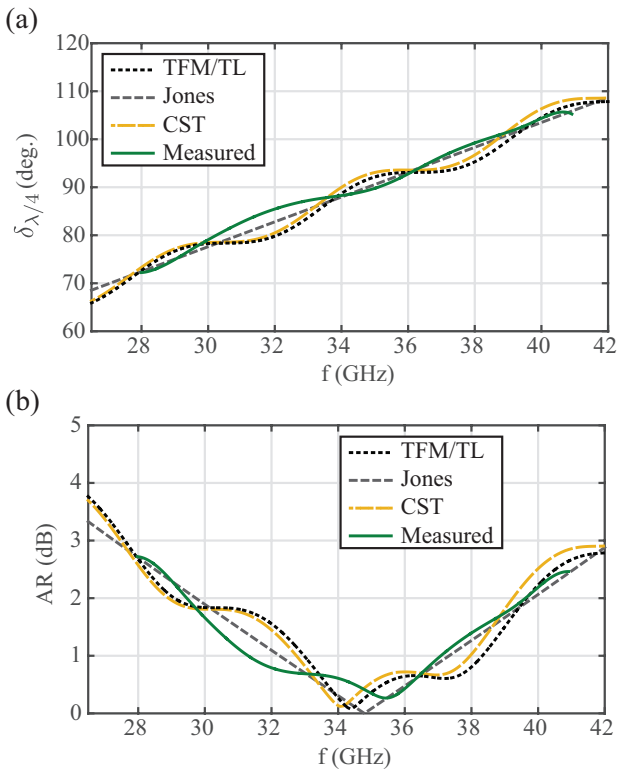

Figure 2.9: (a) Phase-shift and (b) realised AR when a normal incident LP plane-wave travels through the designed quarter-plate obtained using the TFM/TL, Jones' formalism, CST simulations and measurements of the fabricated prototype.

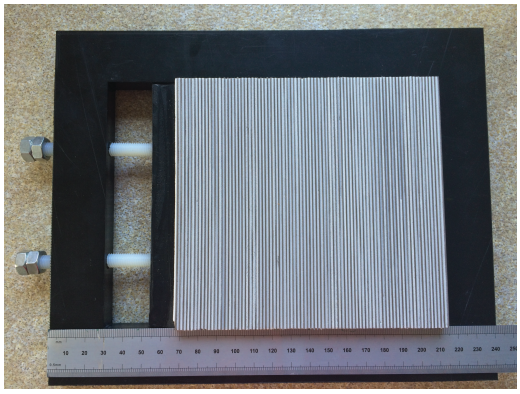

Figure 2.10: Fabricated quarter-plate.

The thickness of the waveplate ($t_{\lambda/4} = 19.4$ mm) was optimized so that AR = 0 dB at 34.8 GHz, thus achieving perfect LP-to-CP conversion.

Fig. 2.9(a) and Fig. 2.9(b) show a comparison of the phase-delay and AR values obtained using Jones' formalism, the TFM (or the TL equivalent), simulations using CST Microwave Studio and measurements of the fabricated prototype. The DUT is shown in Fig. 2.10 and consists of 80 pairs of foam and PTFE laminate enclosed by an adjustable plastic frame with nylon screws. The stack of dielectrics is only held together by pressure produced by such a frame, which provides the required mechanical stability. The lateral dimensions of the stack are 135 mm $\times$144 mm or equivalently $15\lambda \times 16\lambda$ at 33.25 GHz, so that power radiated through the DUT is maximized whilst minimising the amount of necessary materials. As can be seen, the agreement between all the curves is excellent. Deviations with respect to the measurements are attributed to increased dielectric losses (the dielectrics were assumed lossless in the simulations) and fabrication tolerances. Since in the designed converter reflections at the interfaces are nearly negligible (measured $S_{11} < -19$dB), i.e. the converter is nearly perfectly matched to free-space, results obtained using Jones' formalism, (2.30), and the TFM method, (2.50), agree remarkably well. Neglecting the impedance mismatch results in the curves given by (2.30) being linear with frequency. When, on the contrary, the mismatch is considered as is the case in the TFM, results present oscillations, also present in CST simulations and in the measurements. These are due to coupling of the incoming radiation to the cavity formed, which in addition is polarisation dependent. However, thanks to the utilisation of dielectrics with low contrast between ϵ_1 and ϵ_2, the interaction of electromagnetic waves with the cavity is very similar independently of them being x- or

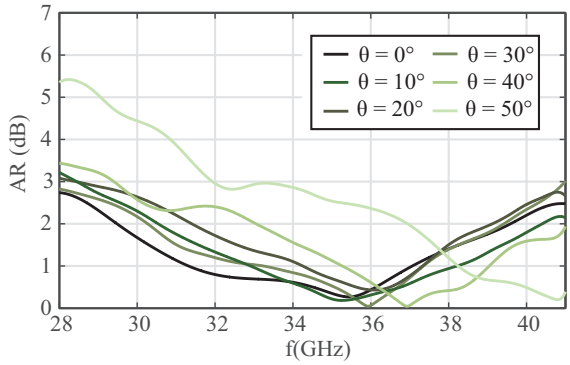

Figure 2.11: Measured AR for $\theta = 0 - 50°$ incidence.

y-polarised. Additionally, the materials employed produce ϵ_{xx} and ϵ_{yy} values close to 1, minimizing the mismatch and in turn the IL. This produces very weak oscillations that don't deteriorate much the performance of the DUT and therefore, Jones' formalism yields good accuracy albeit its simplicity. Hence, there is a compromise between IL and thickness, as suggested by (2.30). An approach to overcome this limitation will be proposed in chapter 3.

As also shown in Fig. 2.9(a) and Fig. 2.9(b), results obtained using (2.50) are nearly identical to those obtained through CST simulations. Small differences can be appreciated as the frequency increases due to the limited validity of the first order EMA. Likewise, the agreement with the measurements is good. The minimum measured AR is 0.27 dB at 35.5 GHz (2% operating frequency shift attributed to fabrication tolerances and measurement uncertainty). The measured 3dB AR fractional bandwidth is 39% while the 1dB AR bandwidth is approximately 17%. Similarly to traditional quarter-plates, the retardation introduced between E_x and E_y is equal to 90° at a single frequency, 35.2 GHz, which is very close to the operating frequency, Fig. **??**. This indicates that the magnitude of E_x and E_y are nearly identical, which is also a requirement for getting pure CP. IL calculated from the measured transmission parameter normalized to the case of free-space propagation is ∼0.6 dB at the operating frequency which is similar to current state-of-the art technologies [8]. The latter property together with the low reflections achieved, make the proposed converter particularly suitable for its integration in antenna systems.

The angular stability of the structure is investigated in Fig. 2.11 which shows the measured AR when the angle of incidence varies between $\theta = 0 - 50°$. As can be seen, the response is remarkably stable up to 30°. As the angle of incidence increases

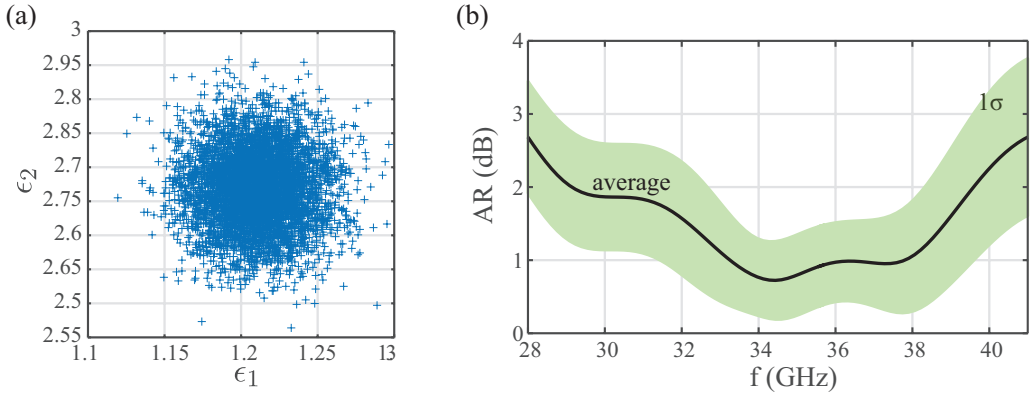

Figure 2.12: Sensitivity analysis to random variations of ϵ_1 and ϵ_2. (a) ϵ_1 and ϵ_2 values considered in the analysis. (b) Average AR and 1-σ confidence interval.

further, the minimum AR shifts towards higher frequencies. For instance, $\theta = 40°$ causes a 4% frequency deviation, whilst $\theta = 50°$ yields 15%. In terms of bandwidth, the response of the DUT remains mostly unaltered whilst the IL is kept below 1.5dB for $\theta < 50°$.

Additionally, the AR sensitivity caused by random variations of ϵ_1 and ϵ_2 was studied using a Montecarlo analysis. The different combinations of permittivity values (ϵ_1, ϵ_2) used in this study are shown in Fig. 2.12(a). 5000 samples where considered. These were obtained by randomly sampling a 2D Gaussian distribution centred at the original permittivity values ($\epsilon_1 = 1.21$, $\epsilon_2 = 2.77$) with 2% standard deviation. The AR was calculated using (2.50). The resulting statistics are summarized in Fig. 2.12(b) where the black curve represents the average AR and the shadowed areas correspond to the the 1-σ confidence interval. Our results show that the performance of the converter is robust against small fluctuations in the dielectric constant which may be caused in practice by temperature variations or mechanical stress.

A comparison between our quarter-plate and some of the previous technologies is summarized in Table 2.1. This suggests that the prototype presented here outperforms existing converters in terms of AR [11, 23] and bandwidth [8, 10], at the expense of being thicker than other single-layer structures [10, 23]. Our measurements indicate that the converter exhibits good angular stability, comparable to [23] and IL similar to that of state-of-the-art technologies [8].

Table 2.1: Comparison with existing LP-to-CP converters

Ref.	Ours	[8]	[10]	[11]	[23]
f (GHz)	35.5	95	325	8.83	12.6
Bandwidth (%)	39	5	12	-	63
AR (dB)	0.27	0.23	0.19	2.5	0.7
Angular Stability (°)	0-40	0-17	-	-	0-45
IL (dB)	0.6	0.3	3.4	2	-
t (mm)	19.4	9.5	0.001	16.5	1.5

2.5.3 A half-plate for cross-polarisation conversion

The technology presented in this chapter is not limited to the synthesis of LP-to-CP converters. Other types of conversion can be achieved with equal ease, by carefully choosing the orientation and thickness of the waveplate. For instance, an axis aligned waveplate providing half-wave retardation (180° phase-delay), may achieve nearly total XP conversion. This is, if a LP wave with E-field polarised along $\alpha = 45°$ propagates through the structure, a LP wave with $\alpha = 135°$ is obtained at the output. Analogously, such a half-plate would also convert between handedness of CP waves.

A half-plate consisting of alternating layers of $w_1 = 1$ mm ROHACELL 31 HF rigid foam and $w_2 = 1.6$-mm-wide Taconic TLY-5 PTFE was designed and fabricated. The effective dielectric constants of the equivalent medium homogenized using the 1st and 2nd order EMAs are compared in Fig. 2.13(a). The period of the structure is $\sim 0.3\lambda$, where λ corresponds to 34.8 GHz. Such a long period causes the 1st and 2nd order approximation to produce significantly different results. Our results suggest that the 2nd order approximation describes more precisely the performance of the device in this situation. Fig. 2.13(b) and 2.13(c) show the results obtained with this approach when the thickness of the waveplate is $t_{\lambda/2} = 38.8$ mm. There, the phase-delay and AR obtained using the TFM/TL are compared against those measured in the experiment. As can be seen, the agreement is very good. The frequency shift of the AR peak at which polarisation at the output is almost perfectly linear is $< 1\%$. Approximately at the same frequency, $\delta_{\lambda/2} = 180°$ hence achieving nearly total XP conversion.

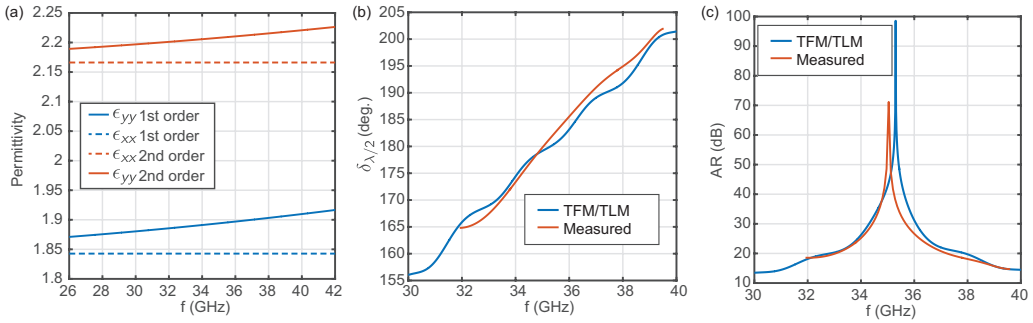

Figure 2.13: (a) Effective permittivy values of the half-plate. (b) Phase-delay and (b) AR realised when $t_{\lambda/2} = 38.3$ mm.

2.6 Synthesis and experimental realisation of multi-plate systems for broadband linear-to-circular polarisation conversion

Several techniques dealing with flattening the retardation introduced by traditional birefringent crystals over broader frequency ranges are available in the literature [36–41]. As the artificial waveplates proposed in the previous section have demonstrated equivalent performances to those based in crystal birefringence, considering applying similar techniques comes naturally. In particular, we focus on those capable of mitigating frequency dispersion. Such techniques hold promise for broadening the bandwidth of operation of the polarisation converters demonstrated in section 2.5. One of the most popular consists in cascading axis aligned waveplates made of different materials to compensate the overall phase-delay [36]. The main drawback of this approach is that, unless the utilised media share very similar dielectric constants, reflections between the successive plates become severe, degrading the performance. As a result, IL increases limiting the practical application of the converter to antenna systems. One could think about reducing the contrast to improve impedance matching as a means to overcome this limitation, but the number of layers required grows rapidly, resulting in considerably bulky cascaded systems. A different mechanism that addresses this limitation was proposed in [38] and later applied to build achromatic half-plates [36, 37] and quarter-plates of birefringent crystals [39–41]. In the work by *Pancharatman*, the operating bandwidth was broadened by cascading waveplates made of the same birefringent material with tailored thicknesses t_i and

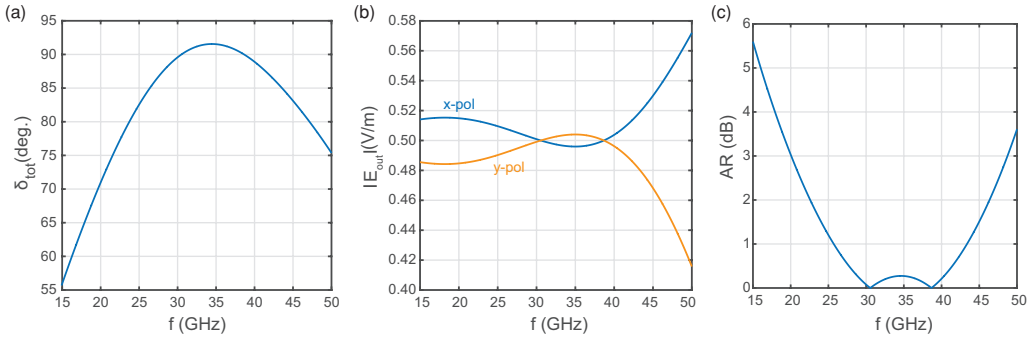

Figure 2.14: Results obtained via Jones' calculus when $\vec{E}_{in} = \cos(45°)\hat{x} + \sin(45°)\hat{y}$. (a) Phase-delay. (b) Normalized magnitude of the E-field components. (c) AR.

rotations β_i [38], Fig. 2.4. By rotating the waveplates by an angle $\beta_i \neq 0°$ or 90°, the off-diagonal elements of the permittivity tensor become non null, as shown in (2.25). This results in the field components appearing coupled in (2.53). Therefore, the problem at hand is not accurately described by the TFM/TL proposed in section 2.4.2 but by the more rigorous Berreman's calculus (section 2.4.3). Despite its limited accuracy, Jones formalism (section 2.4.1) in combination with the CMA-ES algorithm can be used to efficiently find a suitable configuration as the starting point of the design. This can be later refined by means of Berreman's model.

Here, it will be shown how to realise low dispersive broadband LP-to-CP converters cascading only two waveplates. The CMA-ES algorithm was employed in combination with Jones' calculus for optimizing the thickness t_i of the layers and their relative rotations β_i. The defined cost function was $\sum_k [AR(f_k)]^2$ (minimum AR) with f_k = 26.5–41 GHz. The required rotations were found to be $\beta = \pm 29.7°$ and the thickness 38.8 mm (half-plate) and 19.4 mm (quarter-plate), respectively, for an input field polarised at 45° . Two waveplates made of 0.95-mm-wide ROHACELL and 0.8-mm-wide TLY-5 are considered next. The results obtained with this configuration are summarized in Fig. 2.14. In this particular case, the AR is equal independently of which plate is rotated clockwise and which one is rotated anticlockwise, as long as they undergo rotations in opposite directions. Contrarily, the order of the plates is not trivial. For optimum performance, the half-plate must be located first (at the input), followed by the quarter-plate. As shown in Fig. 2.14(a), the phase-delay between the x- and y-polarised field components bends around 90° instead of increasing linearly with frequency, as was the case in Fig. 2.9(a) and 2.13(b). Within the 26.5–41 GHz frequency range, the maximum deviation with respect to 90° is

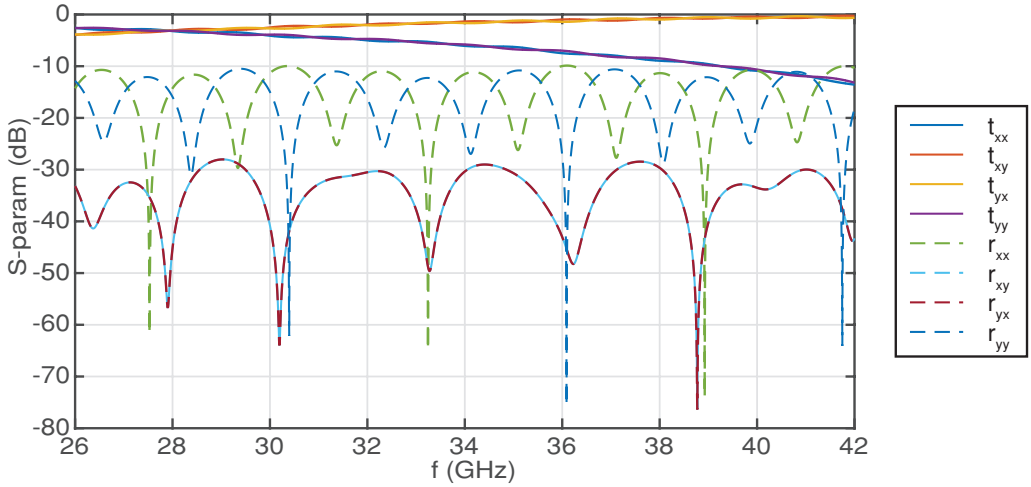

Figure 2.15: S-parameters calculated using Berreman's formulation.

$< 7°$. This, together with the two polarisations sharing approximately equal power, Fig. 2.14(b), produces ∼51% 1dB fractional bandwidth (25.7–43.4 GHz) and an impressive ∼84% 3dB bandwidth (20–48.8 GHz). This is, the bandwidth doubles with respect to the individual quarter-plate case.

More accurate results can be obtained using Berreman's formalism which accounts for reflections and interference effects caused by the various discontinuities (input, output and in between waveplates interfaces). The transmission and reflection parameters calculated with this formalism using the BTF toolbox described in appendix A, are shown in Fig. 2.15. As can be observed, since the rotated waveplates have permittivity tensors with non-zero off-diagonal components, the XP transmission parameters (labelled as t_{xy} and and t_{yx}) are not negligible within the frequency range at hand. Instead, as given by (2.63), they contribute towards transmission and hence, towards the conversion. Interference effects in the form of oscillations in the S-parameters can be clearly appreciated. Reflections are < -10 dB for the CoP components within the considered frequency range –this value is considerably higher than in the case of the individual quarter-plate– and < -30 dB for the XP ones. As previously discussed, reflections are a consequence of the permittivity mismatch at the interfaces which forms a cavity. Despite the constituent materials of the two waveplates being equal, the relative rotations between the waveplates cause their effective permittivity tensors to significantly differ, in turn increasing reflections. It is worth emphasizing that this effect may be mitigated by using a higher number of thinner waveplates with smaller relative rotations, so that the propagating wave

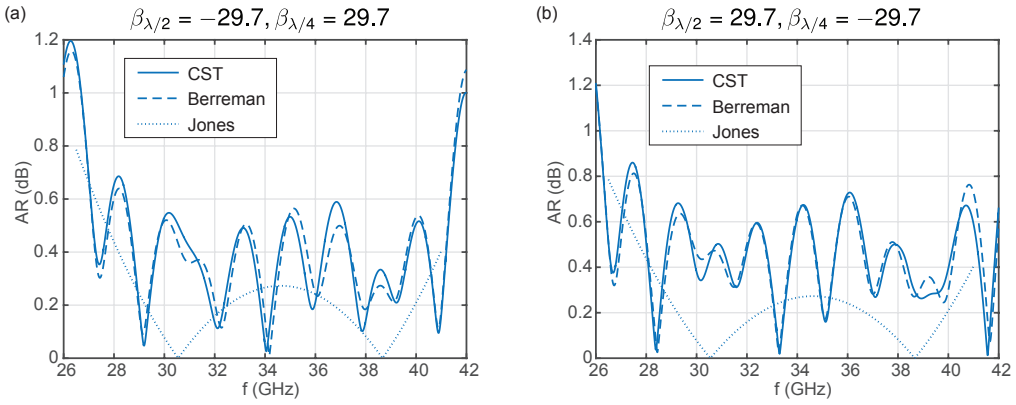

Figure 2.16: Comparison of the AR given by CST simulations, Berreman's and Jones' model when the waveplates are rotated (a) $\beta_{\lambda/2} = -29.7°$ - $\beta_{\lambda/4} = 29.7°$ and (b) $\beta_{\lambda/2} = 29.7°$ - $\beta_{\lambda/4} = -29.7°$.

experiences smoother permittivity transitions yet achieves the required phase-delay for successful LP-to-CP conversion.

The AR given by Berreman's formulation and that simulated with CST Microwave Studio are shown in Fig. 2.16. For the sake of comparison, results given by Jones' calculus have also been included. As expected, Berreman's formalism yields much more accurate results than Jones'. Indeed, the agreement between the AR given by Berreman's and the simulated one is very good for both possible angle combinations. A comparison between Fig. 2.16(a) and 2.16(b) clearly suggests that the order of the rotations does affect the AR realised in practice, contrarily to Jones' prediction. However, the AR in the three cases is below 1 dB within the considered frequency range, demonstrating that Jones' calculus provides a good initial point for the design of this type of converters. Although small deviations can be appreciated between the results given by Berreman's method and the simulations, CST simulations are considerably more time consuming. In addition, the unit-cell boundary conditions applied in the commercial solver considerably restrict the geometry. Since both rotated waveplates must fit into the same unit-cell, the choice of materials –in particular, their widths– is quite limited. Moreover, the design of the unit-cell becomes even more challenging as the number of waveplates increases. Contrarily, these problems do not exist with Berreman's calculus, making it a better candidate for analysing the response of the converter.

In the experiment, the waveplates proposed in section 2.5 were cascaded. Since the

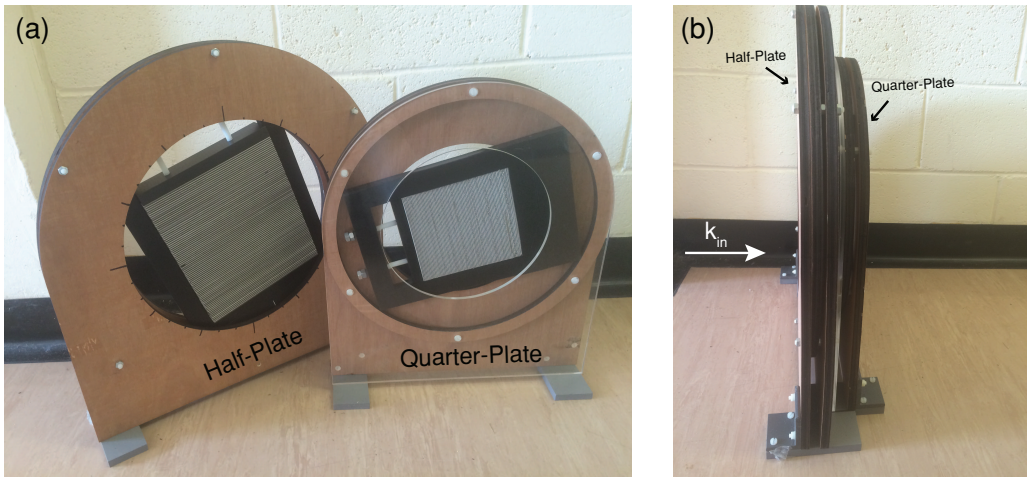

Figure 2.17: Fabricated prototypes. The wooden stands allow for individually rotating the waveplates whilst minimizing separation between the two layers. (a) Front view. (b) Lateral view.

width of the dielectrics available for fabricating the quarter-plate and the half-plate were slightly different, their effective permittivity values also differ. Furthermore, as illustrated in Fig. 2.3, these are also frequency dispersive. Dispersion is more severe in the case of the half-plate than in the quarter-plate due to its longer periodicity. For all these, the approach followed here for flattening the phase-delay, broadening in turn the bandwidth of the converter, can be thought as a combination of that in [36] and [38].

For testing purposes, the two separate wooden stands shown in Fig. 2.17 were fabricated. Each of these contains the plastic frame that supports one of the waveplates, allowing to rotate them individually. This assembly results in a small gap appearing in between the waveplates. The effect of the gap is studied in Fig. 2.18 which shows the calculated AR when the plates are rotated $\beta_{\lambda/2} = -29.7°$ and $\beta_{\lambda/4} = 29.7°$, respectively. The gap was modelled by including a layer of vacuum with thickness s ranging between $0 - 1$ cm that separates the two plates. Fig. 2.18 suggests that the separation distance slightly degrades the performance of the converter. However, the gap is merely caused by the assembly chosen for this specific prototype and could be easily avoided (or at least minimized) by improving the frames or considering a more permanent static solution –e.g. fixing the two plates together. Nonetheless, not being able to rotate the plates individually reduces flexibility in future testing and requires a precise control of the rotation angles which cannot be re-adjusted at

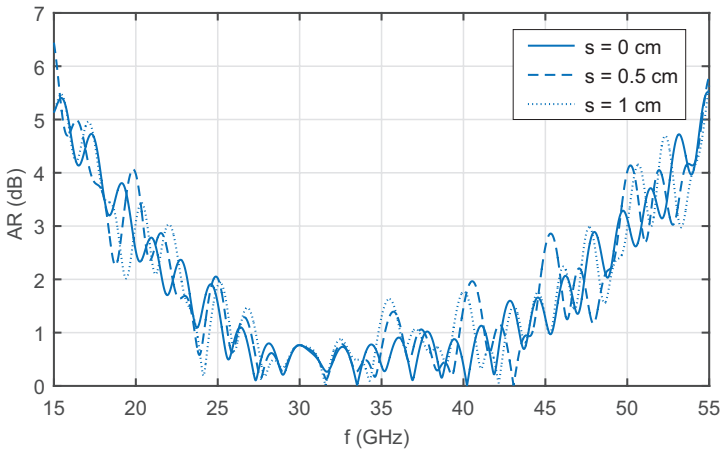

Figure 2.18: Calculated AR when the separation distance between the two waveplates varies between $s = 0 - 1$ cm. Rotations are $\beta_{\lambda/2} = 29.7°$ and $\beta_{\lambda/4} = -29.7°$.

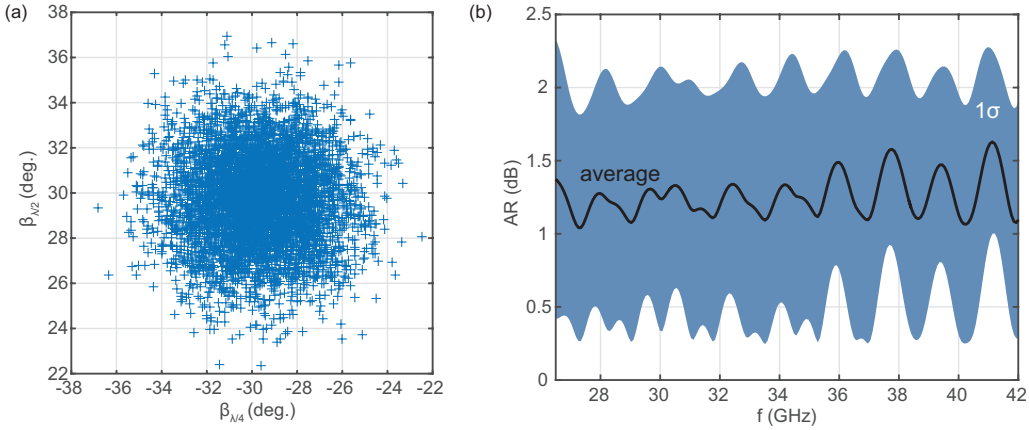

Figure 2.19: Sensitivity analysis to random variations of $\beta_{\lambda/2}$ and $\beta_{\lambda/4}$. (a) $\beta_{\lambda/2}$ and $\beta_{\lambda/4}$ values considered in the analysis. (b) Average AR and 1-σ confidence interval.

a later stage.

The sensitivity of the converter to random variations of $\beta_{\lambda/4}$ and $\beta_{\lambda/2}$ is analysed in Fig. 2.19 using a Montecarlo technique. The 5000 samples ($\beta_{\lambda/4}$, $\beta_{\lambda/2}$) used are shown in Fig. 2.19(a). These were obtained by randomly sampling a 2D Gaussian distribution centred at the original angles $(-29.7°, 29.7°)$ with a $\pm 4°$ deviation. The resulting statistics are summarized in Fig. 2.19(b) where the black curve represents the average AR and the blue areas the 1-σ confidence interval. Our results indicate that the AR remains below 3dB within the frequency range considered with a 68% probability, for errors in the range $\pm 4°$ (above our $\pm 2°$ estimated experimental uncertainty).

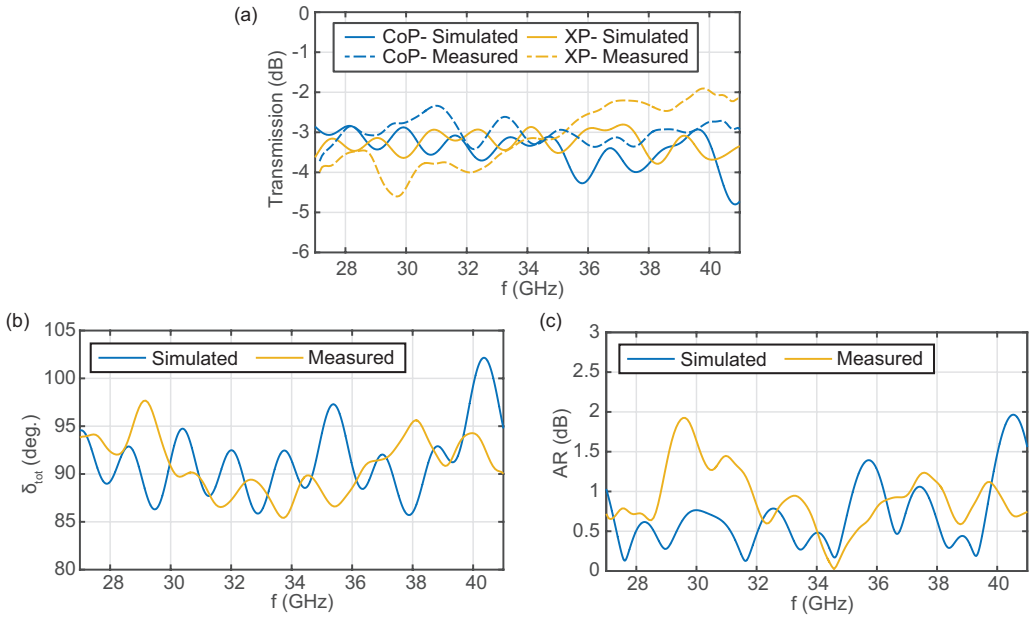

Figure 2.20: Measured and simulated (a) transmission parameters, (b) phase-difference and (c) AR.

The experimental set-up was very similar to that in section 2.5.1, except regarding the excitation. As discussed there, the individual waveplates were characterized by measuring their respective responses to x- and y- polarised radiation. The response to the 45° polarised case was then obtained via superposition. Per contra, here we used 45° polarised radiation directly. The reason for this was twofold. On the one hand, the wooden stands used in this case allowed to rotate the waveplates by arbitrary angles. Hence, a 45° polarised excitation can be obtained very easily, by applying an additional rotation to the two plates. This is significantly simpler than rotating the horn antennas. On the other hand, the multi-plate converter acts not only on the CoP components, as was the case of the individual axis aligned waveplates, but also on the XP ones. As a result, both have to be measured to fully characterize the DUT and this requires rotating the transmitter and/or the receiver. Due to the available equipment, re-positioning the rotated antenna exactly at the same location and with the correct orientation is extremely difficult. The quality of the cables is especially important too, since their response should ideally remain unaltered after the rotation. For all these, the number of rotations should be kept to the minimum. On the other, using the superposition theorem requires 4 measurements: t_{xx}, t_{xy}, t_{yy} and t_{yx}. The number of measurements can be reduced to 2, by using directly a 45° polarised wave: one with the two horns sharing the same

polarisation (CoP) and a second one with opposite polarisation (XP).

The results obtained following this procedure are shown in Fig. 2.20. As can be seen, the simulations and measurements agree reasonably well. Fig. 2.20(a) shows CoP and XP transmission in log-scale. As can be seen, both of them are comparable. This together with the phase-delay between them being close to 90° within the considered frequency range, Fig. 2.20(b), yields an AR below 3 dB within the whole band. Deviations with respect to the simulations are mainly attributed to the limitations of the experimental set up (e.g. border effects and inaccurate repositioning of the antennas).

2.7 Computational costs

A comparison of the computational cost of a single iteration using the different methods employed throughout this chapter is given in table 2.2. A single layer quarter-plate and a two layer system have been considered. As can be seen, Jones' method is orders of magnitude faster than all the other alternatives, with the exception of the TFM which is comparable but limited to single layer axis-aligned waveplates.

Table 2.2: Comparison of computational costs (in seconds)

Layers	Jones	Berreman	TFM	CST
1	0.15s	2.2s	0.6s	73s
2	0.29s	3.1s	-	471s

Despite such computational costs may seem manageable even when a numerical solver is employed (CST), multi-dimensional optimisations typically require hundreds of simulations, e.g. for designing the quarter-plate (1 layer), the CMA-ES required approximately 90 iterations and 520 function evaluations.

2.8 Conclusions

In this chapter, we have theoretically and experimentally demonstrated a new approach for realizing mm-wave all-dielectric waveplates similar to those employed in

optics. The operating principle is based on form birefringence and can be accurately described by an effective anisotropic permittivity tensor obtained via homogenization, as thoroughly discussed in section 2.3. Propagation in such a medium can be described using different models, the most relevant of which can be found in section 2.4. Special attention was drawn to the specific limitations of each model with the aim of assessing suitability depending in the computational cost, accuracy and nature of the problem. In this sense, Jones' calculus is the less consuming model although, generally, also yields lower accuracy, mainly due to neglecting reflections. However, for the prototypes designed here, it still provides acceptable precision.

The designed waveplates can operate as polarisation converters [J1, J2, C1]. In particular, the quarter-plate proposed in section 2.5.2 demonstrated an excellent LP-to-CP conversion performance, comparable to other state-of-the-art technologies in terms of AR, bandwidth, IL and angular stability (Table 2.1) [J1]. A second prototype –a half-plate– showing nearly perfect XP conversion was proposed in section 2.5.3. Lastly, a technique for mitigating frequency dispersion was investigated and experimentally verified in section 2.6 [J2]. There, we showed that the phase-delay can be flattened within a broader frequency range by cascading various waveplates with tailored values of thickness and orientation. This can be exploited for substantially increasing the bandwidth of the converters. In particular, by cascading the quarter- and half-plates previously realised, a LP-to-CP converter with more than double the bandwidth (compared to the individual quarter-plate) was synthesized, proving the flexibility of the proposed structures. The same optimization procedure may be applied to synthesising other types of polarisation converters and, in general, phase-shifters. Likewise, other types of frequency response including multi-band can also be synthesised. Moreover, the presented analytical models may be extended for describing off-normal responses or adapted to include a GP so that the converters operate in reflection, which is particularly relevant for reflect-arrays and reflector antennas.

References

[1] G. Maral and M. Bousquet, *Satellite Communications Systems*, 5th ed. John Wiley & Sons, 2009.

[2] J. Huang, "C.P. microstrip array with wide axial ratio bandwidth and single feed L.P. elements," in *IEEE AP-S 1985 Symposium*, vol. 23, 1985, pp. 705–708.

[3] F. Ferrero, C. Luxey, G. Jacquemod, and R. Staraj, "Dual-band circularly polarized microstrip antenna for satellite applications," *IEEE Antenn. Wireless Propag. Lett.*, vol. 4, pp. 13–15, 2005.

[4] J. Huang, "A technique for an array to generate circular polarization with linearly polarized elements," *IEEE Trans. Antennas Propag.*, vol. 34, no. 9, pp. 1113–1124, 1986.

[5] C. Liu, Y. X. Guo, and S. Xiao, "Capacitively loaded circularly polarized implantable patch antenna for ISM band biomedical applications," *IEEE Trans. Antennas Propag.*, vol. 62, no. 5, pp. 2407–2417, 2014.

[6] N. Fonseca and C. Mangenot, "High-performance electrically-thin dual-band polarizing reflective surface for broadband satellite applications," *IEEE Trans. Antennas Propag.*, vol. PP, no. 99, pp. 1–1, 2015.

[7] M. Navarro-Cia, P. Rodriguez-Ulibarri, V. Torres, and M. Beruete, "Quarter-wave plate based on dielectric-enabled extraordinary resonant transmission," *IEEE Photon. Technol. Lett.*, vol. 24, no. 11, pp. 945–947, 2012.

[8] C. Dietlein, A. Luukanen, Z. Popovic, and E. Grossman, "A W-band polarization converter and isolator," *IEEE Trans. Antennas Propag.*, vol. 55, no. 6, pp. 1804–1809, 2007.

[9] C. W. Haggans, L. Li, T. Fujita, and R. K. Kostuk, "Lamellar gratings as polarization components for specularly reflected beams," *J. Mod. Opt.*, vol. 40, no. 4, pp. 675–686, 1993.

[10] M. Euler, V. Fusco, R. Cahill, and R. Dickie, "325 GHz single layer sub-millimeter wave FSS based split slot ring linear to circular polarization convertor," *IEEE Trans. Antennas Propag.*, vol. 58, no. 7, pp. 2457–2459, 2010.

[11] S. Hollung, W. Shiroma, M. Markovic, and Z. Popovic, "A quasi-optical isolator," *IEEE Microw. Guided Wave Lett.*, vol. 6, no. 5, pp. 205–206, 1996.

[12] Y. Inoue, Y. Ohmori, M. Kawachi, S. Ando, T. Sawada, and H. Takahashi, "Polarization mode converter with polyimide half waveplate in silica-based pla-

nar lightwave circuits," *IEEE Photon. Technol. Lett.*, vol. 6, no. 5, pp. 626–628, May 1994.

[13] Y. Inoue, H. Takahashi, S. Ando, T. Sawada, A. Himeno, and M. Kawachi, "Elimination of polarization sensitivity in silica-based wavelength division multiplexer using a polyimide half waveplate," *J. Lightw. Technol.*, vol. 15, no. 10, pp. 1947–1957, Oct 1997.

[14] C. F. Buhrer, "Four waveplate dual tuner for birefringent filters and multiplexers," *Appl. Opt.*, vol. 26, no. 17, pp. 3628–3632, Sep 1987.

[15] P. A. Williams, "Rotating-wave-plate Stokes polarimeter for differential group delay measurements of polarization-mode dispersion," *Appl. Opt.*, vol. 38, no. 31, pp. 6508–6515, Nov 1999.

[16] S. Bagnulo, M. Landolfi, J. D. Landstreet, E. L. DeglInnocenti, L. Fossati, and M. Sterzik, "Stellar spectropolarimetry with retarder waveplate and beam splitter devices," *Publ. Astron. Soc. Pac.*, vol. 121, no. 883, p. 993, 2009.

[17] K. Iizuka, "Cellophane as a half-wave plate and its use for converting a laptop computer screen into a three-dimensional display," *Rev. Sci. Instrum.*, vol. 74, no. 8, 2003.

[18] J. K. Gansel, M. Thiel, M. S. Rill, M. Decker, K. Bade, V. Saile, G. von Freymann, S. Linden, and M. Wegener, "Gold helix photonic metamaterial as broadband circular polarizer," *Science*, vol. 325, no. 5947, pp. 1513–1515, 2009.

[19] M. Schadt and J. Fnfschilling, "New liquid crystal polarized color projection principle," *Jpn. J. Appl. Phys.*, vol. 29, no. 10R, p. 1974, 1990.

[20] S. H. Chen, D. Katsis, A. W. Schmid, J. C. Mastrangelo, T. Tsutsui, and T. N. Blanton, "Circularly polarized light generated by photoexcitation of luminophores in glassy liquid-crystal films," *Nature*, vol. 397, pp. 506–508, 1999.

[21] M. Born and E. Wolf, *Principles of Optics: Electromagnetic theory of propagation interference and diffraction of light*, 6th ed. Cambridge University Press, 1993.

[22] E. Hecht, *Optics*. Addison Wesley, 1997.

[23] E. Doumanis, G. Goussetis, J. Gomez-Tornero, R. Cahill, and V. Fusco, "Anisotropic impedance surfaces for linear to circular polarization conversion," *IEEE Trans. Antennas Propag.*, vol. 60, no. 1, pp. 212–219, 2012.

[24] A. Jain, P. Tassin, T. Koschny, and C. M. Soukoulis, "Large quality factor in sheet metamaterials made from dark dielectric meta-atoms," *Phys. Rev. Lett.*, vol. 112, p. 117403, 2014.

[25] C. A. Balanis, *Antenna Theory: Analysis and design*, 3rd ed. John Wiley & Sons, 2005.

[26] R. C. Jones, "A new calculus for the treatment of optical systems," *J. Opt. Soc. Am.*, vol. 31, no. 7, pp. 488–493, 1941.

[27] S. Rytov, "Electromagnetic properties of a finely stratified medium," *Soviet Phys. JETP*, vol. 2, no. 3, pp. 466–475, 1956.

[28] J. L. Vilas, L. M. Sanchez-Brea, and E. Bernabeu, "Optimal achromatic wave retarders using two birefringent wave plates," *Appl. Opt.*, vol. 52, no. 9, pp. 1892–1896, Mar 2013.

[29] J. E. Sipe, "New green-function formalism for surface optics," *J. Opt. Soc. Am. B*, vol. 4, no. 4, pp. 481–489, Apr 1987.

[30] D. M. Pozar, *Microwave Engineering*. John Wiley & Sons, 2005.

[31] D. W. Berreman, "Optics in stratified and anisotropic media: 4×4-matrix formulation," *J. Opt. Soc. Am.*, vol. 62, no. 4, pp. 502–510, Apr 1972.

[32] I. J. Martin W McCall, Hodgkinson and Q. hong Wu, *Birefringent thin films and polarizing elements*, 2nd ed. Imperial College Press, 2015.

[33] "Birefringent Thin Films toolbox," http://www.worldscientific.com/worldscibooks/10.1142/p962.

[34] N. Hansen, "The CMA evolution strategy: a comparing review," in *Towards a new evolutionary computation. Advances on estimation of distribution algorithms*. Springer, 2006, pp. 75–102.

[35] I. Zivkovic and A. Murk, "Free-space transmission method for the characterization of dielectric and magnetic materials at microwave frequencies," in *Microwave Materials Characterization*, P. S. Costanzo, Ed. InTech, 2012, ch. 5.

[36] G. Savini, G. Pisano, and P. A. R. Ade, "Achromatic half-wave plate for submillimeter instruments in cosmic microwave background astronomy: modeling and simulation," *Appl. Opt.*, vol. 45, no. 35, pp. 8907–8915, 2006.

[37] C. J. Koester, "Achromatic combinations of half-wave plates," *J. Opt. Soc. Am.*, vol. 49, no. 4, pp. 405–409, Apr 1959.

[38] S. Pancharatnam, "Achromatic combinations of birefringent plates," *P. Indian Acad. Sci. A*, vol. 41, no. 4, pp. 137–144, 1955.

[39] J.-B. Masson and G. Gallot, "Terahertz achromatic quarter-wave plate," *Opt. Lett.*, vol. 31, no. 2, pp. 265–267, Jan 2006.

[40] A. Saha, K. Bhattacharya, and A. K. Chakraborty, "Achromatic quarter-wave plate using crystalline quartz," *Appl. Opt.*, vol. 51, no. 12, pp. 1976–1980, Apr 2012.

[41] J. L. Vilas, L. M. Sanchez-Brea, and E. Bernabeu, "Optimal achromatic wave retarders using two birefringent wave plates," *Appl. Opt.*, vol. 52, no. 9, pp. 1892–1896, Mar 2013.

We build too many walls and
not enough bridges.

Isaac Newton

3

Polarisation conversion via gradient index waveplates and its application to antenna systems

3.1 Introduction

Inhomogeneous materials with spatially varying index of refraction are commonly found in nature. Such is the case of the atmosphere or the human eye, among others [1]. Amid these, Gradient Index (GRIN) media have been widely used in optics and are currently receiving considerable attention in the microwave range, mainly in the field of imaging. Luneburg Lenses (LLs), Eaton lenses or Maxwell fish-eye lenses owe their particular performance to them [2]. Likewise, GRIN media also find application integrated with fiber optics, e.g. as endoscopes for microsurgery [3, 4], and as anti-reflection coatings in a myriad of optical systems [5, 6].

In this chapter, we propose to combine GRIN media with the form-birefringent waveplates presented in chapter 2. Two different designs will be presented. On the one hand, a novel compact highly transparent GRIN quarter plate will be proposed for the first time, offering ∼70% thickness reduction with respect to the standard quarter plate demonstrated in section 2.5.2. On the other, it will be shown how a LL can be integrated with a conformal waveplate to build a highly directive Circular Polarisation (CP) lens antenna.

This chapter is thus divided into two main parts, each one referring to one of the above proposed technologies. Section 3.2 corresponds to the GRIN waveplate [J3]. It begins with a brief introduction to GRIN based anti-reflection coatings. The principle of operation of GRIN waveplates is presented next, in section 3.2.1. There, two different methods for describing the response of a GRIN waveplate are proposed and compared. A compact and transparent quarter plate is subsequently designed. A possible practical realization of the GRIN waveplate, consisting in discretising the refractive index profile, is discussed in 3.2.2. There, the GRIN material is substituted by a collection of homogeneous dielectrics, allowing its simulation with a commercial electromagnetic software: CST Microwave Studio. The required discretisation fineness to avoid degrading the performance of the quarter waveplate is likewise investigated. A comparison with standard form-birefringent waveplates can be found in 3.2.3. Finally, the conclusions are summarized in 3.2.4.

On the other hand, section 3.3 focuses on the integration of the waveplates presented in section 2.5 with LL antennas [J4]. The outline of this second part is as follows. LLs are introduced in section 3.3.1. There, the ideal GRIN spherical LL is compared to its hemispherical version. For easiness of fabrication, a discretised version offering similar performance to the ideal GRIN lens is discussed next. The integration of the discretised hemisphere with a conformal form-birefringent quarter-plate is investigated in section 3.3.2 and the conclusions from this study presented in section 3.3.3.

3.2 Anti-reflection waveplates

GRIN media are typically used as anti-reflection coatings in optical systems [5, 6]. This type of anti-reflection coatings minimize reflections by creating a smooth (graded) transition between the index of refraction of the ambient and that of the substrate, as illustrated in Fig. 3.1. An electromagnetic wave propagating along $\hat{z}$ through such a system would experience a single continuous medium, in turn minimizing reflections due to index mismatch.

Although promising, the form-birefringent waveplates proposed in chapter 2 are limited in terms of bulkiness (which becomes more severe as the range of operation shifts towards lower frequencies) and/or reflections, i.e. high Insertion Loss (IL). The trade-off between this two features makes addressing both simultaneously very challenging. Here, we propose to include GRIN media in the waveplate design in order to overcome this limitation, thus achieving transparency along with compactness.

3.2.1 Gradient index waveplates

A typical form birefringent waveplate consisting of a t-thick sub-wavelength periodic stack of planar dielectric sheets with refractive indexes n_1 and n_2 and widths w_1 and w_2, respectively, is considered in the following, Fig. 3.2(a). A normal incident plane wave with E-field vector $\vec{E} = E_x\hat{x} + E_y\hat{y}$ is assumed. In the metamaterial regime, such a structure can be described using the first order Effective Medium

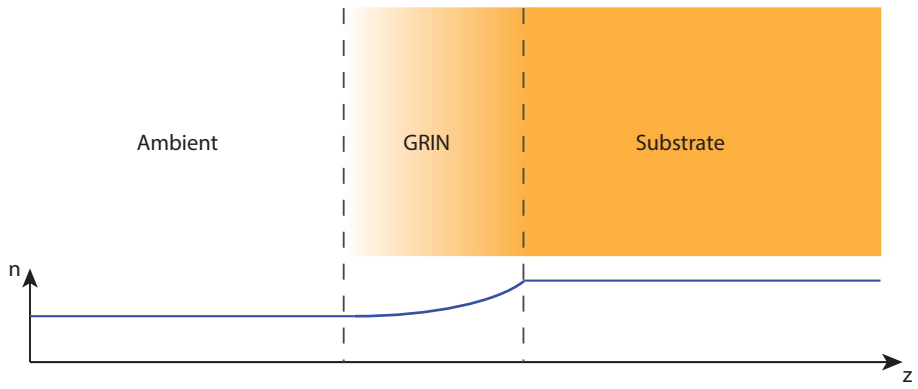

Figure 3.1: GRIN medium acting as an anti-reflection coating between the ambient and a substrate and index distribution as a function of z.

Approximation (EMA) available in section 2.3.1. For non magnetic materials ($\mu = 1$), the permittivity tensor of the effective uni-axial anisotropic medium can be directly translated into a refractive index tensor with components

$$n_{xx} = \left(\frac{f_1}{n_1^2} + \frac{f_2}{n_2^2}\right)^{-1/2}, \tag{3.1}$$

$$n_{yy} = \left(f_1 n_1^2 + f_2 n_2^2\right)^{1/2}, \tag{3.2}$$

where, as in section 2.3.1, f_1 and f_2 are the volume fractions occupied by each medium and $n_{yy} > n_{xx}$ [7].

No restrictions have been imposed yet to n_1 and n_2 which in the standard case are homogeneous. Hereafter, one of the two constituent materials is replaced by a GRIN medium with axial parabolic variation along the direction of propagation

$$n_2(z) = \frac{4(n_\mathrm{o} - n_\mathrm{i})}{t^2}\left(z - \frac{t}{2}\right)^2 + n_\mathrm{i}. \tag{3.3}$$

In (3.3), n_o and n_i represent the refractive indexes at the outer ($z = 0, t$) and inner points ($z = t/2$), respectively. Equation (3.3) can be used in combination with (3.1)-(3.2) to obtain closed-form expressions of the in-plane components of the refractive index tensor of the equivalent medium, $n_{xx}(z)$ and $n_{yy}(z)$. In a reflection-less scenario, the phase-delay introduced upon transmission through the GRIN waveplate can be approximated by the product of the propagation constant and the difference between the light path integral for each field component

$$\delta = \frac{\omega}{c}\int_0^t \left[n_{xx}(z) - n_{yy}(z)\right] dz. \tag{3.4}$$

A GRIN medium with $n_\mathrm{o} = 1$, $n_\mathrm{i} = 2.6$ and $t = 5.9$ mm ($t \sim 0.65\lambda$ where λ corresponds to 33 GHz) is considered next. Its index profile as a function of the distance z from the input interface is shown in Fig. 3.2(b). Planar films made of this material separated by air gaps ($n_1 = 1$) are periodically arranged to build a waveplate, Fig. 3.2(a). The width of the material with n_1 and the GRIN medium are equal ($w_1 = w_2$), causing 50% volume fractions. The effective refractive indexes of the anisotropic equivalent media given by (3.1) and (3.2), and the realised phase-shift according to (3.4) are shown in Fig. 3.2(c) and 3.2(d), respectively. As can be

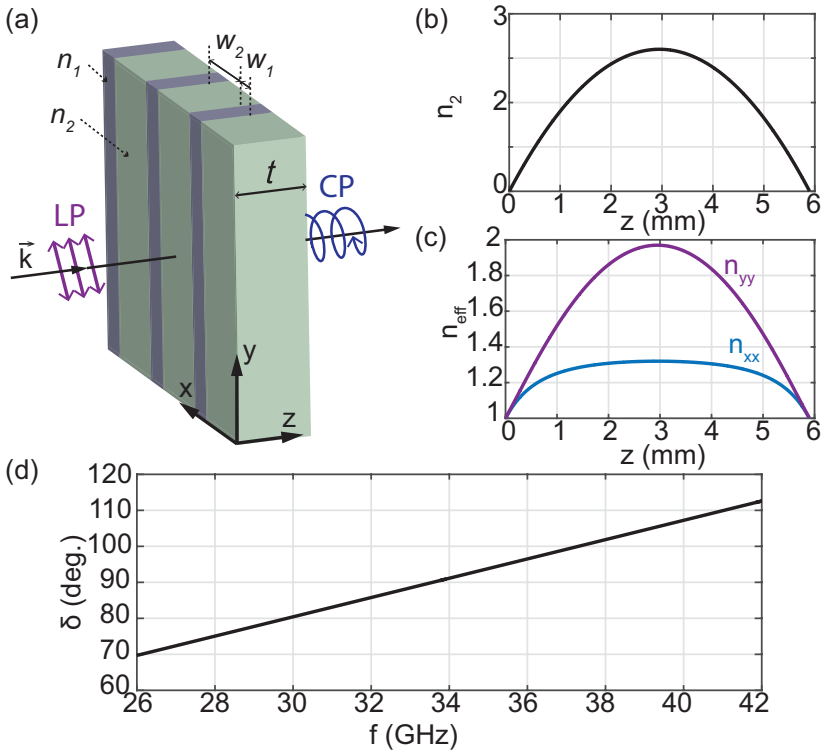

Figure 3.2: (a) Form birefringent waveplate. The dielectric stack extends to infinity in the y-direction and is periodically repeated in x. A normal incident plane wave with E-field contained in the xy-plane impinges the structure. (b) Spatial variation of the refractive index of a $t = 5.9$ mm GRIN medium with $n_{\mathrm{o}} = 1$ and $n_{\mathrm{i}} = 2.6$. (c) Effective refractive index values of a waveplate made of the GRIN medium and air gaps (volume fraction is 50%). (d) Phase-delay between transmitted E-field components.

seen, the waveplate introduces 90° phase-delay (quarter wave retardation) between both E-field components at ∼34 GHz.

Despite the gradual variation of the index, small reflections, which have been neglected up to this point, do exist. As shown in section 2.4.2, a standard form birefringent waveplate is accurately described using a simple transmission line equivalent circuit. Along the same lines, transmission through a GRIN waveplate –or even through a simple GRIN medium– may be understood as a microwave taper. Tapers can be modelled as transmission lines with gradually varying characteristic impedance and are often represented by small discretised sections connected in cascade [8]. As the number of sections approaches infinity, the discretised response approaches the continuous case [8]. Propagation through the GRIN waveplate may be treated analogously, as an anisotropic stratified medium. In this sense, the wave-

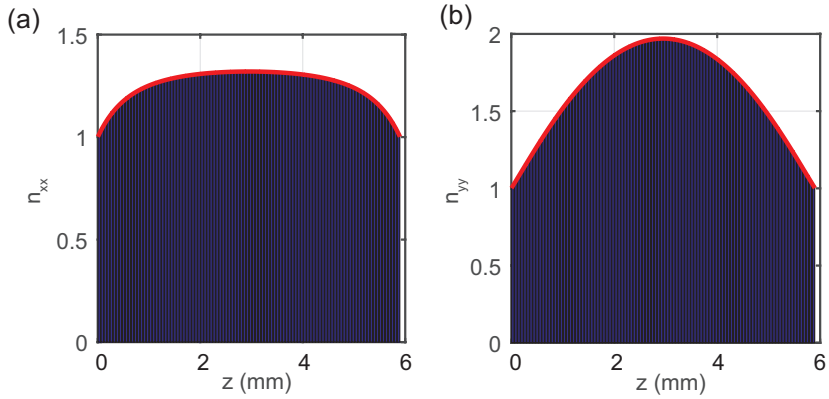

Figure 3.3: Effective indexes of refraction for (a) x- and (b) y-polarised waves obtained after a N = 100 discretisation (blue bars). The ideal GRIN case is shown in red for comparison. Note that the effective index n_{xx} is not parabolic.

plate is discretised in N sections of equally thick homogeneous materials. Finally, the response of such stratified medium can be approximated using the Transfer Matrix Method (TFM) formalism presented in section 2.4.2.

The N = 100 discretisation of the structure shown in 3.3 is considered next. This number of steps suffices for the results to converge to the infinite case. The S-parameters obtained using the TFM method are depicted in Fig. 3.4(a). Reflections are below -9 dB within the considered frequency range, despite the thickness of the waveplate being sub-wavelength. As a result, there is almost total transmission for both polarisations. The maximum difference in transmission levels is below 0.6 dB. The estimated δ and Axial Ratio (AR) given by the TFM method together with that approximated using (3.4) are shown in Fig. 3.4(b) and 3.4(c), respectively. The AR corresponds to that obtained after a Linear Polarisation (LP) plane wave with E-field polarised at 45° with respect to the x-axis propagates through the waveplate. Results obtained through both procedures are slightly different. When reflections are neglected, as is the case in (3.4), the phase-difference increases linearly with frequency, Fig. 3.4(b). On the contrary, the TFM yields a more realistic scenario where reflections are accounted for. These reflections, caused by impedance mismatch not just at the input and output interfaces, as in standard waveplates, but across the whole profile, may result in the formation of a cavity which in turn causes an oscillatory phase-difference. Since in this case reflections are small, the cavity formed is very weak and so is the amplitude of the oscillations in Fig. 3.4(b) and

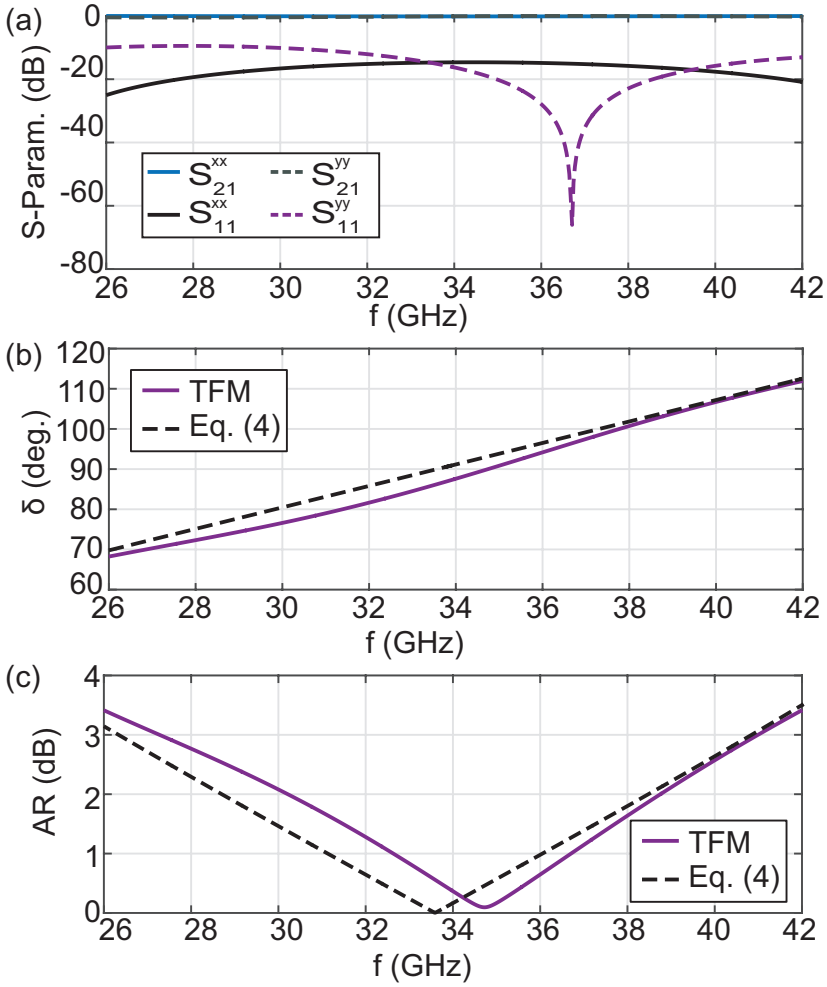

Figure 3.4: (a) S-parameters given by the TFM formalism with N = 100. (b) Phase-delay and (c) AR with (dashed line) and without (solid line) reflections after a LP wave with E-field polarised at 45° from the x-axis propagates through the waveplate.

3.4(c). Despite also present in the transmission parameters, oscillations are easier to appreciate in the reflection parameters in Fig. 3.4(a). Since the transmitted power for both polarisation components is very similar, $\delta = 90°$ produces nearly perfect linear to circular polarisation conversion (AR $\sim$ 0 dB), as suggested by Fig. 3.4(b) and 3.4(c).

The flexibility in the choice of GRIN medium is investigated in Fig. 3.5 where results for different combinations of n_o and n_i are shown. The study is limited to $n_i \geq n_o$. Fig. 3.5(a) shows the optimum thickness of the waveplate for 90° phase-delay at 34 GHz computed from (3.4). The optimum values were obtained using the simplex optimization algorithm. A singularity occurs when the effective indexes match the

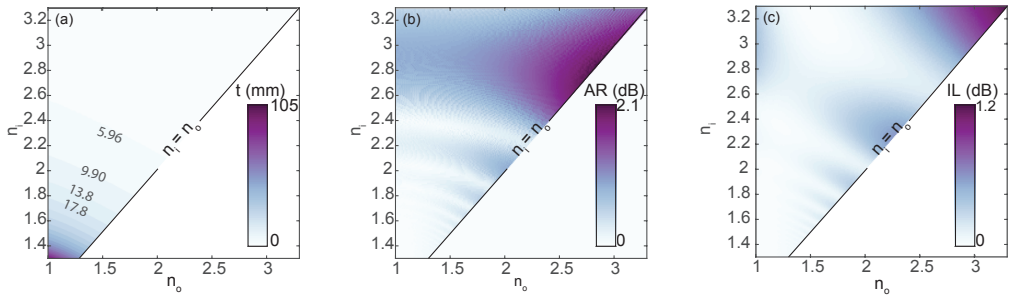

Figure 3.5: (a) Optimum thickness for 90° phase-shift between E_x and E_y. For increased clarity, some values of t (mm) have been included. (b) Realised AR and (c) IL as a function of n_o and n_i for t indicated in (a).

index of the background, i.e. when $n_\mathrm{o} = n_\mathrm{i} = 1$, for which $t \to \infty$ (not shown). For fixed n_o, the required thickness for quarter wave retardation rapidly decreases with increasing n_i (higher index contrast). If n_i is fixed instead, a higher value of n_o results as well in a higher contrast, yielding more compact devices. However, the thickness decrease is slower when n_o is increased instead of n_i.

Fig. 3.5(b) and 3.5(c) show the AR and IL at 34 GHz, respectively, calculated using the TFM when the incident wave is LP at 45° with respect to the x-axis and the waveplate has the thickness shown in Fig. 3.5(a). Note that the achieved AR does not vanish for all the studied cases. The reason for this is twofold. On the one hand, the phase-delay introduced when the thickness is derived from (3.4) differs up to 8° from the TFM model. The differences between these two methods were already shown in Fig. 3.4(b). However, optimization is significantly simplified by using (3.4) and the values estimated following this procedure may provide a good starting point for a subsequent optimization using the TFM or a full-wave electromagnetic solver, in case higher accuracy is required. On the other hand, for a pure CP wave (i.e. AR = 0 dB) the magnitude of each transmitted E-field component shall be equal. Reflections due to the inhomogeneous index distribution cause oscillations in the transmission parameter, and thus in the transmitted power, which in turn deteriorates the polarisation purity. Since the condition $n_{xx} \neq n_{yy}$ shall be satisfied to provide birefringence, coupling of electromagnetic waves to the cavity depends on polarisation. As a result, the power transmitted for each polarisation may differ giving non-zero values of the AR. Remarkably, it remains below 1 dB for most of the indexes combinations, being the maximum AR = 2.1 dB without

any further optimization. Lastly, IL is shown in Fig. 3.5(c). Note that, for lossless dielectrics as those considered here, IL can be merely attributed to reflections. The low IL reported (IL $<$ 1.2 dB) together with the small thickness and low AR prove that GRIN waveplates are an alternative to typical form birefringent waveplates since they enable reducing dimensions and IL simultaneously without compromising performance.

3.2.2 Discretisation of the index profile

Several techniques are available for fabricating GRIN media. Drilling a gradient of sub-wavelength holes on an ordinary dielectric material [9] is among the simpler alternatives. The same effect may be achieved using 3D printing technology [10]. A different approach consists of discretising the index profile and replacing the GRIN medium by a collection of homogeneous dielectrics. The required indexes may be provided by composite materials, e.g. resins loaded with ceramic powders [11]. In preparation for a practical realization, the discretisation is studied in Fig. 3.6.

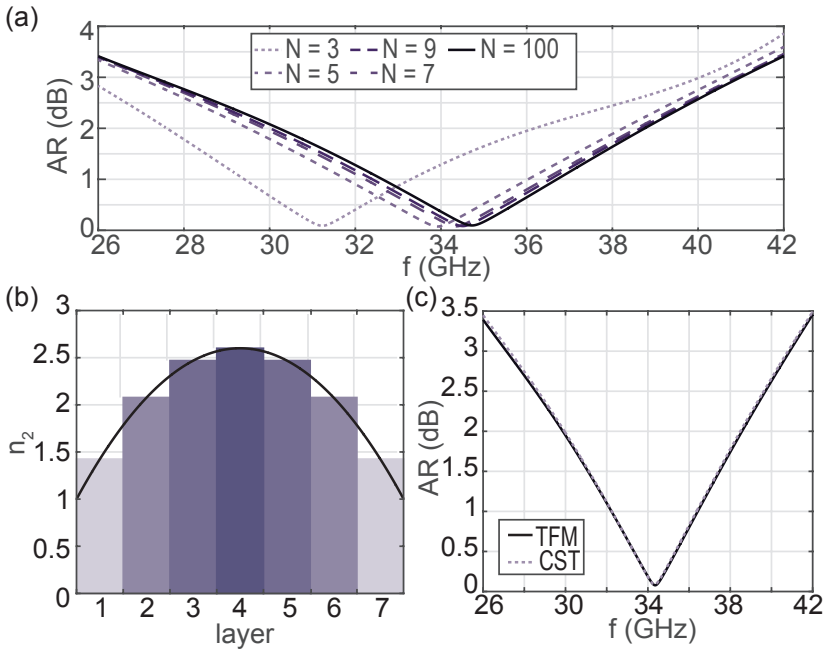

Figure 3.6: (a) AR as a function of the number of discretisation steps. (b) Spatial variation of the continuous (black curve) and N = 7 discretised index profile. (c) AR calculated using the TFM formalism and through full-wave simulations with $w_1 = w_2 = 0.5$ mm.

Fig. 3.6(a) shows the AR obtained from the TFM method with different number of discretisation steps. As can be seen in the figure, results rapidly converge for increasing N. Note that the results obtained with as little as N = 7 are nearly identical to those obtained with N = 100 which suggests that the fabrication of the proposed GRIN waveplate is feasible. The N = 7 case is further investigated in Fig. 3.6(b) and 3.6(c). The index of refraction of the discretised GRIN material is shown in Fig. 3.6(b). For the sake of comparison, the ideal continuous profile has been included. The AR obtained using this configuration is depicted in Fig. 3.6(c). As shown, the AR calculated using the TFM and that obtained via full-wave simulations performed using CST Microwave Studio are in excellent agreement, validating the accuracy of the TFM method.

3.2.3 Comparison with standard form-birefringent waveplates

A comparison between the standard form-birefringent quarter-plate from section 2.5.2 and the GRIN-based one proposed in section 3.2.1 is available in Table 3.1. As can be seen, the performance is very similar. The operating frequency, defined as that of minimum AR is ∼34 GHz, and its minimum value is approximately equal in both cases. Likewise, reflections and thus IL are comparable within the frequency band under consideration. However, the thickness of the waveplate has been reduced by ∼70% in the case of the GRIN waveplate, validating the proposed approach. Note, though, that there are other techniques for reducing the thickness of standard waveplates. For instance, by varying the volume fractions and refractive indexes in (3.1) and (3.2), other combinations of ϵ_{xx} and ϵ_{yy} may be obtained, which may result in thinner profiles without significantly increasing reflections. For instance, combining a large volume of free-space (or other material with index close to 1) with a small volume of a high index material can serve this purpose. However, the required index of the second material increases very rapidly when t is reduced below a critical value. Whether certain materials such as ceramics may exhibit such high indexes of refraction, the necessary low volume fractions –small width– makes them very fragile. Furthermore, since homogenization requires operating in the metamaterial regime, the maximum allowed periodicity, and in turn the width, reduces as the frequency of operation increases. All these problems would be addressed by using GRIN waveplates instead.

Table 3.1: Comparison with a standard quarter-plate

Type	**t (mm)**	**f (GHz)**	**AR (dB)**	**IL$_{\max}$ (dB)**	**S$_{11}^{\max}$ (dB)**
Standard	19.4	34.4	0.08	0.24	-12.68
GRIN	5.9	34.7	0.10	0.28	-12.02

3.2.4 Conclusions

We have shown how GRIN materials can be employed to realise waveplates [J3]. The proposed GRIN waveplates outperform typical form birefringent waveplates as they can exhibit low IL and compact profiles simultaneously which are sought-after features, for instance, in satellite applications. Although standard form-birefringent waveplates may be designed to offer similar performances, they rely in the utilisation of low volume fractions of very high refractive index materials. This results in very fragile devices. Moreover, as the operating frequency increases, the volume fraction reduces, aggravating this problem. Per contra, GRIN waveplates allow similar volume fractions of lower index materials, circumventing this complication. As an example, a quarter-plate has been designed and simulated using a simple reflection-less method and a more rigorous TFM formalism. Our results show a promising $\sim$70% thickness reduction compared to the standard form-birefringent quarter-plate of section 2.5.2. The spectral response obtained via the TFM formalism is in excellent agreement with full-wave simulations. On the other hand, the analytical solution derived in the reflection-less case, may be used to more rapidly evaluate the performance at the expense of reducing the accuracy. However, for low reflection devices as those studied here, it provides reasonable results that shall become the base of a second optimization using a more accurate model, e.g. the TFM method or full-wave simulations, if more precision is desired. Our results suggest that 5 levels of discretisation suffice to implement the GRIN quarter-plate without degrading its performance, which would relax considerably fabrication constraints. Future work shall focus in investigating other manufacturing alternatives. In particular, 3D printing and/or holes gradients. Likewise, the utilisation of asymmetric axially varying index profiles remains unexplored. This unique feature of GRIN waveplates would enable matching to two different media (one of them being free-space) which may be exploited for its integration with other devices such as dielectric lenses.

3.3 All-dielectric Luneburg lens based antennas

In addition to anti-reflection coatings, GRIN materials have been extensively studied in the field of imaging, mainly for implementing dielectric lenses. As early as 1854, Maxwell proposed his fish-eye lens [12]. It consists of a spherical symmetric GRIN medium with radially varying index profile given by

$$n(r) = \frac{n_0}{1 + (r/a)^2}, \tag{3.5}$$

where r is the distance to the centre of the spherical lens, a its radius and n_0 the index of refraction of the background. Such a lens focuses light from a point on its surface to the opposite point within the sphere, Fig. 3.7(a). From a geometrical optics perspective, Maxwell's fish-eye behaves as a perfect lens. Nonetheless, having the source and the image embedded into the lens makes it impractical.

In 1944, Luneburg proposed a second spherical lens capable of focusing parallel rays incident on one side of the sphere into a point at the opposite side [13], Fig. 3.7(b). As Maxwell's fisheye, the LL exhibits spherical symmetry with its index gradually varying according to

$$n(r) = n_0\sqrt{2 - (r/a)^2}. \tag{3.6}$$

In such a distribution, the index of refraction reaches its maximum value at the centre of the sphere and decreases with increased distance to it. Such a lens can focus all the rays in a plane wave impinging its surface to a single focal point at the opposite side. Conversely, if a point source located at its surface acts as the

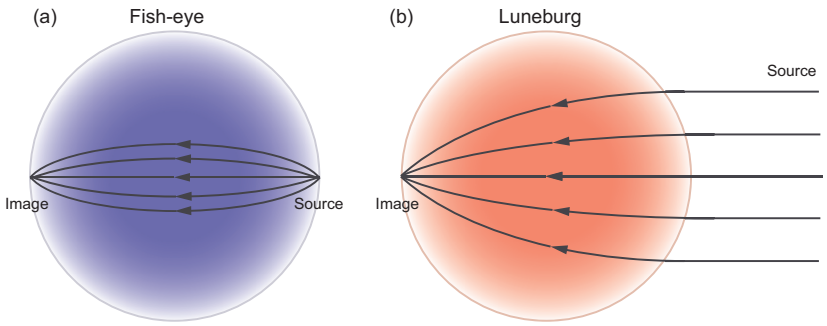

Figure 3.7: Ray trajectories across the cross section of a (a) fish-eye and a (b) LL.

Figure 3.8: (a) Single and (b) ensemble of deployed LL antennas. Courtesy of MATSING RF Lens Technologies.

feed, radiation would focus at infinity. The feed, or alternatively the image plane, lying on the surface of the sphere, the constituent material exhibiting a gradient index profile, and the outer index of refraction being perfectly matched to free-space makes such idealised cases hard to realise in practice. Nonetheless, non-ideal stratified LLs still perform excellently. In this version of the lens, the GRIN material is typically replaced with a collection of concentric shells each of them exhibiting a different homogeneous index of refraction so that the ideal continuous index is discretised [14–16].

The ability to produce multiple simultaneous beams by including multiple feeds or a single scanning feed, makes spherical lenses especially appealing. Similarly to reflector antennas extensively encountered in satellite communication systems, spherical lenses have a primary aperture (the feed) and a secondary aperture (the lens) which is electrically large. As a result, these systems usually offer medium to high directivity values. Additionally, by virtue of their spherical symmetry, LLs outperform reflector antennas in terms of scanning loss, aperture blockage, uniformity of the aperture illumination and cross-polarisation levels [17]. Likewise, they offer higher scan angles than phased arrays with the further advantage of not suffering from grating lobes and not relying on complicated Radio Frequency (RF) circuitry for achieving the beam steering [18]. LLs have been used in microwaves for automotive radar systems [19] and also show promise for communications [20]. Commercial LL antennas are currently being deployed. Some examples of these are shown in Fig. 3.8. Here, we suggest to integrate them together with the form-birefringent

waveplates from chapter 2 to realise all-dielectric highly directive CP antennas.

3.3.1 Linearly polarised Luneburg lenses

Initially, a GRIN LL with radius $a = 40$ mm ($a \sim 4.6\lambda$ where λ corresponds to 34.5 GHz) and index profile described by (3.6) is considered. The lens has been simulated using the Finite Integration Technique (FIT) solver of CST Microwave Studio together with the predefined macro for creating spatially varying materials, which is provided with the 2015 version of the software. A small pyramidal horn antenna with 10° taper angle and 10 mm length acts as the excitation. To this end, the horn is fed with a standard WR-28 waveguide and located with the central point of its aperture lying on the outer surface of the LL, i.e. at the focus. The simulated 3D directivity pattern of the lens-antenna system shown in Fig. 3.9(a) exhibits a very directive pencil beam pointing at $\theta = 0°$ for an operating frequency of 34.5 GHz. Fig. 3.9(b) and 3.9(c) show the directivity patterns at the E- and H-planes, respectively, with and without the lens. The lack of symmetry of the excitation horn

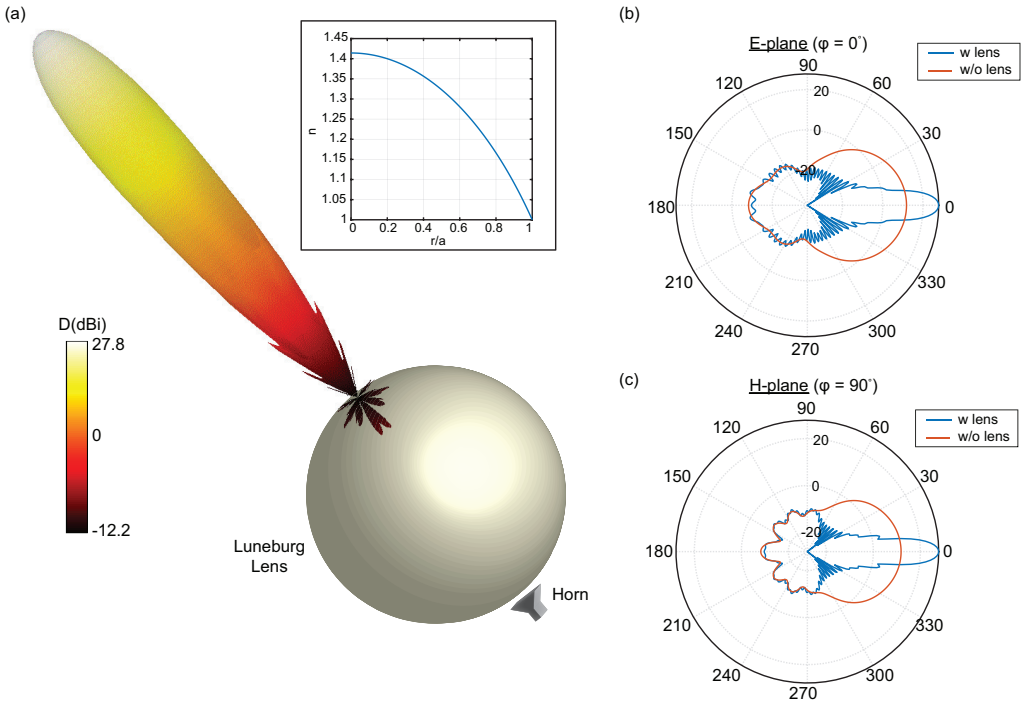

Figure 3.9: (a) 3D directivity pattern (dBi) of the LL antenna system. The inset shows the refractive index profile as a function of the distance to the centre. (b)-(c) Directivity pattern (dBi) at the (b) E- and (c) H-planes with and without the LL.

produces small differences between its E- and H- directivity patterns. These in turn cause the patterns of the LL based antenna to slightly differ as well. As can be seen, the presence of the lens increases the directivity by 16 dB, from 11.8 dBi offered by the horn antenna to 27.8 dBi. The power is confined to a very narrow beam with 7.9° and 7.5° 3dB beam-width and -36.2 dB and -24.5 dB Side Lobe Level (SLL) in the E- and H-planes, respectively.

A very useful variant of the LL is a GRIN hemisphere in conjunction with a Ground Plane (GP). In the ideal case of an infinitely thin GP extending to infinity, image

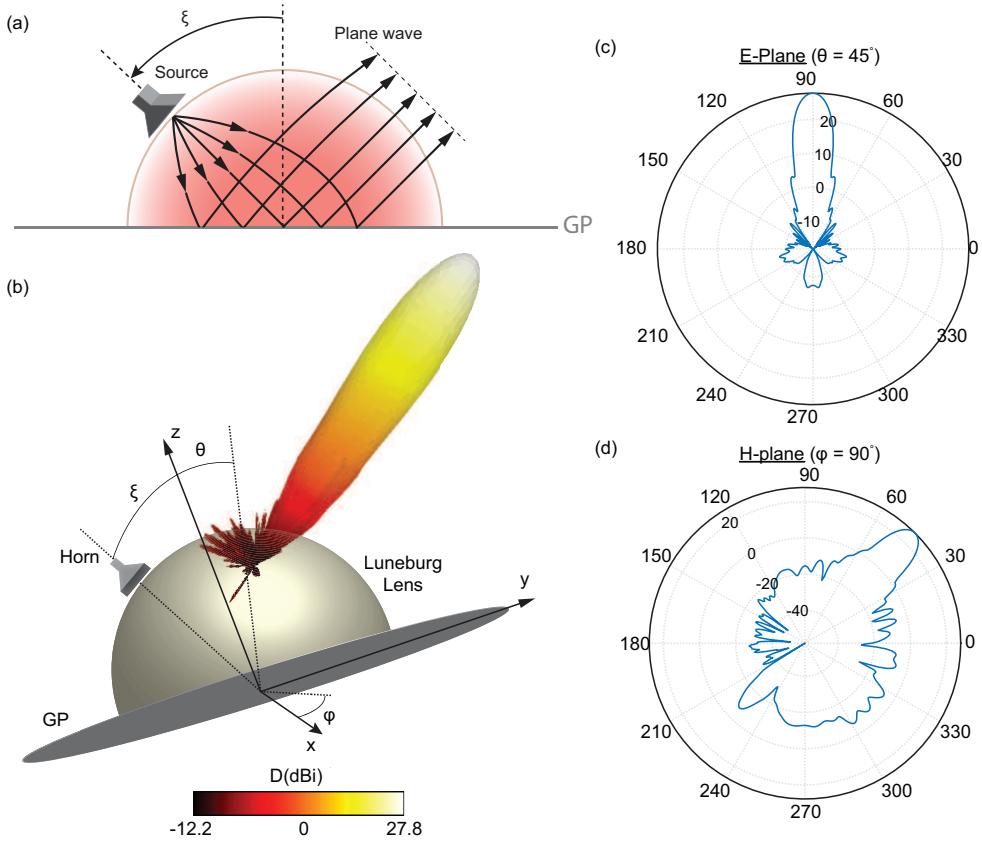

Figure 3.10: (a) Ray trajectories across a section of the hemispherical lens. (b) 3D directivity pattern (dBi) of the LL antenna system. (c)-(d) Directivity patterns (dBi). (c) E- and (d) H-plane.

Table 3.2: Stratified LL hemispherical lens. Radius and refractive index of the shells.

r (mm)	10	20	30	40
n	1.4087	1.3636	1.2686	1.1110

theory predicts an equivalent performance to two hemispheres with reflection symmetry along the GP (one real and a second one virtual) [21]. Hence, one would expect a very similar performance to the spherical version, but with a reduced profile, making the hemispherical LL advantageous for scanning antennas for satellite communications with moving vehicles [22].

A hemispherical lens with radius $a = 40$ mm ($a \sim 4.6\lambda$ where λ corresponds to 34.5 GHz) is considered next, Fig. 3.10(a). The GP is modelled as an infinitely thin Perfect Electric Conductor (PEC) plane. In the simulations, its extension was optimized to approximate the infinite GP case. To avoid aperture blockage, the feed antenna is located at $\xi = 45°$ from the z-axis. The horn is placed at the focus. The simulated 3D directivity pattern shown in Fig. 3.10(b) exhibits a main lobe pointing at $(\theta = 45°, \varphi = 90°)$ with similar width and directivity as that of the traditional spherical LL. Fig. 3.10(c) and 3.10(d) show the directivity patterns at the E- and H-plane, respectively. As can be seen, the main lobe has 10.7° and 7.9° 3dB beam-width and -23.7 dB and -33.8 dB SLL in the E- and H-planes, respectively. This is, the performance of the hemisphere is comparable to the spherical case despite having half the size, as expected from the image theory.

A uniform discretisation of the hemispherical lens is studied in the following. The discretised lens consists of 4 concentric hemispherical shells with equal thickness. The radius of the shells and the refractive index of the constituent homogeneous materials are given in Table 3.2. The directivity patterns obtained in this case are shown in Fig. 3.11(a). A narrow main lobe with 27.7 dBi maximum directivity can be clearly distinguished. Fig. 3.11(a) shows the directivity patterns at the E- and H-planes. The main lobe has 10.7° and 8.1° 3dB beam-width and -27.5 dB and -29.9 dB SLL in the E- and H-planes, respectively. The reflection coefficient is shown in Fig. 3.11(b). This suggests that impedance matching is nearly unaffected by the presence of the lens.

A comparison of the performance of the 3 lenses proposed in this section is in-

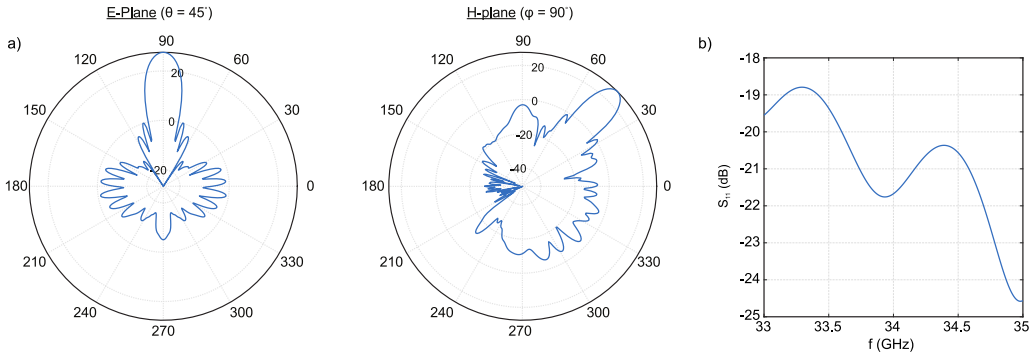

Figure 3.11: (a) E- and H-plane directivity patterns (dBi). (b) Reflection coefficient

Table 3.3: 40 mm radius LL performance comparison.

		E-Plane		**H-Plane**	
Antenna	D_{max} (dBi)	**3dB width**(°)	**SLL** (dB)	**3dB width** (°)	**SLL** (dB)
Spherical	27.8	7.9	-36.2	7.5	-24.5
Hemispherical	27.8	10.7	-23.7	7.9	-33.8
Stratified	27.6	10.7	-27.5	8.1	-26.9

cluded in Table 3.3. In all the cases, a very directive narrow pencil beam with more than 27.7 dBi maximum directivity and less than 10.7° 3dB beam-width is obtained. Likewise, the 3 of them exhibit excellent SLL (< -23.7 dB). These results suggest that hemispherical LLs outperform spherical LLs in terms of dimensions, weight and amount of required materials, whilst offering similar antenna performance. Nonetheless, spherical LLs offer twice the scanning capabilities of its hemispherical counterparts.

3.3.2 Circularly polarised Luneburg lenses

The next goal is to integrate the discretised hemispherical LLs from section 3.3.2, with the form-birefringent quarter-plate presented in section 2.5.2. To this end, the waveplate with thickness $t = 19.4$ mm bends following the hemispherical surface, covering exactly half of it, Fig. 3.12. The waveplate is oriented with the sheets parallel to the GP. A square horn antenna with 15° taper angle and 10 mm length acts as the excitation. This feed is positioned at the focus forming an angle $\xi = 45°$ from the z-axis to avoid blockage. Additionally, the horn has been rotated 45° about its axis to produce the required polarisation for optimum LP-to-CP conversion. The

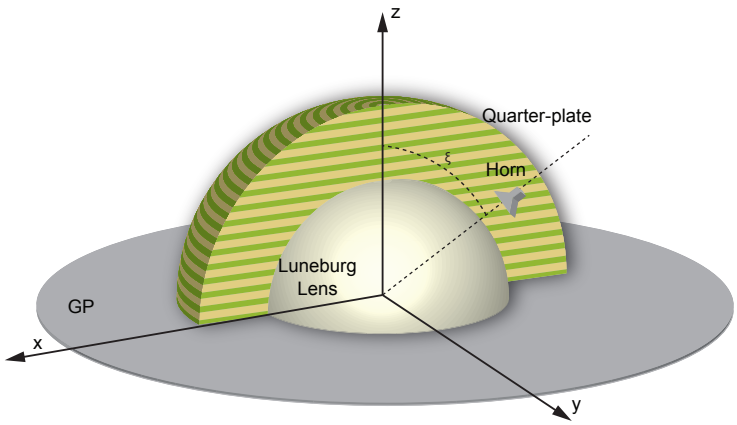

Figure 3.12: Proposed CP LL antenna.

principle of operation can be understood from a geometrical optics perspective. Consider a ray propagating from the horn towards the centre of the hemispherical lens. After reflection at the GP, the ray changes trajectory and propagates through the opposite half of the LL, towards the quarter-plate. The LL transforms the spherical wave-front emitted by the horn, into a nearly planar one at the LL-waveplate interface. Since the wave-front is almost planar when the wave reaches the quarter-plate, its response approximates that presented in section 2.5.2 for plane wave excitation. As a result, the quarter-plate introduces the necessary retardation for the LP wave to become CP before it is radiated to the far-field.

This is confirmed in Fig. 3.13. Fig. 3.13(a) and 3.13(b) show the directivity patterns at the E- and H-planes at 34.5 GHz, respectively, with and without the quarter-plate. The pointing angle of the main lobe shifts very slightly when the quarter-plate is considered, from ($\theta = 48^\circ$, $\varphi = 90^\circ$) to ($\theta = 48.3^\circ$, $\varphi = 90^\circ$). This deviation has been accounted for in the E-plane definition in Fig. 3.13. As can be seen there, including the quarter-plate does not degrade significantly the power patterns. A detailed comparison of the performance with and without quarter-plate can be found in Table 3.4. The main differences arising when the quarter-plate is included are a 1.3 dB directivity maximum reduction (from 27.5 to 26.3 dBi) and an 8.3 dB H-plane SLL increment, which becomes -12.6 dB. In return, the radiation becomes circularly polarised. Fig. 3.13(a) and 3.13(b) show the AR in the vicinity of the main lobe direction at the E- and H-planes, respectively. As can be seen there, the AR is < 1 dB for ($\theta = 48.3^\circ$, $\varphi = 90^\circ$) and < 3 dB for angular deviations smaller than 16° and

20° in the E- and H-planes, respectively. Note that these angular ranges are wider than the 3 dB beam-width, hence assuring that most of the power radiated is CP despite the quarter-plate conforming to the curved surface.

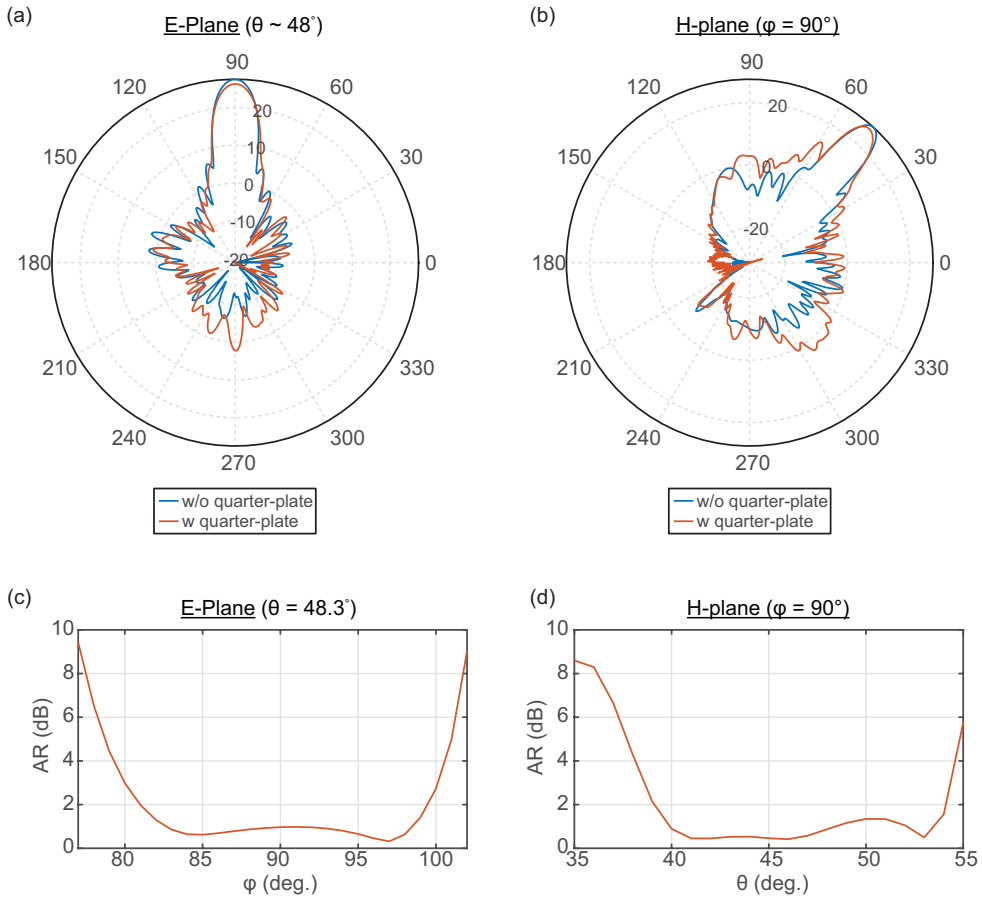

Figure 3.13: (a) -(b) Directivity patterns (dBi) at 34.5 GHz. (c)-(d)

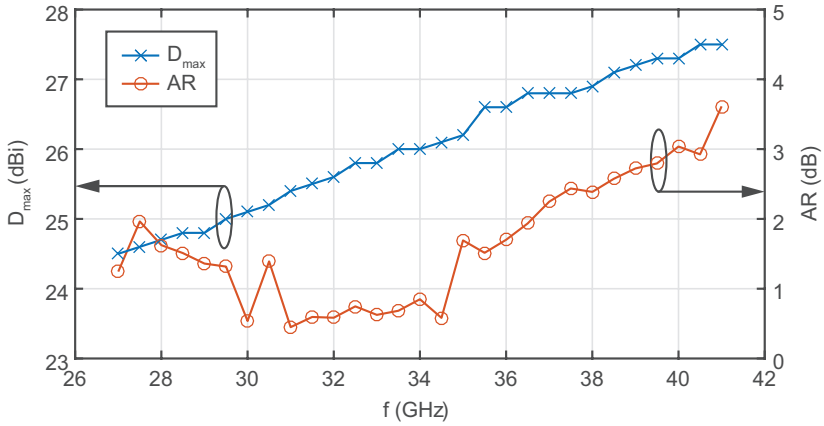

Figure 3.14: Directivity maximum and AR versus frequency. The AR is measured at the direction of maximum directivity.

Table 3.4: LP and CP LL 34.5 GHz performance comparison

		E-Plane		**H-Plane**	
Antenna	D_{max} (dBi)	**3dB width**(°)	**SLL** (dB)	**3dB width** (°)	**SLL** (dB)
LP	27.5	10.2	-24	7.3	-20.9
CP	26.3	10.9	-21.5	8.1	-12.6

Finally, the frequency response of the CP LL is investigated in Fig. 3.14. There, it can be seen that the directivity increases almost linearly with frequency, as is also the case in traditional LP LL [11] excited by horns. From a directivity perspective, the bandwidth is only limited by the source employed, the horn in this case. Per contra, the AR bandwidth is governed by that of the quarter-plate. As shown in the figure, it remains below 4 dB within the frequency range under consideration without any optimization of the structure, which holds promise for this type of CP lenses.

3.3.3 Conclusions

In this section, we have proposed a new approach for obtaining highly directive and high purity CP antennas with low profiles, low SLL and reasonable bandwidth [J4]. Furthermore, this technique may be adapted to operate with other types of lenses, such as cylindral [11] or conformal [C2] LLs, widening the range of potential applications. We departed from a GRIN spherical solution of the LL. Next, it was shown that an hemispherical lens with a GP offers similar performance, as expected from symmetry considerations. For increased feasibility, the hemispherical solution was discretised to give a collection of shells of homogeneous materials, although similarly to the fabrication of the GRIN waveplates, other fabrication methods could be employed (e.g. 3D printing). Finally, the designed discretised lens was integrated with the quarter-plate from section 2.5.2 which is the ultimate responsible of the high purity polarisation conversion obtained. This preliminary study indicates that further studies in this direction are promising and may provide an alternative to current CP reflectors, such as those based on High Impedance Surface (HIS) [23].

References

[1] E. Hecht, *Optics*, 2nd ed. Addison-Wesley, 1987.

[2] E. W. Marchand, *Gradient Index Optics*, United Kingdom ed. Academic Press, 1978.

[3] F. H. J. Koch, K. P. Luloh, A. J. Augustin, M. S. El Agha, H. Guembel, C. Ohrloff, W. S. Grizzard, M. E. Hammer, and S. Sinclair, "Subretinal microsurgery with gradient index endoscopes," *Ophthalmologica*, vol. 211, pp. 283–297, 1997.

[4] B. A. Flusberg, E. D. Cocker, W. Piyawattanametha, J. C. Jung, E. L. Cheung, and M. J. Schnitzer, "Fiber-optic fluorescence imaging," *Nat. Methods*, vol. 2, no. 12, p. 941, 2005.

[5] W. H. Southwell, "Gradient-index antireflection coatings," *Opt. Lett.*, vol. 8, no. 11, pp. 584–586, Nov 1983.

[6] D. Chen, "Anti-reflection (AR) coatings made by solgel processes: A review," *Sol. Energ. Mat. Sol. Cells*, vol. 68, no. 34, pp. 313 – 336, 2001.

[7] M. Born and E. Wolf, *Principles of Optics: Electromagnetic theory of propagation interference and diffraction of light*, 6th ed. Cambridge University Press, 1993.

[8] D. M. Pozar, *Microwave Engineering*. John Wiley & Sons, 2005.

[9] Z. L. Mei, J. Bai, and T. J. Cui, "Gradient index metamaterials realized by drilling hole arrays," *J. Phys. D: Appl. Phys.*, vol. 43, no. 5, p. 055404, 2010.

[10] T. A. Campbell and O. S. Ivanova, "3D printing of multifunctional nanocomposites," *Nano Today*, vol. 8, no. 2, pp. 119 – 120, 2013.

[11] C. Mateo-Segura, A. Dyke, H. Dyke, S. Haq, and Y. Hao, "Flat Luneburg lens via transformation optics for directive antenna applications," *IEEE Trans. Antennas Propag.*, vol. 62, no. 4, pp. 1945–1953, April 2014.

[12] J. Maxwell, "Solutions of problems," *Camb. Dublin Math. J.*, vol. 8, no. 188, 1854.

[13] R. Luneberg, *Mathematical Theory of Optics*. Brown University Press, Providence, Rhode Island, 1944.

[14] H. Mosallaei and Y. Rahmat-Samii, "Non-uniform Luneburg lens antennas: a design approach based on genetic algorithms," *IEEE Antennas Propag. Soc. Int. Symp. Dig.*, vol. 1, pp. 434–437, July 1999.

[15] B. Fuchs, L. L. Coq, O. Lafond, S. Rondineau, and M. Himdi, "Design optimization of multishell Luneburg lenses," *IEEE Trans. Antennas Propag.*, vol. 55, no. 2, pp. 283–289, Feb 2007.

[16] H. Mosallaei and Y. Rahmat-Samii, "Nonuniform Luneburg and two-shell lens antennas: radiation characteristics and design optimization," *IEEE Trans. Antennas Propag.*, vol. 49, no. 1, pp. 60–69, Jan 2001.

[17] J. Thornton and K.-C. Huang, *Modern Lens Antennas for Communications Engineering*. John Wiley & Sons, Inc., Hoboken, NJ, USA., 2013.

[18] Q. Xu and J. Thornton, "Report on steerable antenna architectures and critical RF circuits performance," 2006. [Online]. Available: http://www.capanina.org

[19] B. Schoenlinner, X. Wu, J. P. Ebling, G. V. Eleftheriades, and G. M. Rebeiz, "Wide-scan spherical-lens antennas for automotive radars," *IEEE Trans. Microw. Theory Techn.*, vol. 50, no. 9, pp. 2166–2175, Sep 2002.

[20] J. Thornton, "Scanning Ka-band vehicular lens antennas for satellite and high altitude platform communications," *11th European Wireless Conf.*, pp. 1–6, April 2005.

[21] C. A. Balanis, *Antenna Theory: Analysis and Design*. John Wiley & Sons, 2012.

[22] J. Thornton, "Wide-scanning multi-layer hemisphere lens antenna for Ka band," *IEE P- Microw. Anten. P.*, vol. 153, pp. 573–578(5), December 2006.

[23] K. Agarwal, Nasimuddin, and A. Alphones, "Wideband circularly polarized AMC reflector backed aperture antenna," *IEEE Trans. Antennas Propag.*, vol. 61, no. 3, pp. 1456–1461, March 2013.

Tradition is the illusion of permanence.

Woody Allen

4

Leaky-wave nano-antennas based on arrays of nano-particles

4.1 Introduction

In previous chapters, we proposed novel all-dielectric structures operating in the mm-wave band that can overcome typical limitations associated with metallic structures. The mm-waves region of the electromagnetic spectrum remains one of the most underdeveloped frequency bands. Novel technologies must be envisaged to generate and receive signals at these frequencies at which free-space propagation is also challenging (e.g. poor foliage penetration and high atmospheric path loss). Future communications would benefit from operation at even higher frequencies. For instance, the spectral region corresponding to the Near Infrared (NIR) and optical waves are gaining popularity for high-speed point-to-point optical wireless military and commercial communication systems [1], as well as for intersatellite

communication links [2]. It is also a region in which control of electromagnetic radiation emanating from optical sources, such as organic dye molecules [3], semiconductor quantum dots [4] or diamond colour centres [5] in specific directions with sharp angular characteristics is critical. The use of single photon emitters in combination with optical antennas opens up fascinating new perspectives for quantum information science, providing unique opportunities in quantum computing, communication and metrology, among others [6]. However, as these sources are typically embedded into planar slabs, efficient extraction of the emitted photons is extremely challenging. Different routes have been explored towards improving their extraction efficiency, including microcavities [7,8] and nano-antennas [9–13]. However, the proposed nano-antennas usually rely on plasmonic effects which are inherently lossy, whilst planar and hemispherical microcavities offer poor directivity values or require a very precise positioning of the emitter, respectively. In this chapter, we introduce for the first time the use of Leaky-Wave (LW) antennas similar to those described by Trentini in 1956 [14] in the NIR regime. LW antennas have been extensively used for tailoring the radiation pattern of low directive sources in the microwave regime. They can concentrate the radiated power into highly directive pencil-beams at the frequency of operation and conical beams –radiation focused at a certain scan angle from the vertical axis– above it [15]. A common type of 2D LW antenna consists of a Partially Reflecting Surface (PRS) over a Ground Plane (GP) forming a half-wavelength Fabry-Pérot (FP) cavity. The PRS often comprises one high permittivity dielectric layer [16, 17] or a stack of dielectrics with alternating high and low permittivity values [18, 19]. However, in the latter case, the required number of layers to obtain high directivity is large, leading to devices with increased lateral profiles. PRSs consisting of single-layered metasurfaces, e.g. 2D arrays of metallic patches [15] or slots drilled in metal planes, have been proposed to overcome this limitation [20].

The operating principle can be understood using the simplified FP cavity model illustrated in Fig. 4.1 [14, 21]. A horizontal hertzian electric dipole located just above the GP (at point P) acts as the feeding source. Nonetheless, the model can be adapted to allow arbitrarily positioned sources. Such a source emits outward radially propagating LWs which determine the radiation pattern of the LW antenna [22]. From a geometrical optics perspective, the source emits a ray at an arbitrary angle

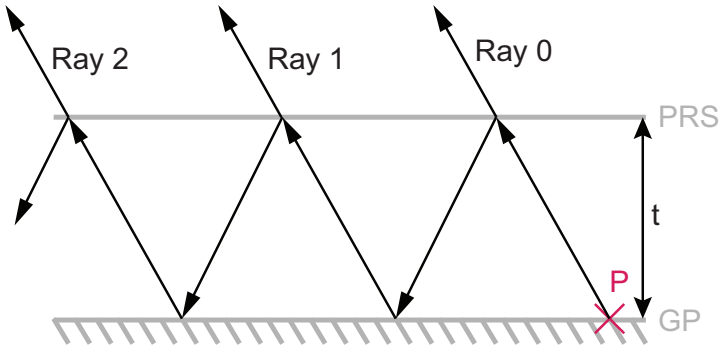

Figure 4.1: Fabry-Pérot cavity model describing the operation of a LW antenna.

α. The highly reflective PRS allows the radiation to leak out, while the GP reflects all the incident power, avoiding power lost in the backward direction. Thus, when the emitted ray reaches the PRS, part of the power is transmitted (ray 0) and part is reflected into the cavity. After reflecting at the GP, a new ray propagates towards the PRS where it is partially transmitted (ray 1) and reflected, and so on. The cavity height can be tailored so that the multiple transmitted waves are in-phase, constructively interfering to enhance radiation in a certain direction, e.g. broadside.

This concept is here tailored to the NIR band to provide significantly enhanced and highly confined electromagnetic fields. In addition, the planar nature of these antennas makes them especially suitable for their integration with planar slabs. As we shift towards higher frequencies the electromagnetic properties of the materials increasingly differ from those at microwaves. At optical frequencies, metals no longer behave as (nearly) Perfect Electric Conductor (PEC). Their permittivity is rather described by a complex frequency dispersive Drude's model, (4.1) [23]. Since metals (and most natural materials) exhibit negligible optical magnetic responses ($\mu = 1$), they are fully characterised by (4.1)

$$\varepsilon_m(\omega) = \epsilon_\infty - \frac{\omega_p^2}{\omega^2 + j\Gamma\omega} \tag{4.1}$$

where ω_p represents the plasma frequency, Γ is the damping frequency and the value at infinity ϵ_∞ is typically chosen for an accurate fitting to experimental data [24].

(4.1) can be re-written as $\epsilon_m(\omega) = \epsilon' + j\epsilon''$ with

$$\epsilon' = \epsilon_\infty - \frac{\omega_p^2}{\omega^2 - \Gamma^2}, \tag{4.2}$$

$$\epsilon'' = \frac{\omega_p^2 \Gamma}{(\omega^2 + \Gamma^2)\omega}. \tag{4.3}$$

The imaginary part, ϵ'', is associated with losses and non-negligible field penetration into metals, (4.6) whilst the real part, ϵ', is directly related to plasmonic effects, which will be the focus of chapter 5. For the purpose of the present chapter, it is enough to notice that plasmon excitation may alter the performance of an antenna –as given by traditional design guidelines– in addition to significantly increase dissipation losses. Per contra, typical dielectric losses are low and usually neglected within the NIR frequency range where alternative loss mechanisms become important, e.g. scattering losses [25].

In the following, nanoparticle arrays are employed to implement PRSs at optical frequencies (section 4.2) for their application to FP LW nano-antennas operating in the NIR part of the electromagnetic spectrum (section 4.3) [J5, C3]. Recent advances in nanotechnology provide the necessary resolution to fabricate arrays of metallic nanoparticles with sub-wavelength features and sufficiently high filling factors required for manufacturing such PRSs [26–28]. Our results show how LW nano-antennas allow to shape the radiation pattern of optical sources. The performance of the nano-antenna is studied using full-wave simulations and the reciprocity theorem. The same approach has been previously validated experimentally in the microwave regime [29]. A detailed explanation of the analysis and the results obtained following this procedure can be found in subsection 4.3.1. To gain a better insight on the effect of the geometry on the performance of the nano-antenna, a parametric study is presented in subsection 4.3.2, where the similarities and differences with traditional LW antennas are highlighted and discussed. Finally, the conclusions are summarised in section 4.4.

4.2 Optical partially reflecting surfaces

A PRS consisting of an infinite grating of square silver (which exhibits low intrinsic losses within the NIR) nano-patches with thickness $t = 20$ nm and side $l = 200$ nm arranged in a 2D square lattice with periodicity $a = 250$ nm is considered, Fig. 4.2(a). The dielectric function of silver is described by (4.1), with $\omega_p = 1.39 \times 10^{16}$ rad/s, $\Gamma = 5.13$ THz and $\epsilon_\infty = 5$ [24]. The PRS is assumed to be embedded in silica

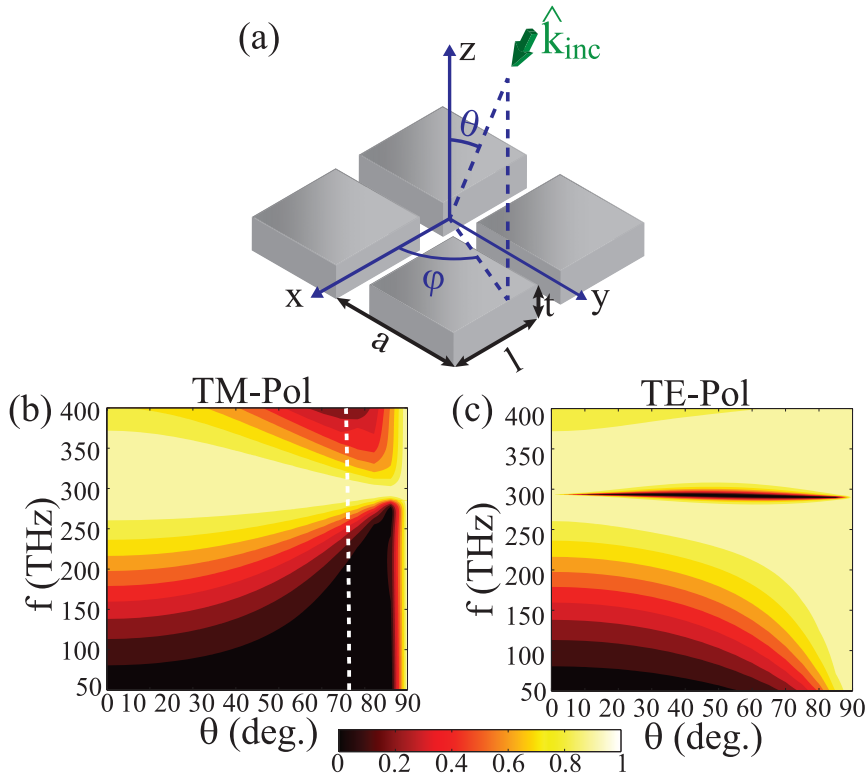

Figure 4.2: (a) Proposed PRS. (b)-(c) Angular reflection spectra of a PRS with $l = 200$ nm, $a = 250$ nm and $t = 20$ nm at $\varphi = 0°$, $90°$ for a (b) TM and a (c) TE polarised wave. The plasmonic Brewster's angle is indicated with a white dashed line.

$(n = 1.45)$.

Fig. 4.2(b) and 4.2(c) show the angular reflectivity spectra for Transverse Magnetic (TM) and Transverse Electric (TE) polarised incident waves, respectively. A maximum at about 300 THz can be observed for both polarisations. At oblique incidence, the TM and TE spectra show some important differences. For a TM polarised wave, Fig. 4.2(b) shows a vertical band (50–260 THz) with almost zero reflectivity that is not present for TE polarisation. This broadband extraordinary transmission effect has been attributed to anomalous perfect impedance matching of the impinging electromagnetic radiation at the plasmonic Brewster's angle in optical plasmonic gratings and can be predicted using a Transmission Line Model (TLM) [30–32].

The condition for anomalous perfect matching is given by

$$\cos\theta_B = \frac{\beta_s(a-l)}{k_0 a n}, \tag{4.4}$$

where k_0 is the free-space wave-number and β_s that in the equivalent transmission line, which can be obtained by numerically solving the following transcendental equation

$$\tanh\left[\sqrt{\beta_s^2 - n^2k_0^2}\frac{a-l}{2}\right]\sqrt{\beta_s^2 - n^2k_0^2} = -\frac{n^2}{\epsilon_m}\sqrt{\beta_s^2 - k_0^2\epsilon_m}. \tag{4.5}$$

As observed in (4.4), the matching condition does not depend on the thickness of the grating. Moreover, it only holds when the metallic nano-particles are optically thick enough to prevent direct transmission through them, i.e. thicker than the skin-depth. The skin-depth δ can be calculated from the conductivity σ of the metal as

$$\delta(\omega) = \sqrt{\frac{2}{\omega\mu_0\mu\sigma}}, \tag{4.6}$$

with $\sigma = \omega\epsilon_0\epsilon''$ where ϵ'' is the imaginary part of the metal's permittivity (4.1).

In our case, the nano-particles forming the PRS are thinner than the skin-depth allowing the incident E-field to penetrate the metal whilst suffering very little absorption. As a result, transmission occurs not only through the gaps between adjacent nano-patches but also through the nano-particles, causing the angle of minimum reflectivity to deviate from that predicted by the TLM (indicated by a dashed line in Fig. 4.2(b)).

When the wave impinging the PRS is TE polarised, a horizontal narrow band of zero reflectivity is observed in Fig. 4.2(c). This wide-angle resonance is originated by the excitation of a localized surface plasmon (LSP) which splits the reflectivity maximum [23]. Similar LSPs are studied in detail in chapters 5 and 6 in different array configurations.

4.3 Fabry-Pérot type leaky-wave nano-antennas

The LW nano-antenna is formed by locating a sufficiently thick silver GP at $h =$ 398 nm from the PRS ($h \sim \lambda/2$). Unless otherwise stated, the nano-antenna is completely embedded in silica, $n_i = n_o = 1.45$, in order to avoid any mismatch effect. The inhomogeneous case, $n_i \neq n_o$, will be discussed later in this chapter.

In [14], it was shown that the magnitude of the reflection coefficient of the PRS determines the maximum directivity of the nano-antenna whilst the pointing angle is related to its phase. The height of our cavity h is slightly shorter than expected from traditional antenna design ($\lambda/2$) due to the non-negligible field penetration into the metal [33]. This effect can be understood as the cavity having an increased effective height.

A y-directed optical source emitting at 252 THz is placed at the centre of the cavity, Fig. 4.3(a). Such a source emits TM_z and TE_z electromagnetic waves which determine the E- and H-planes of the antenna, respectively [22]. Our simulations show that the position of the source along the XY plane has very little effect on the radiation pattern, in contrast to its vertical position, as indicated by the field distribution shown in Fig. 4.3(b). There, a perturbed version of the TM/TE first order mode of the corresponding parallel plate cavity is observed upon excitation of the source. At the frequency of operation, a standing wave in the transverse direction is formed, being the field maximum at $d \sim h/2$. The separation from the source to the free surfaces is sufficient to avoid non-radiative recombinations associated with surface states thus conserving source coherence [34].

4.3.1 Analysis of leaky-wave nano-antennas via the Rayleigh-Carson reciprocity theorem

The performance of the LW nano-antenna is analysed using CST Microwave Studio together with reciprocity. According to the Rayleigh-Carson reciprocity theorem, the receiving pattern of an antenna equals that of its transmission pattern [35]. Therefore, assuming a y-directed optical source at d, the problem of calculating the far-field radiated by the LW nano-antenna reduces to sampling the y-component of the electric near-field at the source position when a plane-wave impinges from any angle of incidence (θ, φ) [36]. The 3D directivity pattern, Fig. 4.3(c), is then obtained as the ratio of the radiation intensity in each direction and the power emitted by the nano-antenna over the whole space [9]

$$D(\theta, \varphi) = \frac{4\pi P(\theta, \varphi)}{\iint P(\theta, \varphi) d\Omega}, \tag{4.7}$$

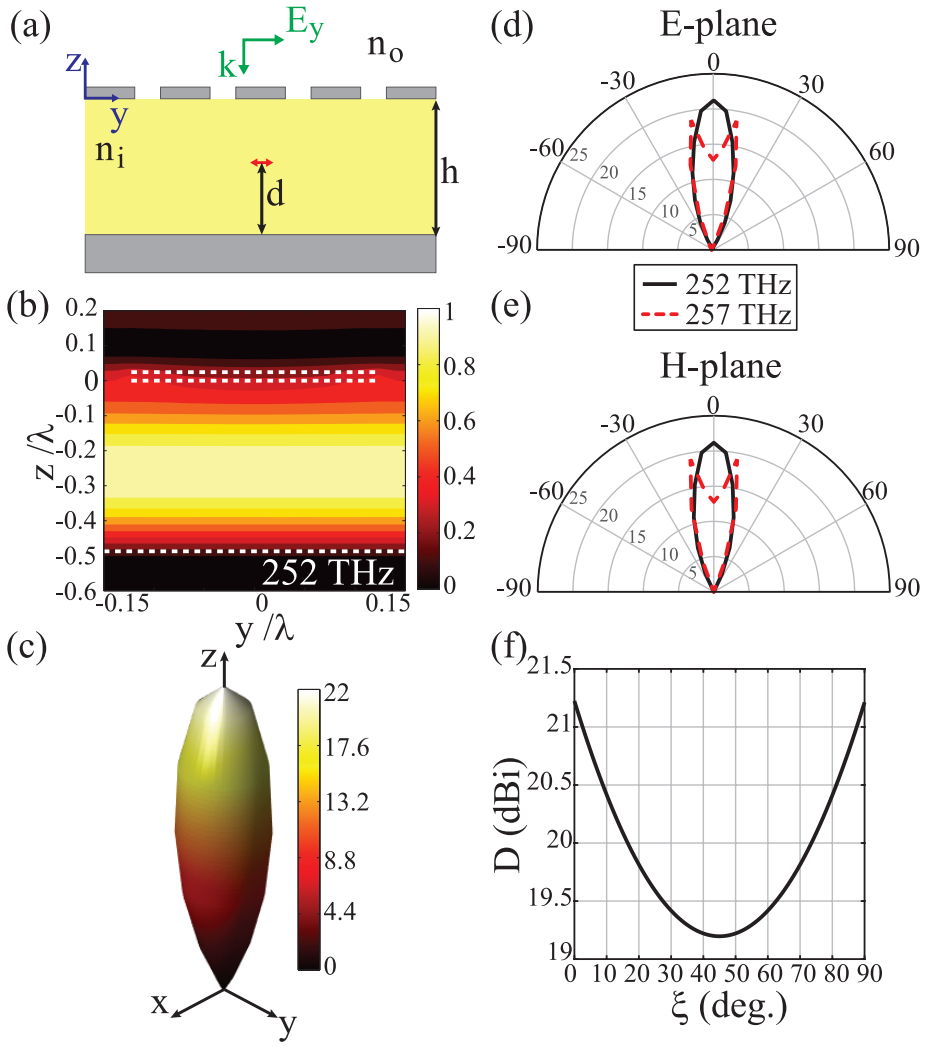

Figure 4.3: (a) Side view of the LW nano-antenna. The source is shown with a red arrow. (b) Normalized E-field distribution at normal incidence. The position of a nanopatch and the GP are indicated with dashed white lines. (c) 3D-Directivity pattern (dBi) of the nano-antenna. (d)-(e) Directivity pattern at the (d) E- and (e) H-plane. (f) Directivity at broadside when the source is oriented at an angle from the y-axis.

where the integration is performed with respect to the solid angle $\Omega = \sin\theta d\theta d\varphi$.

Fig. 4.3(c) shows that the dipole characteristic toroidal pattern has been transformed into a highly directive narrow pencil beam with 13.8° 3dB-angular width at the frequency of operation of the nano-antenna. The directivity at broadside ($\theta = 0°$) is 21.2 dBi. TM-polarised waves impinging at the angle of minimum reflection shown in Fig. 4.2(b) will essentially contribute to the z-component of the E-field to which a horizontal source cannot couple. Thus, no side-lobes are observed regardless of

the reflection minimum in the angular spectra. However, it is worth mentioning that for those sources in which the z-component plays an active role, for instance a vertical dipole, radiation at the plasmonic Brewster's angle should be expected. On the other hand, the wide-angle zero reflectivity band in the TE polarisation response of the PRS observed in Fig. 4.2(c) is above the operating frequency of the nano-antenna, not affecting its performance. The directivity patterns at the E- and H-planes ($\varphi = 90°$ and $\varphi = 0°$, respectively) for two different frequencies depicted in Fig. 4.3(d) and 4.3(e) are nearly symmetrical. Increasing the operating frequency or employing higher cavities, results in the resonant condition of the cavity being fulfilled at oblique incidence. Consequently, the pointing angle increases and the pencil beam turns into a conical beam. This effect is shown with dashed red lines in Fig. 4.3(d) and 4.3(e).

The quantum efficiency η_{q} is given by the ratio between the relative and the total decay [9]

$$\eta_{\mathrm{q}} = \frac{K_{\mathrm{rad}}}{K_{\mathrm{rad}} + K_{\mathrm{nrad}}}, \tag{4.8}$$

where the radiative K_{rad} and non-radiative K_{nrad} decays can be obtained from (4.9) and (4.10), respectively.

$$K_{\mathrm{rad}} = \frac{\iint P(\theta,\varphi)d\Omega}{\iint P_0(\theta,\varphi)d\Omega}, \tag{4.9}$$

$$K_{\mathrm{nrad}} = \frac{P_{\mathrm{diss}}(\theta,\varphi)d\Omega}{\iint P_0(\theta,\varphi)d\Omega}, \tag{4.10}$$

being P_0 the power radiated by an hertzian dipole and P_{diss} the total power dissipated in metals. By substituting (4.9) and (4.10) in (4.8), the quantum efficiency can be written as the ratio of the power emitted by the nano-antenna when metal losses are considered over the loss-less case

$$\eta_q = \frac{\iint P(\theta,\varphi)d\Omega}{\iint P_{\text{loss-less}}(\theta,\varphi)d\Omega}, \tag{4.11}$$

In other words, it is equivalent to the antenna efficiency neglecting the mismatch, i.e. the radiation efficiency from traditional antenna design. In our case, this is 99.7% at 252 THz.

Due to fabrication limitations, a precise control on the orientation of optical sources is extremely challenging –e.g. small organic molecule emitters are synthesised via a solution of dye and polymers, so that typically, the emitters are arbitrarily oriented. Fig. 4.3(f) shows that the directivity at broadside varies less than 2 dB when the source is rotated by an angle ξ about the z-axis, i.e. the performance of the LW nano-antenna here presented is barely affected by orientation changes in the XY-plane, significantly alleviating problems associated with orientation uncertainty. This could be improved further by using alternative lattice configurations, e.g. an hexagonal lattice.

4.3.2 Effect of the geometry of the partially reflective surface on the nano-antenna perfomance

To gain a better understanding of the performance of the nano-antenna, a parametric study of the PRS geometry was performed and its results summarized in Fig. 4.4 and 4.5. The effect of varying the dimensions of the nano-patches is investigated and presented in Fig. 4.4 for a periodicity $a = 250$ nm. Silver's inherent losses are very low in this frequency range. Therefore, larger nanopatches produce more reflective PRSs whilst barely increasing the absorption (red curve in Fig 4.4(a)) which in turn results in higher values of directivity (purple curve). For $l = 200$ nm the directivity at broadside is maximized. Fig. 4.4(b) shows the resonant frequency of the cavity for varying angle of incidence when $l = 200$ nm. It can be observed that, at the operating frequency of the nano-antenna, the resonant condition is fulfilled at broadside. For larger values of l, the gaps between adjacent nano-patches are significantly reduced. As a result, the operating frequency of the nano-antenna is red-shifted, as suggested by Fig. 4.4(c). At higher frequencies, constructive interference is achieved at angles different from broadside, resulting in the beam splitting.

Fig. 4.4(d) shows the directivity at broadside for $l = 180, 190$ and 200 nm. As a consequence of increasing the size of the nano-patches up to the optimum $l = 200$ nm, the 3dB fractional bandwidth is reduced. Coupling of the cavity to the incoming plane wave decreases, resulting in higher external quality factors and thus lower 3dB fractional bandwidths. In particular, for $l = 200$ nm the 3dB bandwidth is 2.8% for a central frequency of 252 THz while for $l = 190$ nm and $l = 180$ nm it is 3.7%

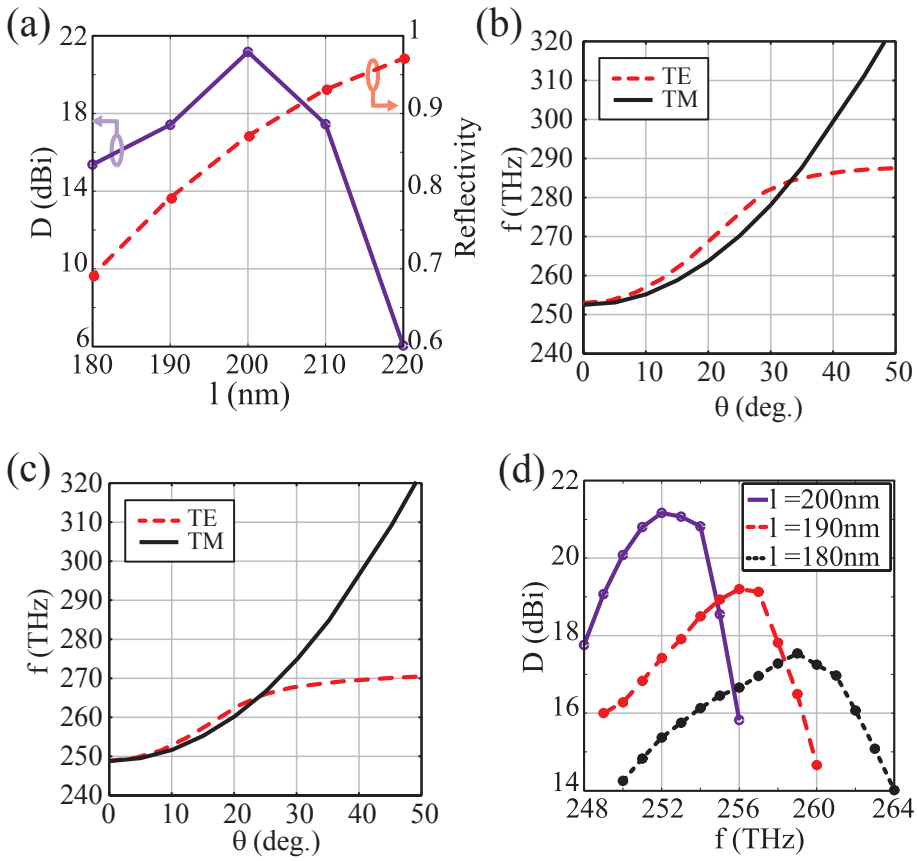

Figure 4.4: (a) Directivity at broadside (right axis) and PRS reflectivity (left axis) at 252 GHz when $a = 250$ nm, $t = 20$ nm, $h = 398$ nm and $l = 180 - 220$ nm. (b)-(c) Resonance frequency vs. θ when (b) $l = 200$ nm and (c) $l = 210$ nm. (d) Directivity at broadside when $l = 180 - 200$ nm.

and 5.1%, respectively. In conclusion, there is a trade-off between directivity and bandwidth. The periodicity also plays a key role in the performance of the nano-antenna. If the period is below the first Bragg resonance ($a < \lambda/2$) such as the case presented here, only the zeroth diffraction order is radiated. Thus, the effect of varying the periodicity within this range can be understood as complementary of that obtained when changing the dimensions of the nano-patches, i.e. it varies the density of patches, and hence the reflectivity of the PRS. The optimum periodicity was found to be $a = 250$ nm.

Typically, when designing LW antennas in the microwave regime, metals are assumed to be good conductors with negligible thickness. This assumption is not valid at the frequency range at hand. Furthermore, the effective height of the cavity depends on the field penetration and hence, on the thickness of the nano-patches.

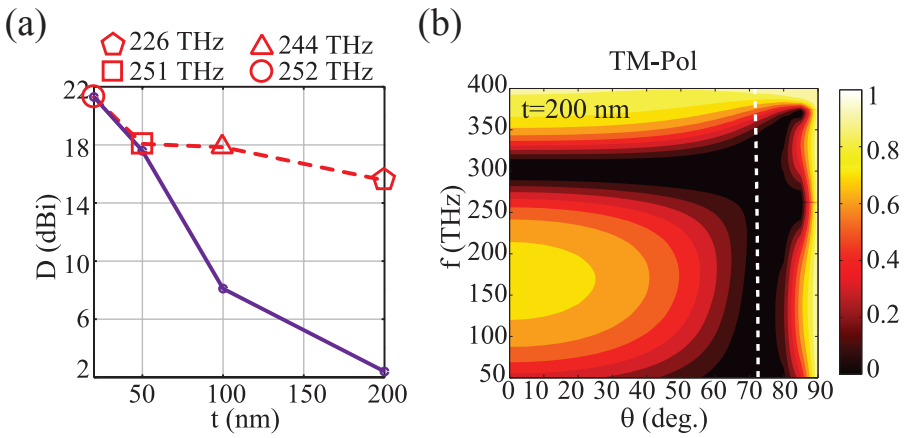

Figure 4.5: (a) Directivity at broadside when $t = 20 - 200$ nm. The purple solid line is the directivity at 252 THz and the red dashed line at the frequencies at which the pencil beam is obtained (indicated in the legend). (b) TM reflectivity spectra when $t = 200$ nm. The plasmonic Brewster's angle is shown with a white dashed line.

The effect of the thickness of the metallic nano-patches in the nano-antenna radiation performance is studied in Fig. 4.5(a). The solid line shows the directivity at broadside at 252 THz for a given cavity height. For $t \neq 20$ nm the radiation pattern has a conical shape, since the nano-antenna is not tuned to the operating frequency. The dashed line shows the directivity at the frequency at which the pencil beam is obtained for the different values of thickness indicated in the figure. For thicker nano-patches, the operating frequency is red-shifted. When the grating is sufficiently thick, i.e. the nano-patches are thicker than the penetration distance, the power is only transmitted through the gaps, diminishing the directivity. Since field penetration is negligible in this situation, the angle of minimum reflectivity and the plasmonic Brewster's angle calculated using the TLM agree excellently, Fig. 4.5(b).

4.3.3 Influence of the environment. The inhomogeneous case.

A more practical scenario consists of a LW nano-antenna surrounded by an inhomogeneous dielectric medium so that the power radiated couples to free-space. In this case, the PRS is assumed to lie on a dielectric medium with refractive index n_i while the surrounding space is vacuum ($n_o = 1$), 4.3(a). This situation is illus-

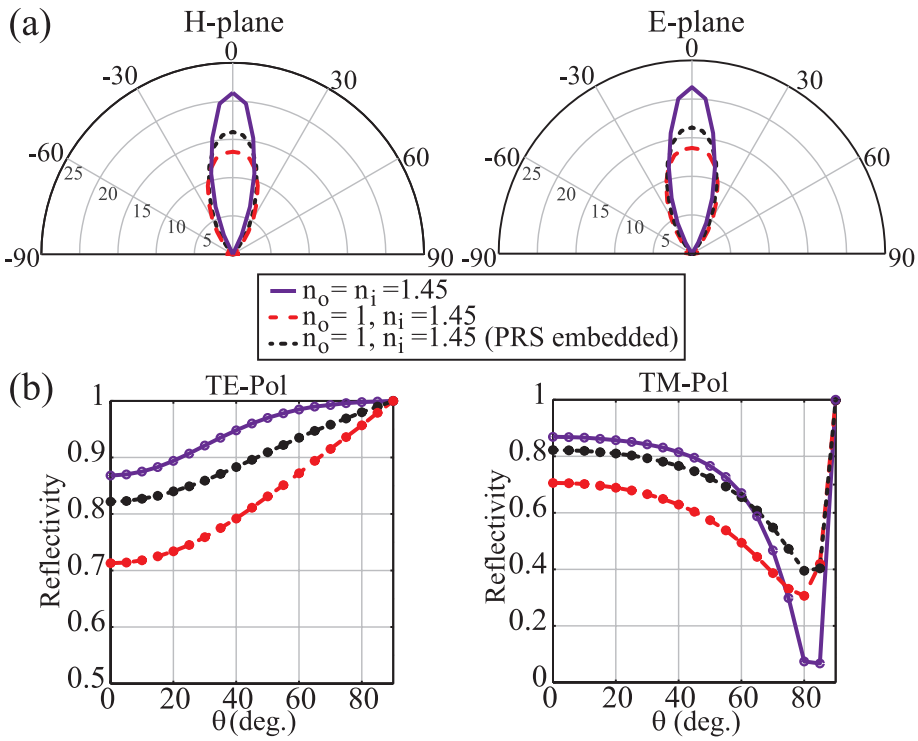

Figure 4.6: (a) Directivity pattern (dBi) at the E- and H-plane when $n_i \neq n_o$ and the PRS lies on top of the silica slab at 266 THz (red dashed line), and when embedded at 259 THz (black dotted line). The homogeneous case (purple solid line) is included for comparison. (b) PRS angular reflectivity spectra for both incoming polarisations.

trated in Fig. 4.6(a) for two cases, namely a PRS laying on top of a silica slab and a PRS embedded in silica. The dimensions of the nano-antenna are equal to those indicated in Fig. 4.2 and 4.3. For the sake of comparison, the LW nano-antenna pattern for $n_i = n_o = 1.45$ has also been included. When the PRS lies on top of the slab, the index mismatch results in reduced directivity, increased beam-width and a blue-shift of the operating frequency. This can be explained by looking at the angular reflection spectra of the PRS in Fig. 4.6(b). Reflectance at normal incidence is much lower than in the homogeneous case. Consequently, the directivity is reduced by 8 dB. The performance can be moderately improved with the embedded PRS which shows a directivity of 16 dBi. Other techniques such as employing gradient index substrates may further enhance the directivity [37].

4.4 Conclusion

In conclusion, we have shown that 2D periodic FP cavity type LW nano-antennas can control the far-field emission of optical sources [J5, C3]. They can tailor the radiation pattern of low directive emitters into very narrow highly directive pencil beams (over 21 dB directivity at broadside). We have also considered the case in which the nano-antenna is embedded in an inhomogeneous substrate. Our results show that the nano-antenna still offers a good performance in this scenario. Its planar nature may ease its integration with embedded sources. In addition, the nano-antenna does not rely on plasmonic effects, with the advantage of reduced non-radiative losses and higher separation to metallic parts than previously reported designs [10]. Lastly, the roles that the cavity height, nano-patches' dimensions and array's periodicity have on the overall performance have been analysed. The results of this study can serve as guidelines for frequency tuning the nano-antenna to other frequencies for its adaptation to different optical sources. Such a device could find many interesting applications in quantum communications and quantum cryptography [6], imaging systems [3] and sensing [38]; for which further investigation in this direction may be promising.

References

[1] O. Timus, "Free space optic communication for Navy surface ship platforms," Ph.D. dissertation, Monterey, California. Naval Postgraduate School, 2004.

[2] T. Tolker-Nielsen and G. Oppenhauser, "In-orbit test result of an operational optical intersatellite link between ARTEMIS and SPOT4, SILEX," *Proc. SPIE*, vol. 4635, pp. 1–15.

[3] Z. Tao, G. Hong, C. Shinji, C. Chen, S. Diao, A. L. Antaris, B. Zhang, Y. Zou, and H. Dai, "Biological imaging using nanoparticles of small organic molecules with fluorescence emission at wavelengths longer than 1000nm," *Angew. Chem. Int. Ed.*, vol. 52, no. 49, pp. 13 002–13 006, 2013.

[4] D. V. Regelman, U. Mizrahi, D. Gershoni, E. Ehrenfreund, W. V. Schoenfeld, and P. M. Petroff, "Semiconductor quantum dot: A quantum light source of

multicolor photons with tunable statistics," *Phys. Rev. Lett.*, vol. 87, p. 257401, Nov 2001.

[5] M. W. Doherty, N. B. Manson, P. Delaney, F. Jelezko, J. Wrachtrup, and L. C. Hollenberg, "The nitrogen-vacancy colour centre in diamond," *Phys. Rep.*, vol. 528, no. 1, pp. 1 – 45, 2013.

[6] H. J. Kimble, "The quantum internet," *Nature*, vol. 453, pp. 1023–1030, 2008.

[7] Y. Ma, P. E. Kremer, and B. D. Gerardot, "Efficient photon extraction from a quantum dot in a broad-band planar cavity antenna," *J. Appl. Phys.*, vol. 115, no. 2, 2014.

[8] Y. Ma, G. Ballesteros, J. M. Zajac, J. Sun, and B. D. Gerardot, "Highly directional emission from a quantum emitter embedded in a hemispherical cavity," *Opt. Lett.*, vol. 40, no. 10, pp. 2373–2376, May 2015.

[9] T. H. Taminiau, F. D. Stefani, and N. F. van Hulst, "Single emitters coupled to plasmonic nano-antennas: angular emission and collection efficiency," *New J. of Phys.*, vol. 10, no. 10, p. 105005, 2008.

[10] R. Esteban, T. V. Teperik, and J. J. Greffet, "Optical Patch Antennas for Single Photon Emission Using Surface Plasmon Resonances," *Phys. Rev. Lett.*, vol. 104, no. 2, p. 026802, Jan. 2010.

[11] A. G. Curto, G. Volpe, T. H. Taminiau, M. P. Kreuzer, R. Quidant, and N. F. van Hulst, "Unidirectional emission of a quantum dot coupled to a nanoantenna," *Science*, vol. 329, no. 5994, pp. 930–933, 2010.

[12] T. H. Taminiau, F. D. Stefani, F. B. Segerink, and N. F. van Hulst, "Optical antennas direct single-molecule emission," *Nat. Photon.*, vol. 2, no. 4, pp. 234–237, 2008.

[13] L. Novotny and N. van Hulst, "Antennas for light," *Nat. Photon.*, vol. 5, no. 2, pp. 83–90, 2011.

[14] G. Trentini, "Partially reflecting sheet arrays," *IRE Trans. Antennas Propag.*, vol. 4, no. 4, pp. 666–671, 1956.

[15] T. Zhao, D. Jackson, J. Williams, H.-Y. D. Yand, and A. Oliner, "2-D periodic leaky-wave antennas-part I: metal patch design," *IEEE Trans. Antennas Propag.*, vol. 53, no. 11, pp. 3505–3514, 2005.

[16] D. R. Jackson and N. G. Alexopoulos, "Gain enhancement methods for printed circuit antennas," *IEEE Trans. Antennas Propag.*, vol. 33, pp. 976–987, Sep. 1985.

[17] D. Jackson and A. Oliner, "A leaky-wave analysis of the high-gain printed antenna configuration," *IEEE Trans. Antennas Propag.*, vol. 36, no. 7, pp. 905–910, Jul 1988.

[18] H. Yang and N. Alexopoulos, "Gain enhancement methods for printed circuit antennas through multiple superstrates," *IEEE Trans. Antennas Propag.*, vol. 35, no. 7, pp. 860–863, Jul 1987.

[19] D. Jackson, A. Oliner, and A. Ip, "Leaky-wave propagation and radiation for a narrow-beam multiple-layer dielectric structure," *IEEE Trans. Antennas Propag.*, vol. 41, no. 3, pp. 344–348, Mar 1993.

[20] T. Zhao, D. Jackson, and J. Williams, "2-D periodic leaky-wave Antennas-part II: slot design," *IEEE Trans. Antennas Propag.*, vol. 53, no. 11, pp. 3515–3524, Nov 2005.

[21] A. Feresidis and J. Vardaxoglou, "High gain planar antenna using optimised partially reflective surfaces," *Inst. Electr. Eng. Proc. – Microw. Antennas Propag.*, vol. 148, no. 6, pp. 345–350, Dec 2001.

[22] A. Ip and D. Jackson, "Radiation from cylindrical leaky waves," *IEEE Trans. Antennas Propag.*, vol. 38, no. 4, pp. 482–488, Apr. 1990.

[23] S. A. Maier, *Plasmonics: Fundamentals and applications.* Springer, 2007.

[24] P. Johnson and R. Christy, "Optical constants of the noble metals," *Phys. Rev. B*, vol. 6, p. 4370, 1972.

[25] R. G. Hunsperger, *Losses in Optical Waveguides.* New York, NY: Springer New York, 2009, pp. 107–128.

[26] B. Päivänranta, H. Merbold, R. Giannini, L. Bchi, S. Gorelick, C. David, J. F. Löffler, T. Feurer, and Y. Ekinci, "High aspect ratio plasmonic nanostructures for sensing applications," *ACS Nano*, vol. 5, no. 8, pp. 6374–6382, 2011.

[27] L. Y. M. Tobing, L. Tjahjana, D. H. Zhang, Q. Zhang, and Q. Xiong, "Deep subwavelength fourfold rotationally symmetric split-ring-resonator metamaterials for highly sensitive and robust biosensing platform," *Sci. Rep.*, vol. 3, no. 2437, pp. 1–6, 2013.

[28] J. Huang, D. Fan, Y. Ekinci, and C. Padeste, "Fabrication of ultrahigh resolution metal nanowires and nanodots through EUV interference lithography," *Microelectronic Engineering*, vol. 141, no. 0, pp. 32 – 36, 2015.

[29] C. Mateo-Segura, A. Feresidis, and G. Goussetis, "Bandwidth Enhancement of 2-D Leaky-Wave Antennas Using Double-Layer Periodic Surfaces," *IEEE Trans. Antennas Propag.*, vol. 62, no. 2, pp. 586–593, 2014.

[30] A. Alù, G. D'Aguanno, N. Mattiucci, and M. J. Bloemer, "Plasmonic Brewster Angle: Broadband Extraordinary Transmission through Optical Gratings," *Phys. Rev. Lett.*, vol. 106, no. 12, p. 123902, Mar. 2011.

[31] C. Argyropoulos, G. D'Aguanno, N. Mattiucci, N. Akozbek, M. J. Bloemer, and A. Alù, "Matching and funneling light at the plasmonic Brewster angle," *Phys. Rev. B*, vol. 85, no. 2, p. 024304, Jan. 2012.

[32] K. Q. Le, C. Argyropoulos, N. Mattiucci, G. D'Aguanno, M. J. Bloemer, and A. Alù, "Broadband Brewster transmission through 2D metallic gratings," *J. Appl. Phys.*, vol. 112, no. 9, p. 094317, 2012.

[33] L. Novotny, "Effective wavelength scaling for optical antennas," *Phys. Rev. Lett.*, vol. 98, no. 266802, pp. 1–4, 2007.

[34] J. Johansen, S. Stobbe, I. Nikolaev, T. Lund-Hansen, P. Kristensen, J. Hvam, W. Vos, and P. Lodahl, "Size dependence of the wavefunction of self-assembled InAs quantum dots from time-resolved optical measurements," *Phys. Rev. B*, vol. 77, no. 7, Feb. 2008.

[35] J. Carson, "A generalization of the reciprocal theorem," *Bell Syst. Tech. J.*, vol. 3, pp. 393–399, 1924.

[36] T. Zhao, D. R. Jackson, J. T. Williams, and A. A. Oliner, "General formulas for 2-D leaky-wave antennas," *IEEE Trans. Antennas Propag.*, vol. 53, no. 11, pp. 3525–3533, Nov 2005.

[37] N. T. Nguyen, R. Sauleau, and C. J. Martínez Pérez, "Very broadband extended hemispherical lenses: Role of matching layers for bandwidth enlargement," *IEEE Trans. Antennas Propag.*, vol. 57, no. 7, pp. 1907–1913, 2009.

[38] R. Schirhagl, K. Chang, M. Loretz, and C. L. Degen, "Nitrogen-vacancy centers in diamond: Nanoscale sensors for physics and biology," *Annu. Rev. Phys. Chem.*, vol. 65, no. 1, pp. 83–105, 2014.

Who are you going to believe,
me or your own eyes?

Groucho Marx

5

Magnetic and electric hot-spots in plasmonic nano-particle gratings

5.1 Introduction

Metallic gratings respond differently to optical waves than they do to microwaves. For instance, the angular response of the Partially Reflecting Surface (PRS) designed in the previous chapter showed abnormal zero reflections bands (section 4.2) which were attributed to plasmonic effects. As these are not described by traditional antenna design principles, they can severely alter the operation of the antenna. To avoid any performance degradation, they must be accounted for during the early stages of the design process. To this end, understanding their physical origin, their effects, as well as how they interfere with other electromagnetic phenomena, or how they are affected by variations of the geometry is critical. Whereas the plasmonic Brewster angle is well documented in the literature [1–3], there is limited information

about localised Edge Plasmons (EPs), and most of the available studies focus on isolated nano-particles rather than arrays [4,5]. In this chapter, we will numerically investigate these localised plasmonic modes in depth.

The origin of plasmons can be traced to (4.2). From (4.2), it can be observed that ϵ' is negative below a certain frequency. Within this range, metallo-dielectric interfaces support bounded modes associated with collective charge oscillations: Surface Plasmon Polaritons (SPPs) [6]. The unique properties of SPPs enable a wide range of nanophotonic applications, such as sub-wavelength imaging [7], single molecule sensing [8] and invisibility cloaking [9]. Additionally, plasmonics allows breaking the diffraction limit for the localization of light into sub-wavelength dimensions, enabling strong field enhancements [10, 11]. Since light-matter interaction is mostly mediated by the electric component of the electromagnetic field, with the magnetic component usually being considered negligible [12], typically only electric enhancement is realised [13, 14]. Nonetheless, it has been shown that properly engineered metallic nano-structures can provide optical magnetic responses thanks to real or virtual electric current flows. These may not only result in strong electric hot-spots, but also in strong concentrations of the magnetic field [15–18]. Hence, both electric and magnetic nano-antennas can be implemented in virtue of the excitation of SPPs.

Here, we focus on metallic nano-particles Localised Surface Plasmons (LSPs) (section 5.2). An infinite plasmonic waveguide with circular cross-section is initially investigated (subsection 5.2.1), as the supported modes are well known and can be obtained analytically [19]. Similar modes arise when finite waveguides –nano-rods– are considered, i.e. when the length of the waveguide enables Fabry-Pérot (FP) cavity resonances. These cavity modes are discussed in subsection 5.2.2. A different scenario consists of a very short section of waveguide: a nano-disk. In this case, the waveguide modes become evanescent and other resonant effects become more important, e.g. EPs. A thorough analysis of such EPs can be found in subsection 5.2.3 [J6, C4]. Arranging the nano-particles in arrays offers additional degrees of freedom for tailoring their interaction with light. Studying the LSPs supported by nano-particles' arrays is the scope of section 5.3. In section 5.3.1, it is shown that, as expected, the individual nano-particles LSPs are also present in this configuration. Among them, nano-disks' EPs are investigated in section 5.3.1, where special attention is paid to the required conditions for their coupling to incident light and the

effect of the geometry. However, these EPs are not the only LSPs supported by arrays. FP modes producing strong field concentrations in the gaps between adjacent nano-particles (section 5.3.2) are also supported. In section 5.3.2, it is shown that depending on the configuration, such modes may originate electric and/or magnetic hot-spots [J7]. Finally, the conclusions are presented in section 5.4.

5.2 Localized surface plasmons in individual nano-particles

SPPs are bounded electromagnetic waves which propagate along metallo-dielectric interfaces and are confined to their vicinity, arising from collective charge oscillations. A special case of coherent oscillations may arise when the interfaces form closed surfaces, as is the case of nano-particles. The resulting non-propagating modes, referred to as LSPs, depend on the shape, size and background of the nano-particles, and are responsible for two important phenomena: a) strong field enhancements localized to the nano-particle surface, and b) strong absorption and scattering peaks at the resonant frequencies [10].

Interestingly, LSPs have been unknowingly exploited by artists since ancient times. A unique piece which owes part of its beauty to the particular optical response of LSPs is Lycurgus cup, two photographs of which are shown in Fig. 5.1. The cup is made of ruby glass, which contains sub-wavelength gold nano-particles that are responsible for the colour change that the cup undergoes under different illumination conditions. In daylight, Lycargus cup shines green (left image), whilst it becomes red when illuminated from the inside (right image). The reason behind the colour change is the gold nano-particles embedded in the glass exhibiting a Localised Surface Plasmon Resonance (LSPR) in the red region of the visible spectrum. Similarly, the rich bright colours embellishing many cathedral windows fabricated, for instance, from stain glass, also involve the excitation of LSPs. More recent applications of LSPs include high absorption photovoltaic cells for more efficient energy harvesting [21], as well as ultra-fast switching, frequency conversion and optical signal modulation via enhanced non-linear effects [22], among others. Likewise, the high sensitivity of LSPs to the nano-particle's surrounding environment makes them particularly

Figure 5.1: Lycurgus cup (British museum; 4th century AD). The cup undergoes a colour change under different illumination conditions. Reproduced from [20].

suitable for high performance sensing applications [23, 24].

5.2.1 Plasmonic waveguides with circular cross-section

A common problem in any electromagnetism course consists of an electromagnetic wave propagating inside a hollow waveguide whose walls are made of Perfect Electric Conductor (PEC). This problem can be solved by enforcing PEC boundary conditions at the waveguide walls, i.e. the tangential electric component equals zero ($E_{\parallel} = 0$). Nonetheless, since metals in the optical range behave different to PEC, the wave-guiding problem must be revisited.

A waveguide consisting of a circular cylinder of radius r and infinite length embedded in an infinite homogeneous medium is considered. Its cross-section is depicted in Fig. 5.2. Without loss of generality, the cylinder is oriented along the z-axis. The frequency dependent permittivity of the cylinder is $\epsilon_C(\omega)$, whilst that of the surrounding medium is $\epsilon_D(\omega)$. No restriction is imposed as yet upon neither of them. In this configuration, the fields are a combination of trigonometric, exponential and Bessel functions (appendix C). In particular, the field components in cylindrical coordinates are given by [19, 25]

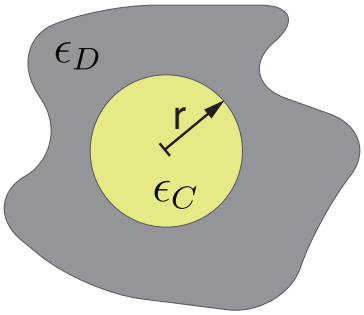

Figure 5.2: Cylindrical waveguide with r-radius circular cross section. The cylinder is made of a material with permittivity ϵ_C and surrounded by a homogeneous medium with permittivity ϵ_D.

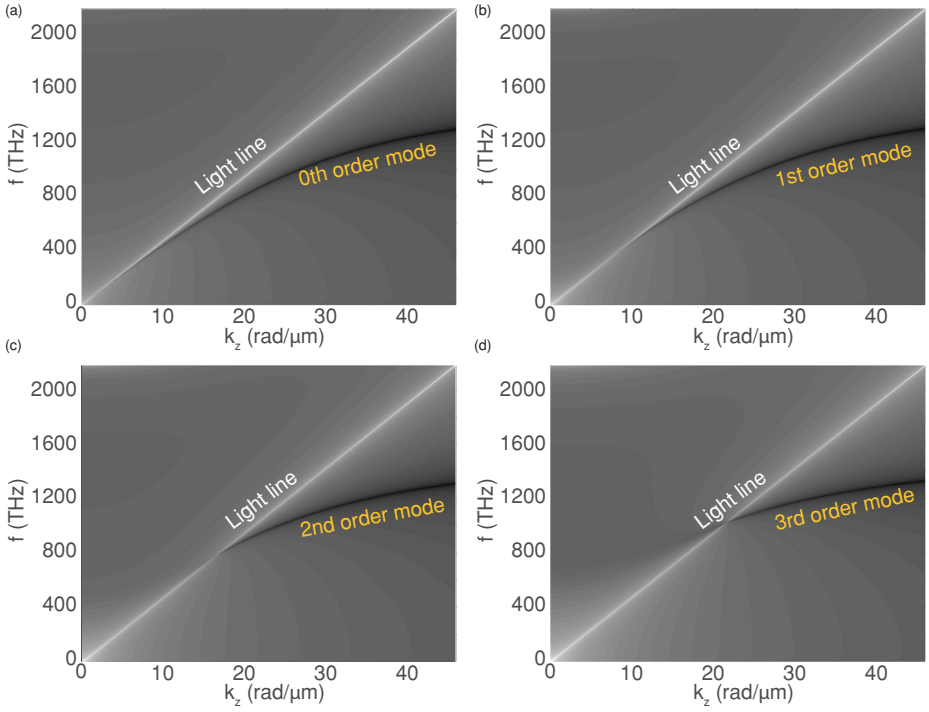

Figure 5.3: Dispersion relation of the lower order modes of a free-standing infinite Ag nanowire with 160-nm-radius circular cross-section in free-space. (a) $n = 0$, (b) $n = 1$, (c) $n = 2$ and (d) $n = 3$. Darker shades represent smaller values. The light-line is shown in white.

$$E_\rho = \left[\frac{jk_z}{K_i} Z_n^{i\prime}(K_i\rho)a_n^i - \frac{\mu_i\omega n}{K_i^2\rho} Z_n^i(K_i\rho)b_n^i\right] S_n, \tag{5.1}$$

$$E_\varphi = -\left[\frac{nk_z}{K_i^2\rho} Z_n^i(K_i\rho)a_n^i + \frac{j\mu_i\omega}{K_i} Z_n^{i\prime}(K_i\rho)b_n^i\right] S_n, \tag{5.2}$$

$$E_z = \left[Z_n^i(K_i\rho)a_n^i\right] S_n, \tag{5.3}$$

$$H_\rho = \left[\frac{n(K_i^2+k_z^2)}{\mu_i\omega K_i^2\rho} Z_n^i(K_i\rho)a_n^i + \frac{jk_z}{K_i} Z_n^{i\prime}(K_i\rho)b_n^i\right] S_n, \tag{5.4}$$

$$H_\varphi = \left[\frac{j(K_i^2+k_z^2)}{\mu_i\omega K_i} Z_n^{i\prime}(K_i\rho)a_n^i - \frac{nk_z}{K_i^2\rho} Z_n^i(K_i\rho)b_n^i\right] S_n, \tag{5.5}$$

$$H_z = \left[Z_n^i(K_i\rho)b_n^i\right] S_n, \tag{5.6}$$

where the super-index i identifies the region of space where the fields are being calculated. Two different areas may be distinguished: $i = C$ corresponding to $\rho < r$ and $i = D$ (inside the cylinder) where $\rho > r$ (outside the cylinder). Inside the cylinder, $Z_n^C(x) = J_n(x)$, i.e. the Bessel function of the 1st kind of order n ensures the fields are finite at the center of the cylinder ($\rho = 0$). For the outer region, $Z_n^D(x) = H_n^{(1)}(x)$, the Hankel function of the 1st kind of order n. This guarantees the proper behaviour at infinity. The primed Bessel functions denote differentiation with respect to the argument $x = K_i\rho$. Although we will limit ourselves to non-magnetic media, the magnetic permeabilities in the two regions μ_C and μ_D have also been included. The remaining variables S_n and K_i where, as before, $i = C$, D denotes the region in space are

$$S_n = \exp\left[jn\varphi + jk_z z - j\omega t\right], \tag{5.7}$$

$$K_i^2 = \omega^2\epsilon_i(\omega) - k_z^2. \tag{5.8}$$

The unknown coefficients a_n^i and b_n^i are obtained by applying the boundary conditions at $\rho = r$. In the case of a plasmonic waveguide, these are: the tangential components of the electric and magnetic field must be continuous across the interface. The resulting system of homogeneous equations is available in [25]. Its non-trivial solution may be obtained by letting the determinant vanish. Finally, the transcendental equation whose solutions are the dispersion relation of the modes supported by such a waveguide is [19]

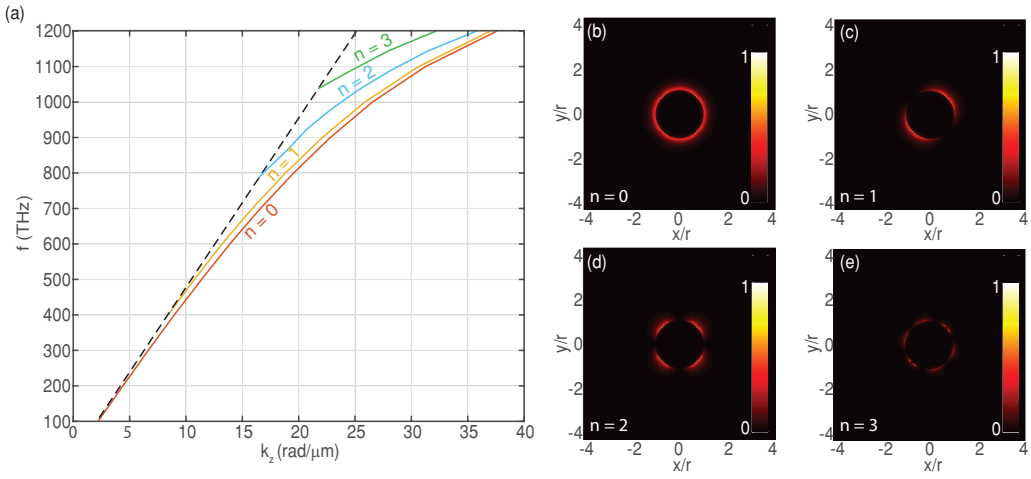

Figure 5.4: (a) Simulated dispersion relation of the lower order modes of a free-standing infinite Ag nano-wire with 160-nm-radius circular cross-section. (b)-(d) Normalized electric field intensity patterns at (b)-(c) 1000 THz and (e) 1200 THz.

$$F(k_z,\omega) = A(k_z,\omega)B(k_z,\omega) + E(k_z,\omega) = 0, \tag{5.9}$$

with

$$A(k_z,\omega) = \frac{\mu_C}{K_C r}\frac{J_n'(K_C r)}{J_n(K_C r)} - \frac{\mu_D}{K_D r}\frac{H_n^{(1)\prime}(K_D r)}{H_n^{(1)}(K_D r)}, \tag{5.10}$$

$$B(k_z,\omega) = \frac{(\omega/c)^2\epsilon_C(\omega)}{\mu_C K_C r}\frac{J_n'(K_C r)}{J_n(K_C r)} - \frac{(\omega/c)^2\epsilon_D(\omega)}{\mu_D K_D r}\frac{H_n^{(1)\prime}(K_D r)}{H_n^{(1)}(K_D r)}, \tag{5.11}$$

$$E(k_z,\omega) = n^2 k_z^2\left[\frac{1}{(K_D r)^2} - \frac{1}{(K_C r)^2}\right]^2. \tag{5.12}$$

In general, the dispersion relation in (5.9) cannot be solved analytically. Nevertheless, its solutions can be numerically approximated via root finding. To illustrate this, a numerical example is studied next. The dispersion relation of the n = 0-3 modes, with n indicating the number of azimuthal (φ) variations, supported by a free-standing ($\epsilon_D = 1$) silver waveguide with radius $r = 160$ nm is depicted in Fig. 5.3. Silver's complex dielectric permittivity $\epsilon_C(\omega)$ is described by (4.1) with $\epsilon_\infty = 1$, $\omega_p = 1.37\times10^{16}$ rad/s and $\Gamma = 40$ THz [26]. The (f, k_z) pairs corresponding to the roots of (5.9) appear as black curves in the figure.

Fig. 5.4(a) shows the dispersion relation simulated using an eigenmode solver [27]. The agreement with the theoretical curves in Fig. 5.3 is excellent. The E-field

intensity pattern of the various modes are shown in Fig. 5.4(b)-5.4(e). Clearly, the $n = 0$ - 3 modes' intensity patterns show a monopole, dipole, quadrupole and hexapole field distribution, respectively. In addition, the intensity distributions in Fig. 5.4(b)-5.4(d) suggest that higher order modes produce less localized E-fields which is in good agreement with the theory –note that for a given frequency (1000 THz in 5.4(b)-5.4(d)), Fig. 5.4(a) shows the real part of k_z decreasing for increasing n, which is associated with weaker localization to the waveguide interface [28].

5.2.2 Cavity modes in nano-rods

Infinite waveguides as those described in the previous section cannot be realised in practice. However, similar modes may arise when finite sections of waveguide, often referred to as nano-wires or nano-rods, are considered.

Fig. 5.5(a) shows the schematic of a nano-rod with radius r and length L terminated in flat ends. The nano-rod is illuminated by a plane-wave propagating at an angle α of its axis. It has been shown that finite nano-rods act as resonators for SPPs [29]. The discontinuities at the nano-rod's edges form a cavity that supports FP resonances which in turn produce standing waves along its length. The extinction cross-section, which is often employed to describe the interaction between nano scale objects and light [5], can be used to analyse this phenomenon. The Finite Integration Technique (FIT) solver of CST Microwave studio has built-in functions that automatically integrate the total power scattered and absorbed by the nano-rod to give the scattering and absorption cross-section, respectively. The simulated extinction cross-section can then be simply obtained via the summation of these two $\sigma = \sigma_s + \sigma_a$, with σ_s and σ_a indicating scattering and absorption cross-section, respectively.

Fig. 5.5(b) shows the simulated σ when a plane-wave with E-field polarised along the axis of a silver nano-rod with $r = 30$ nm and $L = 500$ nm acts as the excitation ($\alpha = 90°$), and when incidence is oblique ($\alpha = 30°$). Note that incident light couples to different order FP modes in each case. Efficient coupling to one mode or another depends on mode matching, which requires not only a good spatial overlap of the intensity profiles, but also matching the phase profiles. The quality of mode matching and in turn, the coupling efficiency, can be evaluated using an overlap

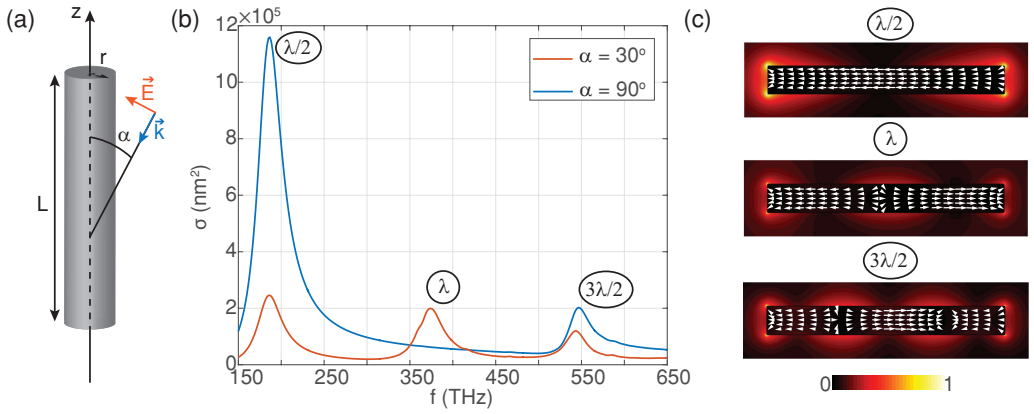

Figure 5.5: (a) Schematic of a finite nano-rod with radius r and length L terminated in flat ends. An incident plane-wave propagates forming an angle α with the axis of the nano-rod. (b) Scattering cross-section when $\alpha = 30°$ and $90°$. (c) E-field distribution (colour map) and current density (white arrows) at the frequencies labelled in (b). (b)-(c) The nano-rod has $r = 30$ nm and $L = 500$ nm.

integral [30]

$$\eta = \frac{|\int E_i^* E_m dS|^2}{\int |E_i|^2 dS \int |E_m|^2 dS}, \tag{5.13}$$

where E_i and E_m are the complex E-field distributions of the incidence and the FP mode, respectively. For $\alpha = 90°$, only the odd order FP cavity resonances ($\lambda/2$ and $3\lambda/2$) are excited. Odd order modes exhibit antisymmetric charge distributions enabling their excitation by such a plane wave. Contrarily, even order FP modes cannot be excited in this configuration due to the overlap integral vanishing. By tilting the E-field ($\alpha = 30°$), the overlap integral becomes non-zero making even order FP modes (λ) accessible. Note that all the above resonances belong to the fundamental radially polarised mode ($n = 0$). Higher order modes are at cut-off for the considered frequency range.

Since the nano-rod edges are not perfect mirrors, SPPs are not reflected exactly at them. As a consequence, the conventional FP resonant condition

$$k_z L = m\pi, \tag{5.14}$$

where k_z represents the wavenumber of the mode and $m = 1, 2, 3, ...$ indexes the FP resonance order, is not perfectly satisfied. Instead, the field penetrates a certain

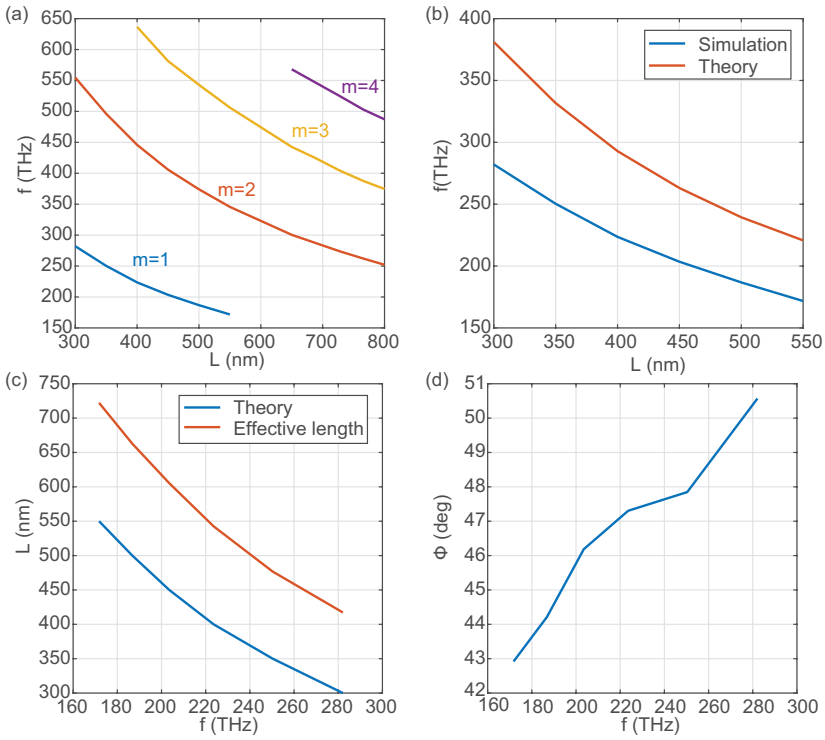

Figure 5.6: (a) First 4 lower order FP cavity resonances of a $r = 30$ nm Ag nanowire with varying L obtained from the cross-section simulated with CST when $\alpha = 30°$. All of them are related to the $n = 0$ mode of the infinite waveguide. (b) Resonant frequency of the $m = 1$ mode. (c) Required length of the nano-rod and (d) extra phase-shift upon reflection at its boundaries so that the $m = 1$ mode resonates at a certain frequency.

distance into the background and (5.14) must be modified to account for this effect. Algebraically, field penetration can be described as an increased effective length $L_{eff} > L$ so that the condition reads [31]

$$k_z L_{eff} = m\pi; \tag{5.15}$$

or considering an extra phase-shift ϕ introduced upon reflection at the edges [29]

$$k_z L + \phi = m\pi. \tag{5.16}$$

The accuracy of (5.14)-(5.16) is investigated in Fig. 5.6. Fig. 5.6(a) shows the resonant frequencies of the $m = 1$ - 4 modes of a nano-rod with $r = 30$ nm and varying L. All of these are associated with the $n = 0$ order mode of the infinite waveguide and have field profiles (not shown) similar to that in Fig. 5.4. The

resonant frequencies were obtained from the position of the various peaks in the simulated cross-section for $\alpha = 30°$. Two typical features of FP resonators can be observed in Fig. 5.6(a). On the one hand, for a given length of the nano-rod, the resonant frequency increases for higher mode order. On the other, the resonant frequency red-shifts as the nano-rod lengthens, being this red-shift linear with L (in terms of wavelength), as corresponds to a mode wavelength of the form $\lambda_m = 2\pi L/m$.

For simplicity, only the lowest order cavity mode ($m = 1$) has been considered in Fig. 5.6(b)-5.6(d). Fig. 5.6(b) shows a comparison between the simulated resonant frequency and that calculated using (5.14) in combination with (5.9). As can be seen, the theoretical results considerably deviate from the simulations. The resonant conditions (5.15) or (5.16) provide increased accuracy, since they account for the effective mode wavelength shortening. Fig. 5.6(c) shows that the effective length of the nano-rod (given by (5.15)) so that it resonates at the frequency indicated by the simulations is considerably larger than its physical length. Similar results may be obtained using (5.16), where instead of an effective length, a non-zero phase-shift is considered. The required phase-shift so that both models are equivalent is shown in Fig. 5.6(d) which significantly deviates from 0°.

5.2.3 Edge plasmons in nano-disks

The most basic configuration in plasmonics consists of a smooth straight metal-dielectric interface. Such an interface supports SPPs propagating along the 2D discontinuity. This type of SPPs is also present when metallic films of finite extent are considered. Finite films additionally support edge modes with reduced dimensionality, i.e. 1D EPs, which are highly confined to their ridges [32]. Recently, it has

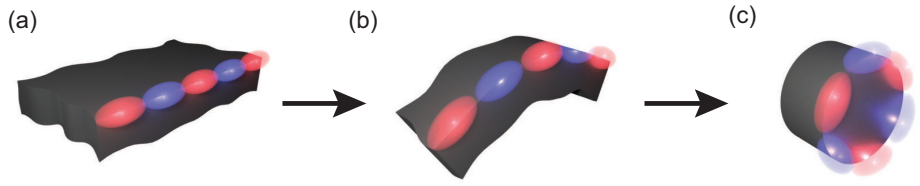

Figure 5.7: Transformation from (a) a straight metallic edge to a (c) nano-disk following a (b) convex bend.

been shown that EPs remain mostly unaltered when curvature is introduced, even for bending radii as small as a few tens of nanometres [4]. Sufficiently bending the film results in the formation of a nano-disk, Fig. 5.7. Hence, nano-disks can also support EPs which may coexist with the cavity modes described in section 5.2.2.

We begin our study by considering a free-standing silver nano-disk of radius $r = 160$ nm and thickness $t = 30$ nm , Fig. 5.8(a). The extinction cross-section σ normalized to the area of the nano-disk $A = \pi r^2$ under plane-wave excitation is depicted in Fig. 5.8(b). There, the results obtained for normal incidence ($\theta = 0°$) are compared with the Transverse Electric (TE) and Transverse Magnetic (TM) off-normal cases ($\theta = 45°$). When $\theta = 0°$, a single maximum arises in the scattering spectra, at ~ 327 THz. Fig. 5.8(c) clearly shows a dipole H_z distribution in that case. The dipole mode of nano-disks has been recently investigated by *Wan et al* [5]. The nano-disks in that study exhibited two hybridized dipoles, one with symmetric charge distribution at the top and bottom interfaces of the nano-disk, as in the case presented in Fig. 5.8(c), and a second mode with antisymmetric distribution and higher resonant frequency. Depending on the geometry (diameter and thickness of the nano-disk), these two modes may be uncoupled and with low spectral overlap as is likely our case –no second peak is observed in Fig. 5.8(b)– or strongly coupled. The former results in a Fano-type resonant profile [33], while the latter may cause super-scattering [5], i.e. scattering cross-section values surpassing the single resonance limit [34], which may be used not only for sensing applications [5], but also to implement strong absorbers for thermal therapy and solar cells [35].

When the angle of incidence deviates from $\theta = 0°$, new resonances, corresponding to higher order multipolar modes, arise in the scattering spectra, Fig. 5.8(b). These multipolar modes are more effectively excited when the incident wave is TE polarised than for TM polarisation. According to Fig. 5.8(d)-5.8(f), which shows H_z when a $\theta = 45°$ TE polarised plane-wave illuminates the nano-disk, these are: the dipole, that remains approximately at the same frequency as in the $\theta = 0°$ case, Fig. 5.8(d), the quadrupole, which is excited at 505 THz, Fig. 5.8(e), and the hexapole, at 653 THz, Fig. 5.8(f). Along the same line, higher order modes are expected at higher frequencies. The excitation of multipolar modes in nano-disks was experimentally verified in [4] using a Scanning Transmission Electron Microscope (STEM). STEM combined with Electron Energy Loss Spectroscopy (EELS)

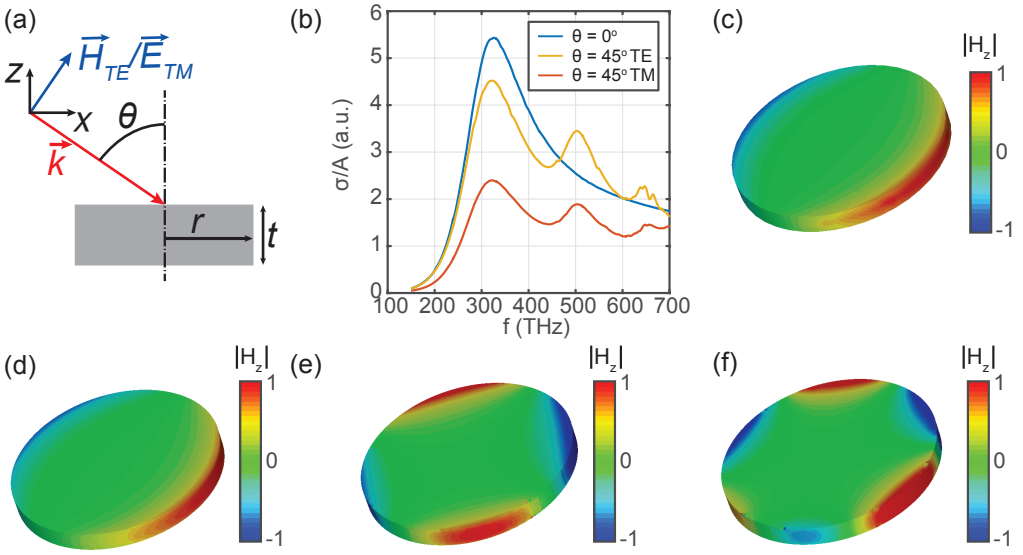

Figure 5.8: (a) Structure under consideration and field polarisation. The blue arrow represents the H-field for TE- and the E-field for TM-polarisation. (b) Normalized scattering cross-section for $\theta = 0°$ and 45° and both possible polarisations. (c)-(f) Normalized H_z volume distribution (c) at normal incidence and for (d)-(f) 45° TE polarisation. The frequencies are (c) 327 THz, (d) 321 THz, (e) 505 THz and (f) 653 THz.

allows very high spatial resolution scanning and has been widely employed for mapping LSPs of nano-particles with a variety of shapes [36, 37]. The measurements presented in [4] enabled extracting the dispersion diagram of the EPs of nano-disks which closely followed that of a straight edge, suggesting that they are the same mode. Comparison with the measured dispersion relation of a semi-infinite metal-dielectric interface, showed additionally that, for a given frequency, EPs had larger propagation constants than traditional SPPs, or equivalently, for a given propagation constant, EPs were excited at lower frequencies. This further supports 1D EPs and 2D SPPs being different and coexisting in nano-disks.

The multipolar EPs patterns in Fig. 5.8(d)-5.8(f) may be explained from a standing wave perspective. Multipolar modes exhibiting a certain number of field antinodes will be supported only if there is constructive interference along the edge, i.e. when an integer number of wavelengths fits the perimeter of the nano-disk. The resonant condition obeys

$$k_p = \frac{p}{r}, \tag{5.17}$$

where k_p is the wave-number of the mode with order $p = 1, 2, \ldots$. To validate this

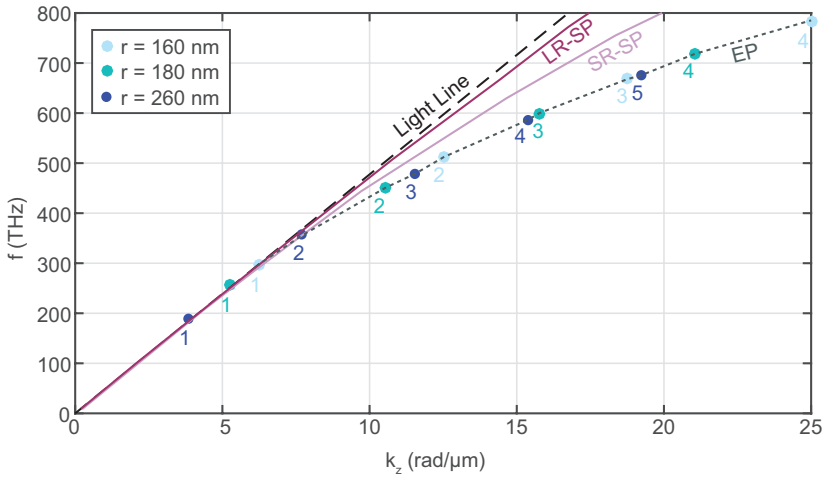

Figure 5.9: Dispersion relation of the EPs of a nano-disk excited at oblique incidence when $t = 35$ nm and r=$160 - 260$ nm and of the SR- and LR- plasmon modes of a $t = 35$ nm free-standing silver film. The light-line is indicated by a black dashed line. Straight grey dotted lines connecting the points at which the EPs resonate have been included as a guide to the eye and the number next to each point labels the corresponding mode order p.

interpretation, the cross-sections of nano-disks with $r = 160 - 260$ nm and $t = 35$ nm were simulated. The wavenumbers can be easily calculated from the spectral position of the various scattering peaks. The dispersion relation computed in this way is shown in Fig. 5.9. For comparison, the theoretical dispersion relation of the two hybridized SPPs of an infinite silver film with the same thickness ($t = 35$ nm) has also been included. These surface modes, often referred as Long Range (LR-) and Short Range (SR-)SPPs, will be discussed in detail in chapter 6. As can be seen in Fig. 5.9, the dispersion relation of the EPs cannot be mapped to those of the SPPs which agrees with the measurements reported in [4].

5.3 Localized surface plasmons in 2D arrays of nano-particles

Although isolated nano-particles are ideal candidates for applications such as increasing the sensitivity of some spectroscopic techniques [38] or to implement nanoscale optical tweezers [39], 2D periodic assemblies offer more degrees of freedom for tai-

loring light interaction. Not only the shape and constituent material of the nano-particles forming the array can be controlled, but also their relative positions and orientations. This broadens the range of exhibited phenomena and, thus, the range of potential applications. These include directional single photon and plasmon sources [40] and light trapping [41], among others.

5.3.1 Edge plasmons supported by arrays of nano-disks

The structure under analysis consists of an array of silver nano-disks arranged forming a 2D square lattice with periodicity $a = 400$ nm, whose unit-cell is depicted in Fig. 5.10. Despite a substrate would be required in practice for mechanical support, the free-standing case is considered here to simplify the analysis. The radius and thickness of the nano-disks are $r = 160$ nm and $t = 30$ nm, respectively. The angular spectral response of the infinite array was simulated using the Frequency Domain (FD) solver of CST Microwave studio with plane-wave illumination, enforcing unit-cell boundary conditions. Fig. 5.11 shows the plane of incidence for TE and TM polarisation. The zeroth order reflectance R, transmittance T and absorption $A = 1 - T - R$ for TE plane-wave incidence are shown in Fig. 5.12(a)-5.12(c), respectively, whilst Fig. 5.12(d)-5.12(f) correspond to the TM case.

The EP modes supported by the array of nano-disks clearly depend on light polarisation, as observed in Fig. 5.12. Excitation via TE polarised waves is mainly mediated by the H-field, since in this case $E_z = 0$, Fig. 5.11. At normal incidence ($\theta = 0°$), only the 3rd order EP mode (hexapole) is excited, causing a reflectance minimum and a maximum in the transmittance and absorption spectra at ~ 640 THz, Fig. 5.12(a)-5.12(c). This may result surprising since for individual nano-disks only the dipole couples to normal incident light (subsection 5.2.3). In section 5.3.1, we will show that light coupling to EP modes in arrays is not only governed by the incident angle and polarisation, but also by the symmetries exhibited by the lattice. Coupling to the hexapole when $\theta = 0°$ is mediated by this lattice effect. When $\theta \neq 0°$, the symmetry breaks and a second mode, which remains dark at normal incidence, can be observed. This is the 2nd order EP (quadrupole) which resonates at ~ 485 THz. The resonant frequencies agree with those obtained in the case of isolated nano-disks (subsection 5.2.3), although slightly red-shifted due to near-

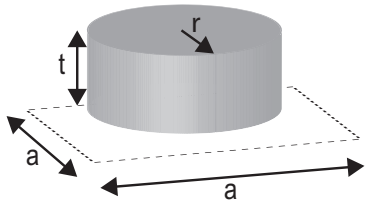

Figure 5.10: Unit-cell detail of a 2D array of nano-disks with radius r and thickness t. The array is formed by arranging the nano-disks in a square lattice with period a.

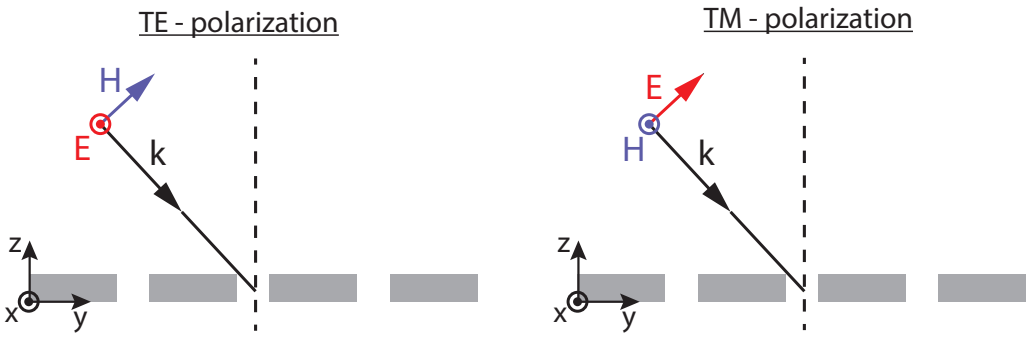

Figure 5.11: Incident plane for TE and TM polarised light.

field interaction between adjacent nano-disks [42]. The normalized magnitude of the E-field through a mid-plane shown in Fig. 5.13 exhibits the expected multipolar patterns and so do the superimposed current densities; namely, from lower to higher resonant frequency: a quadrupole and a hexapole, shown respectively in Fig. 5.13(a) and 5.13(b). On the other hand, TM polarised waves have a non-vanishing E_z component which results in a more complex coupling mechanism, as both the E- and H-fields of the incident light overlap with those of the EPs. Fig. 5.12(d)-5.12(f) show the hexapole also being excited in this case, however the quadrupole remains dark, which further indicates that $H_z \neq 0$ is required for it to become bright in this configuration.

Fig. 5.12 additionally suggests that the resonant frequencies of the EPs depend very weakly on the angle of incidence, further confirming their localized nature. An exception to this occurs when the EP modes and Wood's Anomalies (WAs) [43, 44] spectrally overlap. WA arises when a grating order changes its character from evanescent to propagating at grazing angle, i.e. when the in-plane component of the momentum matches that of light: $|k_{(u,v)}| = |k|$. For a rectangular lattice and free-space propagation, the latter condition may be written as [45]

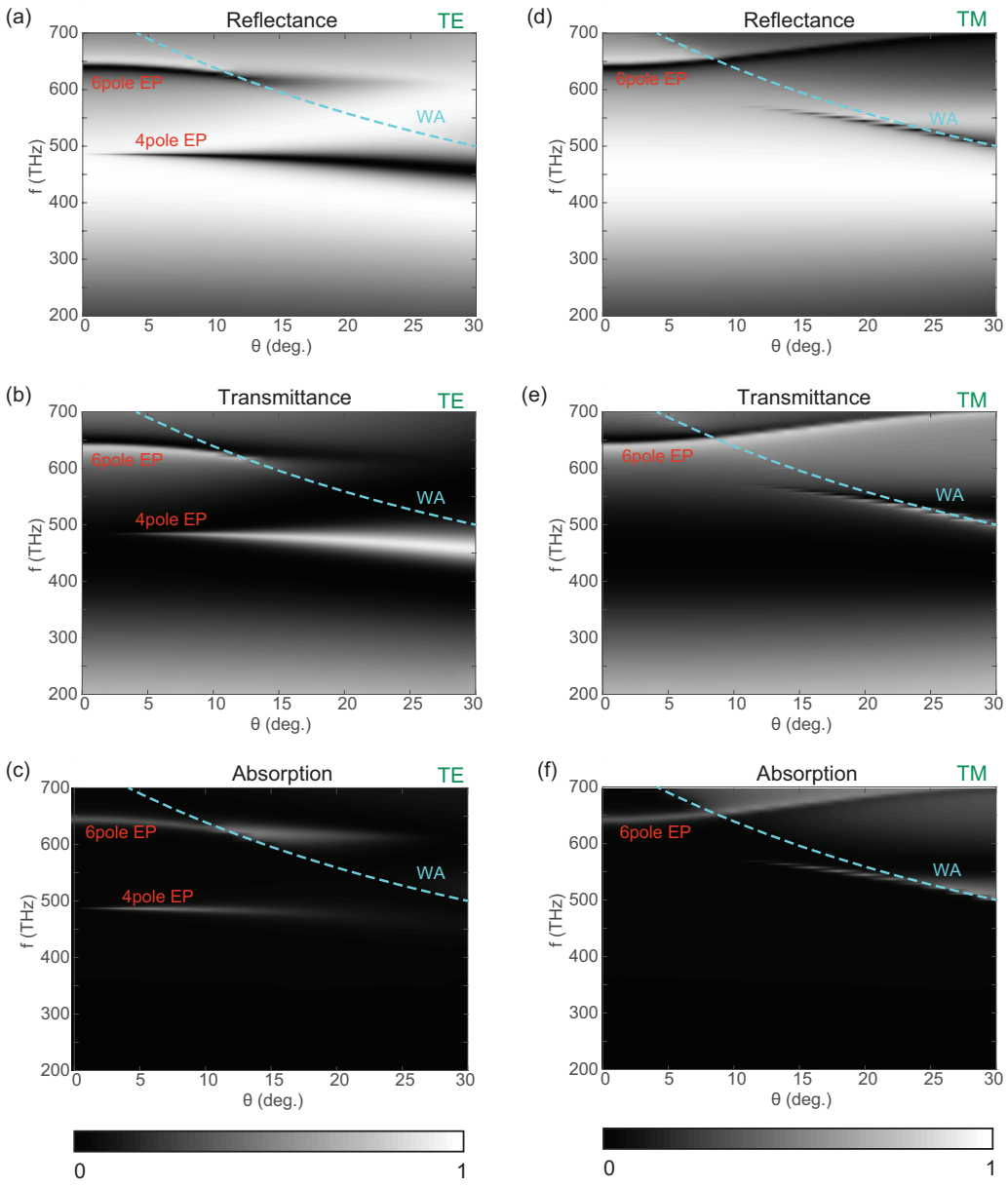

Figure 5.12: Angular spectral response of a nano-disk array with $t = 30$ nm, $r = 160$nm, $a = 400$ nm and varying θ when the incoming wave is (a)-(c) TE and (d)-(f) TM polarised. (a), (d) Transmittance. (b), (e) Reflectance. (c), (f) Absorption. WA is shown as a cyan dashed line while the different order EPs are indicated by the labels.

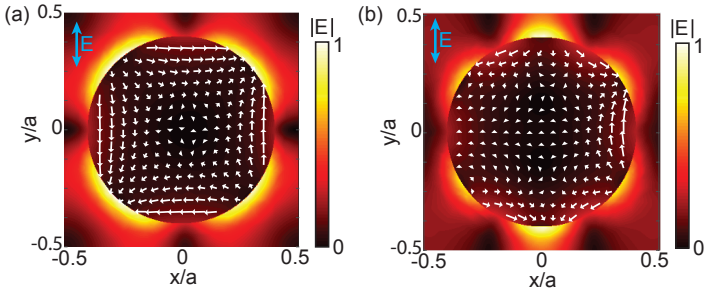

Figure 5.13: E-field distribution normalized to its maximum value at centre plane in the TE-case and a frequency of (a) 485 THz and (b) 640 THz. The vector current distribution is shown with the white arrows.

$$\left(k_x^i + uG_x\right)^2 + \left(k_y^i + vG_y\right)^2 = k_0^2, \tag{5.18}$$

where k_x^i and k_y^i represent the x- and y-components of the incident light momentum, respectively, and (u, v) indexes the grating order. Since in our case the periodicity is equal along the direction of the two lattice vectors $\hat{x}$ and $\hat{y}$, the reciprocal lattice constant is simply given by $G_x = G_y = \frac{2\pi}{a}$. The frequency at which the $(-1, 0)$ grating order becomes propagating (lower frequency WA) is indicated by the cyan curves in Fig. 5.12. As shown in the figure, in the vicinity of WA, there are strong variations in the zeroth order scattering response. This, together with an increased damping due to radiation loss and frequency shifts, is among the effects commonly attributed to WAs [45, 46].

Influence of the lattice symmetries on the spectral response

As previously mentioned, the angular response shown in Fig. 5.12(a)-Fig. 5.12(c) reveals another interesting feature of the structure under study: the 3rd order EP (hexapole) is excited at normal incidence. Despite this may seem to contradict part of the discussion in subsection 5.2.3, in particular the need for off-normal illumination to enable higher order modes to become bright, in the following, it will be shown that this is not the case. There is a fundamental difference between the nano-disks analysed in subsection 5.2.3 and those considered here: the lattice. This suggests that the lattice plays an important role in mediating light coupling to some EPs (e.g. the hexapole) at normal incidence.

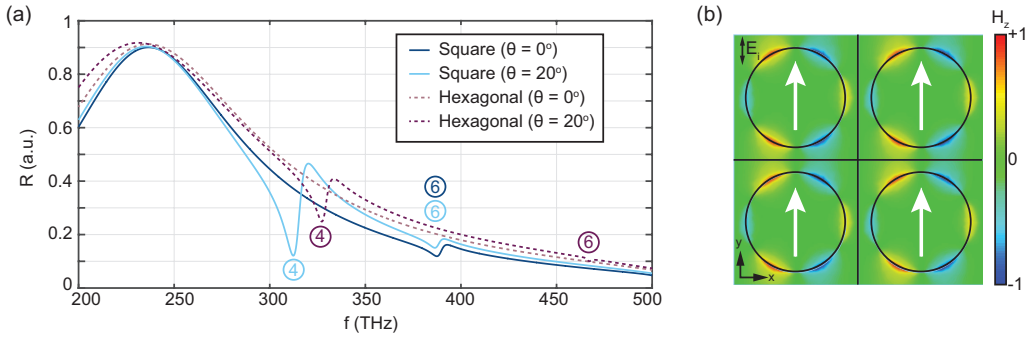

Figure 5.14: (a) Comparison of the simulated reflectance response between hexagonal and square nano-disk arrays when $\theta = 0°$ and 20° TE incidence. The geometrical parameters are $a = 400$ nm , $t = 5$ nm and $r = 160$ nm. The multipoles corresponding to the various reflectance minima are indicated by the labels. (b) H_z distribution at the input interface of the square lattice when illuminated by a 390 THz normal incident TE plane wave. The white arrows indicate the net (electric) dipole moment provided by the lattice configuration.

The effect of the lattice is investigated in Fig. 5.14. Fig. 5.14(a) shows the reflectance response of a nano-disk array arranged in a square (solid lines) and a hexagonal (dashed lines) lattice. Both arrays consist of nano-disks with $r = 160$ nm and $t = 5$ nm and periodicity $a = 400$ nm. Although we are mainly interested in the response to $\theta = 0°$ incident light, the $\theta = 20°$ case has been included for the sake of comparison. Yuxtaposition of this two cases (and same lattice configuration) confirms that off-normal illumination enables coupling to more EPs than normal incidence. In particular, for the square lattice, off-normal light ($H_z \neq 0$) couples to the quadrupole at $\sim$ 390 THz, that remains dark for normal incidence. This indicates that, a non-vanishing H_z component is necessary for exciting the quadrupole in a square lattice. A similar comparison can be performed in the hexagonal lattice case. As can be seen, when the lattice is hexagonal, no EP modes are supported at normal incidence within the frequency range considered. However, when $\theta = 20°$, not only the quadrupole but also the hexapole, which is considerably blue-shifted with respect to the square lattice case, become accessible. Therefore, contrarily to the square lattice case, coupling to the hexapole requires $H_z \neq 0$ in this configuration.

EPs at normal incidence can only occur if a dipole moment is introduced via near-field interaction between neighbouring nano-disks. An example of this is depicted in Fig. 5.14(b), which shows the H_z distribution at the input interface when normal

incident TE light (E-field polarised along y) impinges the square lattice of nano-disks. Fig. 5.14(b) shows the interaction between adjacent nano-disks modifying the hexapole, which exhibits anti-nodes with different field intensities at different locations of their perimeter. This results in the mode acquiring a net dipole moment along y, represented by the white arrows in Fig. 5.14(b). As a consequence, the overlap integral differs from zero and the hexapole becomes accessible to normal incident light.

Fig. 5.14(a) additionally shows that the quadrupole and the hexapole remain dark when $\theta = 0^\circ$ in the case of the square and hexagonal lattice, respectively. This can also be explained based on symmetry considerations. Due to the lattice and the mode field pattern sharing the same symmetries, all neighbouring nano-disks interact in the same way, not producing any net dipole moment. As a result, the overlap integral with a normal incident plane wave vanishes, prohibiting the excitation of these modes. This reasoning can be extended even further: for a square lattice, mutual interactions between even-order EPs (e.g. quadrupole, octupole and so on) cannot introduce a net dipole moment, due to the lattice 4-fold symmetry. On the contrary, interaction between odd-order modes (e.g. hexapole, decapole and so on) is different in vertical than in horizontal, and produces the required net dipole moment to enable their coupling to normal incident light. Similarly, the hexagonal lattice prohibits the excitation of even-order EPs at normal incidence as a result of its double reflection symmetry. Additionally, in this configuration, the hexapole is also inaccessible to normal incident light because it shares the lattice 3-fold symmetry. As a result, the first bright EP available in this case is the decapole. Although this mode is above the frequency range considered and therefore it is not shown in Fig. 5.14, it will be clearly visible in chapter 6.

Thickness dependent edge plasmon hybridization

The thickness of the nano-disks is closely related to EP hybridization. This is investigated in Fig. 5.15(a) and 5.15(b), which show the spectral response of a square lattice of nano-disks with $r = 160$ nm, $a = 400$ nm and $t = 20$ - 200 nm at $\theta = 5^\circ$ incidence. Zeroth order reflectance and absorption are shown in Fig. 5.15(a) and 5.15(b), respectively. Two different set of modes producing reflectance minima

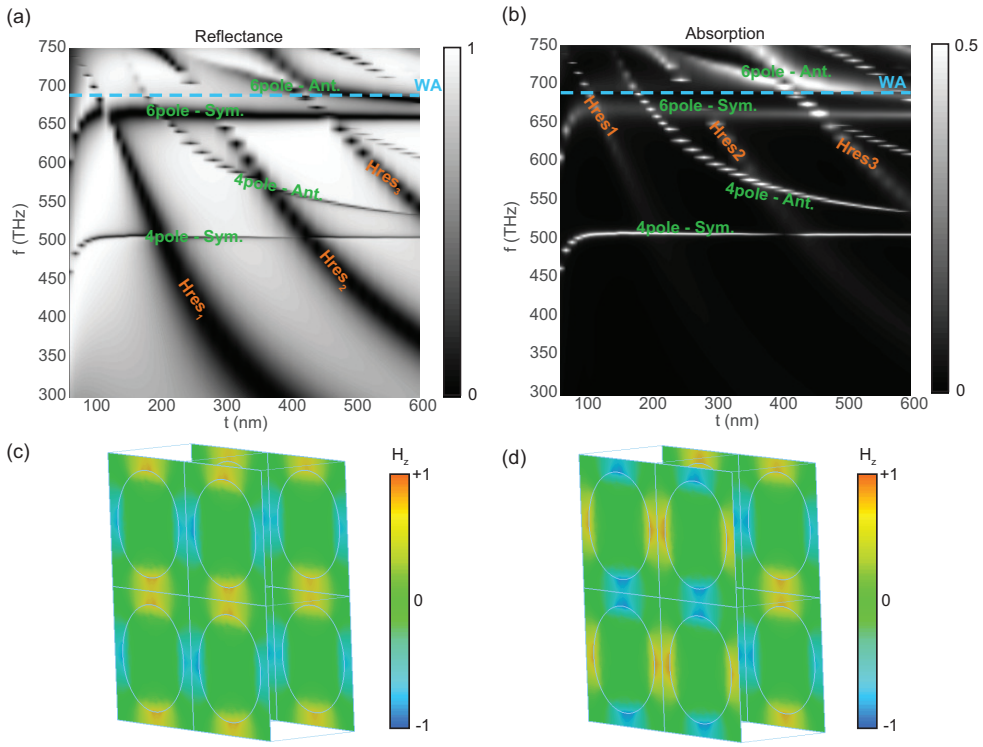

Figure 5.15: (a) Reflectance and (b) absorption response of a square lattice of nano-disks with $a = 400$ nm, $r = 160$ nm and $t = 20$ - 600 nm when $\theta = 5°$. Odd and even EP of different orders are labelled in green, whilst the different order FP magnetic resonances are shown in orange. WA is indicated with cyan dashed lines. (c)-(d) Normalized H_z distribution for $t = 300$ nm at the input and output interfaces. The frequencies are (b) 507 THz, (c) and (d) 586 THz.

can be distinguished in Fig. 5.15(a). One of these sets correspond to EP (green labels) whilst the second set (orange labels) belongs to a different category which shall be studied in detail in section 5.3.2. Since EPs exhibit larger absorption values, they are easier to appreciate in the absorption spectra, Fig. 5.15(b). Two EPs (the quadrupole and the hexapole) are supported within the considered frequency range. Analysing the effect of the thickness on these modes simplifies by considering a single EP since interference effects, which increase with frequency due to the higher number of resonances supported, are minimized. In the following and without loss of generality, we focus only on the quadrupole. The influence of the thickness on this mode, allows identifying two different regimes: thin ($t < 200$ nm) and thick nano-disks ($t \geq 200$ nm). For thin nano-disks, light couples to a unique quadrupole. As the thickness increases above 350 nm, a second quadrupole, resonating at a

higher frequency, can be observed. The resonant frequencies of the two quadrupoles approach for increasing t. These are ultimately expected to overlap, in analogy to the results reported by *Wan et al.* in isolated nano-disks [5].

The H_z distributions shown in Fig. 5.15(c) and 5.15(d) further confirm the mode hybridization model. There, the field distributions of the symmetric and antisymmetric modes supported by a $t = 300$ nm nano-disk array have been depicted at 507 THz and 586 THz, respectively. As can be seen in Fig. 5.15(c) and Fig. 5.15(d), H_z exhibits quadrupole patterns at the input and output interfaces, which are in phase at 507 THz and out of phase at 586 THz.

Effect of the shape of the nano-particles

EPs are not exclusive of nano-disks, they are supported by a variety of different shaped nano-particles, e.g. nano-patches as those studied in chapter 4. Fig. 5.16(a) shows the absorption spectrum of a square array of nano-disks together with that obtained for a nano-patch array. In both cases, $t = 30$ nm and $a = 400$ nm. The lateral side of the nano-patches is $l = 250$ nm so that the perimeter is approximately equal to that of the nano-disks. A TE polarised plane-wave propagating at $\theta = 5°$ is considered. Both absorption responses exhibit a single narrow peak, 5.16(a). Fig. 5.16(b) and Fig. 5.16(c) show the H_z distribution at resonance when nano-disks and nano-patches are considered, respectively. Quadrupoles are clearly formed in

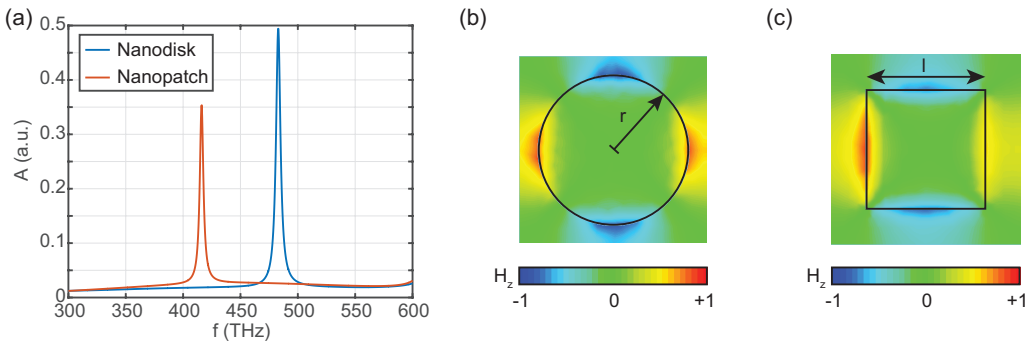

Figure 5.16: (a) Absorption of an array consisting of 160 nm radius nano-disk and 250 nm lateral side nano-patches. In both cases $t = 30$ nm and $a = 400$ nm. The array is excited by $\theta = 5°$ TE light. (b)-(c) H_z distribution at the input interface and frequency (b) 483 THz in the case of the nano-disk array, and (c) 416 THz in the nano-patch array case.

both cases. The main difference being a frequency shift which can be attributed in part to the different near-field interaction between neighbouring elements. Note likewise that the EP resonant condition given in Eq. (5.17) does not account for any effects as a result of near-field coupling, being in turn inaccurate for arrays.

The above results allow us to associate the LSP observed in the TE angular response of the PRS presented in chapter 4 (section 4.2) with the quadrupole EP supported by the nano-patches.

5.3.2 Fabry-Pérot modes in nano-disks and nano-rings

In addition to EPs, the spectra depicted in Fig. 5.15 show a second set of modes (labelled as Hres_x, where x indicates the mode order) with a distinctive response to t variations. These usually produce lower absorption values, and thus are easier to observe in the reflectance response depicted in Fig. 5.15(a). As will be shown, the Hres_x modes are just plasmonic FP modes of the nano-disks.

The Hres_x modes are weakly influenced by the angle of incidence of the incoming light, as suggested by Fig. 5.15 and Fig. 5.17 which show $\theta = 5°$ and $\theta = 0°$ reflectance, respectively. Since less EPs are excited in the $\theta = 0°$ case, their interference with the Hres_x is minimized compared to $\theta = 5°$, facilitating the analysis. Hence, hereafter, we will focus on the normal incidence case.

Fig. 5.17(a) shows that contrarily to EPs which were only significantly influenced by t in the thin film region, the resonant frequencies of the Hres_x modes strongly depend on the thickness of the nano-disks. A similar effect was presented in section 5.2.2 in the case of isolated nano-disks.

The FP nature of the Hres_x modes is further confirmed in Fig. 5.17(b)-5.17(e). Fig. 5.17(b) shows reflectance for varying t at 400 THz. Three minima, corresponding to the excitation of the 1st, 2nd and 3rd order resonances (t = 250, 560 and 850 nm, respectively), can be observed. The normalized E-field distributions in Fig. 5.17(c)-5.17(e) exhibit typical FP patterns, i.e. for higher t, the number of field anti-nodes along the axis $\hat{z}$ of the nano-disks increases.

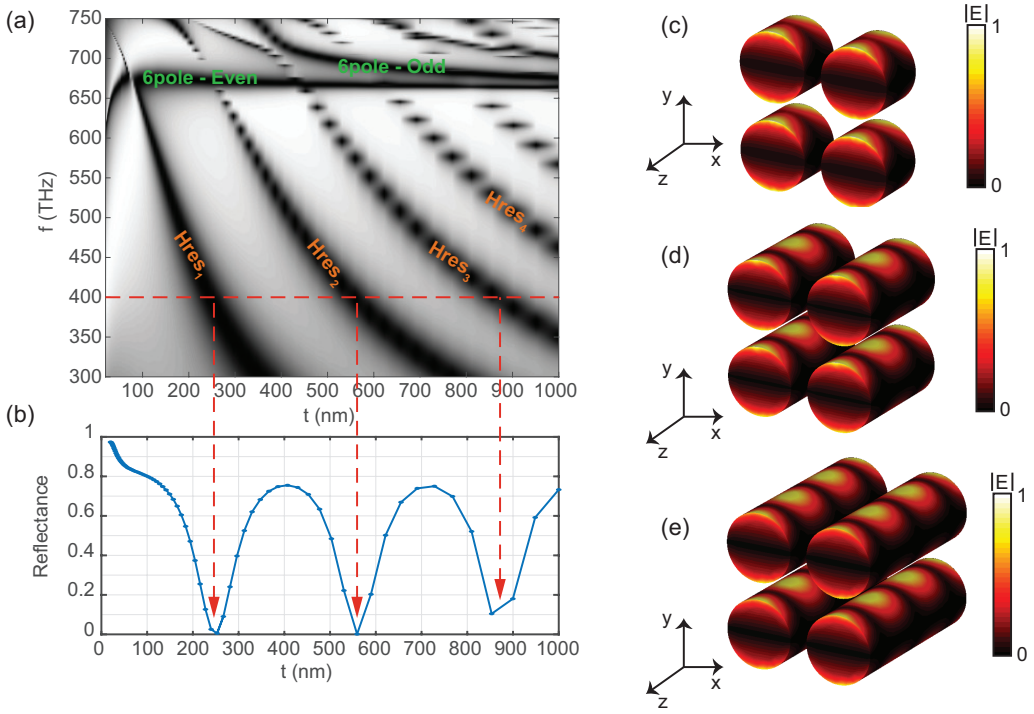

Figure 5.17: (a) Reflectance response of an array of nano-disks with $a = 400$ nm, $r = 160$ nm and $t = 20 - 1000$ nm for $\theta = 0°$ and with E-field polarised along $\hat{y}$. Odd and even EP are labelled in green whilst different order FP magnetic resonances are shown in orange. (b) Reflectance versus t at 400 THz. (c)-(e) Normalized E-field distribution when (c) $t = 250$ nm, (d) $t = 560$ nm and (e) $t = 850$ nm.

Electric enhancement in nano-ring arrays

Norlander et al. showed that individual nano-particles LSPRs hybridize when two of them are located in close proximity, forming a dimer [47]. The resulting dimer exhibits two modes with different resonant frequencies, referred to as the coupled-bonding and coupled-antibonding modes, which inherit part of the properties of the individual LSPs. In absence of interference with EPs, the spectral response of the arrays investigated here is dominated by the coupled-bonding mode. Interestingly, for very small gap separations, nano-ring dimers have been shown to exhibit very high E-field concentration to the sub-wavelength gap region [48]. Moreover, the resulting electric hot-spots are much stronger than those observed in individual nano-rings [13].

An array of gold nano-rings with outer radius $R_{\text{out}} = 300$ nm, inner radius $R_{\text{in}} = 200$ nm and thickness $t = 100$ nm is considered next. The nano-rings are distributed on

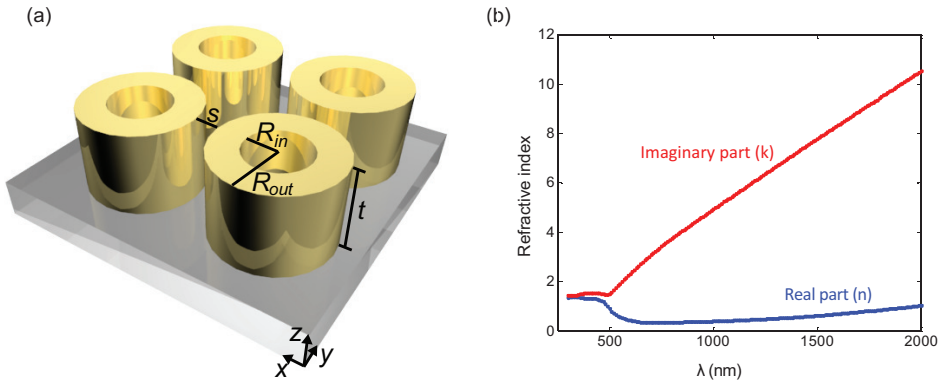

Figure 5.18: (a) Array of gold nano-rings with inner radius R_{in}, outer radius R_{out}, thickness t and separation between rings s. The nano-rings are placed on top of a dielectric substrate with refractive index n. (b) Measured refractive index n and extinction coefficient k of gold.

top of a quartz substrate, forming a square lattice with spacing $s = p - 2R_{\text{out}} = 30$ nm, Fig. 5.18(a). In the simulations, the index of refraction of gold was fitted to the experimental values depicted in Fig. 5.18(b). These were obtained via ellipsometry. The index of refraction of quartz was approximated by the following Sellmeier equation [49]

$$n^2 - 1 = \frac{0.6961663\lambda^2}{\lambda^2 - 0.0684043^2} + \frac{0.4079426\lambda^2}{\lambda^2 - 0.1162414^2} + \frac{0.8974794\lambda^2}{\lambda^2 - 9.896161^2}, \tag{5.19}$$

with λ in micrometres. Eq. (5.19) fits experimental data between 0.21 μm and 3.71 μm, covering most of the Near Infrared (NIR) region of the spectrum.

Fig. 5.19(a) shows the simulated absorption spectrum. The absorption maximum at 920 nm corresponds to the excitation of the coupled-bonded mode. Such a mode causes charges of different signs to concentrate at opposite sides of the nano-rings, resulting in the creation of an electric dipole moment [13]. As a consequence, for small s, the E-field is strongly enhanced in the region between adjacent nano-rings, as depicted in Fig. 5.19(b) and 5.19(c) which show the E-field enhancement intensity evaluated at a xy-plane located at $t/2$ distance from the substrate, and at a xz-plane passing through the centre of the nano-rings, respectively. In the previous, the intensity enhancement was calculated as the ratio of power with and without nano-rings $I_E = |E|^2/|E_0|^2$, with $\vec{E} = E\hat{x}$ and $\vec{E}_0 = E_0\hat{x}$, respectively.

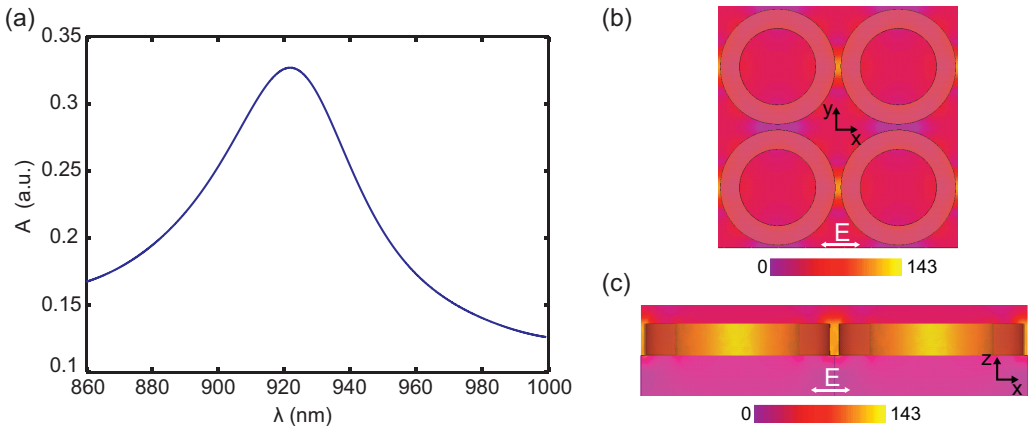

Figure 5.19: (a) Simulated extinction coefficient of the array of gold nano-rings with $t = 100$ nm, $R_{\text{out}} = 300$ nm, $R_{\text{in}} = 200$ nm and $s = 30$ nm. A quartz substrate is considered. (b)-(c) I_E at 920 nm at the two main central cut-planes, namely (b) xy-plane and (c) xz-plane. The polarisation of the incident field is indicated in white.

Virtual current loops: a route towards magnetic enhancement

Most of the studies available in the literature focus on the electric enhancement provided by relatively thin gold nano-rings, mainly due to their simpler fabrication [50]. Nonetheless, thicker nano-rings produce a very interesting scenario where the region between them closely resembles a pair of coupled parallel nano-plates. It has been shown that the LSPRs supported by such nano-plates can exhibit Virtual Current Loops (VCLs) [51]. Such VCLs produce local H-fields that may sum up to that of the incident wave, resulting in magnetic activity [15–18]. As a consequence, this type of LSPRs are commonly referred to as magnetic plasmons [52]. In addition to nano-rings, other structures such as self-assembled nanoparticle clusters [53] and fishnet metamaterials [54], also support VCLs-based magnetic plasmons. Interestingly, VCLs are not only capable of producing magnetic enhancement but also of confining the local H-field to sub-wavelength regions, creating magnetic hot-spots [18, 55].

The underlying mechanism is investigated in Fig. 5.20 which shows the currents at resonance when the array is illuminated at normal incidence. As can be seen, the coupled-bonded mode supported by the nano-ring array produces charges of different signs at the surfaces of adjacent nano-rings. Excitation by the incoming wave, promotes charge motion which results in opposite currents flowing along $\hat{z}$.

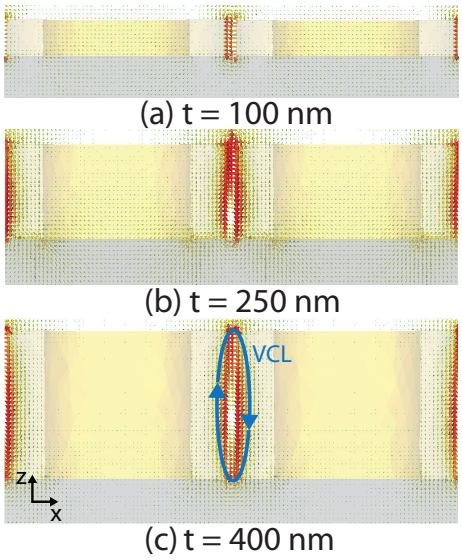

Figure 5.20: Currents generated in a pair of coupled nano-rings for different values of the metal thickness. A VCL (over-imposed in (c) for clarity) is formed in the gap under normal illumination, being responsible for the strong enhancement of the magnetic field in the gap as well as for the creation of a magnetic dipole. Parameters: $R_{\text{out}} = 300$ nm, $R_{\text{in}} = 200$ nm and $s = 30$ nm.

Three different cases are included in the figure: thin, medium and thick nano-rings. In the case of thin nano-rings depicted in Fig. 5.20(a), the currents generated at each side of the gap only flow along very small distances, so they merely produce an accumulation of opposite charges. This results in the formation of an electric dipole that causes E-field enhancement in the gap region, as in the case shown in Fig. 5.19. As t increases, the paths the currents flow along lengthen, Fig. 5.20(b). For thick enough nano-rings, the distance covered becomes sufficient for a VCL to form, Fig. 5.20(c). The resulting VCL behaves as a magnetic dipole and as such, strong local H-fields (y-directed) may originate in the gap region.

Similarly to the E-field case, the H-field enhancement can be evaluated through its intensity $I_M = |H|^2/|H_0|^2$, where H and H_0 stand for the y-component of the H-field, with and without nano-rings, respectively. The E- and H-field enhancement evaluated at the central point (height $t/2$ over the substrate and equidistant to the nano-rings) are studied in Fig. 5.21. Note that in all the cases presented hereafter, the enhancement is monitored at the resonant frequency, i.e. when the absorption spectrum reaches its maximum. Fig. 5.21(a) shows I_E and I_M for $t = 125$ - 425 nm

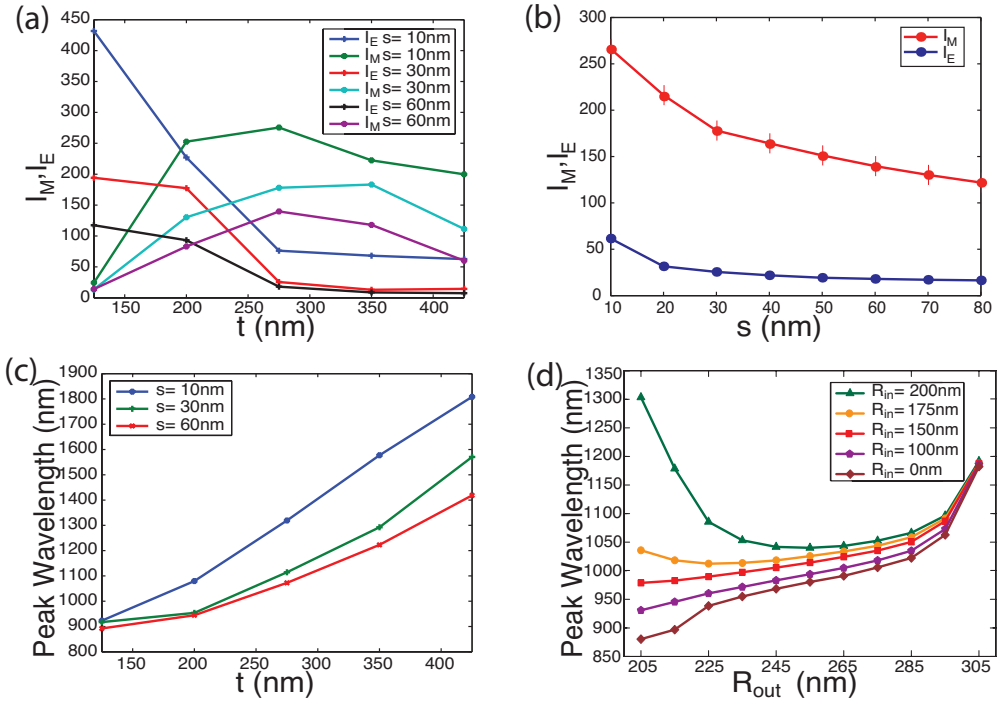

Figure 5.21: (a) I_E and I_M values obtained from numerical simulations as a function of the nano-ring thickness for different nano-rings spacings. The array is illuminated normally at a wavelength at which the extinction reaches a maximum. (b) I_E and I_M as a function of the spacing for a fixed thickness $t = 275$ nm. (c) Resonant wavelength as a function of the metal thickness for the three previously considered separation distances between nano-rings. Constant parameters: $R_{\text{out}} = 300$ nm and $R_{\text{in}} = 200$ nm. (d) Resonant wavelength as a function of the outer radius for different values of the inner radius and a fixed thickness $t = 275$ nm. The separation distance for each value of R_{out} is chosen so that the period is fixed to 630 nm.

and $s = 10$, 30 and 60 nm. In the case of thin nano-rings, our results show highly enhanced E-fields at the centre of the gap. Contrarily, the H-field is comparable to the case with no nano-rings, i.e. no enhancement is obtained with this configuration. When $t > 150$ nm, I_M increases whilst I_E decreases. This suggests that for sufficiently thick nano-rings, whilst the E-field weakens, a high H-field enhancement is achieved producing a magnetic hot-spot in the gap region. For instance, for $t > 250$ nm the magnetic enhancement is more intense than the electric one ($I_M > I_E$). This suggests that the LSPR changes its character from electric to magnetic for sufficiently thick nano-rings, i.e. for thin nano-rings the LSPR resembles a pure electric dipole whilst for sufficiently thick nano-rings a magnetic dipole is formed [J7].

The influence of the spacing s is analysed in Fig. 5.21(b). Similarly to I_E, I_M increases for shorter s which indicates that the magnetic resonance is a result of strong coupling between adjacent nano-rings. We expect that the H-field enhancement will be ultimately limited by mechanisms such as the intrinsic non-locality of the dielectric response of the metal [56] or quantum-tunnelling [57] similarly to the E-field enhancement.

The results shown in Fig. 5.21(a) suggest that there is an optimum metal thickness that maximizes I_M, e.g. $I_M = 178$ for $s = 30$ nm and $I_M = 140$ for $s = 60$ nm. This can be explained by analysing the effect that varying t has on the formation of the VCL, Fig. 5.20. For very thin nano-rings, there is no current flow. As a consequence, the H-field is not enhanced and, at resonance, the response is purely electric. As t increases, the induced currents flow through increasingly longer distances. The resulting VCLs produce in turn enhanced magnetic fields. For a certain thickness, a quasi-symmetric –the substrate cannot be neglected– VCL is formed causing maximum I_M at the central point. The same can be concluded by considering a pair of nano-rings as a section of a plasmonic waveguide consisting of two metallic hollow nano-cylinders. The discontinuities introduced by free-space and the substrate behave as low-reflectivity mirrors forming a t-high cavity. Analogously to Eq. (5.14)-(5.16), the resonant condition of such a cavity strongly depends on t, Fig. 5.21(c). There, it can be seen that the resonance red-shifts for increasing t provided that it is in the magnetic regime, i.e. $t > 150$ nm. Contrarily, if $t < 150$ nm (electric regime), the resonant wavelength remains approximately constant and no standing wave is formed. Similar dual behaviour has been previously observed in other plasmonic nano-structures [18, 58].

From nano-rings to nano-disks

The influence of the hole in the magnetic response is studied in Fig. 5.21(d), which shows the resonant wavelength for varying R_{out} and different R_{in} values. The resonant wavelength is mainly controlled by R_{out}, which allows tuning the resonance over the whole NIR range. When $R_{\text{out}} = 305$ nm and $s = 20$ nm, the influence of R_{in} is nearly negligible, due to the field being strongly confined to the gap region and thus, nearly not affected by the inner hole. In this case, the response of nano-disks

($R_{\text{in}} = 0$) and nano-rings arrays is equivalent. For smaller R_{out}, the nano-rings become decoupled and the resonance behaves similar to that of an isolated nano-ring, i.e. as an electric dipole. This can be better appreciated in the curve corresponding to $R_{\text{in}} = 200$ nm (shown in green). In that case, increasing R_{out} causes a strong red-shift of the resonant wavelength as reported by *Aizpurua et al.* [13] for the individual nano-ring case.

Fabrication and measurements

The nano-ring arrays were fabricated in the *Paul Scherrer Institute* using electron beam lithography. Three samples of nano-ring arrays with $t = 220$, 350 and 420 nm were fabricated. Each sample contained 200×200 μm^2 arrays with $R_{\text{out}} = 300$ nm, $R_{\text{in}} = 200$ nm and $s = 30$ and 60 nm (nominal values). Scanning Electron Microscopy (SEM) images of the fabricated arrays can be found in Fig. 5.22. The thickness of the fabricated nano-rings estimated from the tilted SEM images in Fig. 5.22(b) and Fig. 5.22(d) was very close to the nominal value. However, significant differences were found in the remaining dimensions. For instance, the measured spacing was half the nominal one in some of the samples.

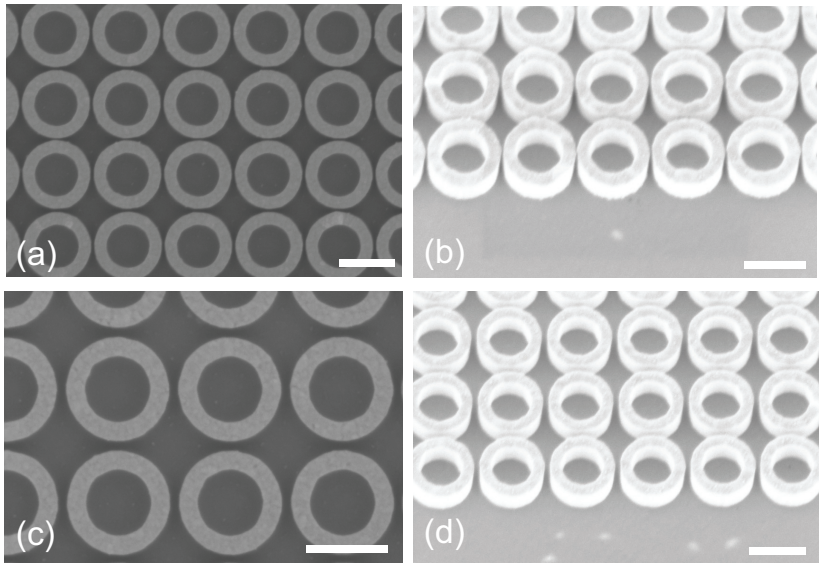

Figure 5.22: SEM images of the fabricated samples. The nominal dimensions are $t = 350$ nm, $R_{\text{out}} = 300$ nm and $R_{\text{in}} = 200$ nm. (a), (c) $s = 30$ nm, (b), (d) $s = 60$ nm. Images (a) and (b) are taken from the top whilst (c) and (d) are tilted 25°. Scale bars correspond to 500 nm.

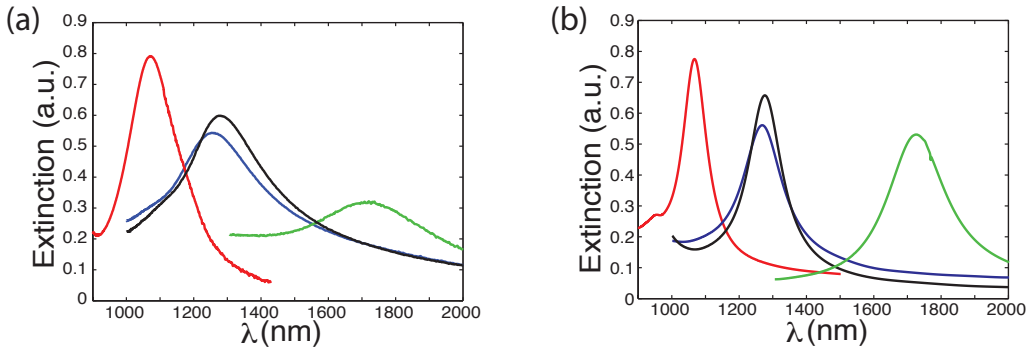

Figure 5.23: Measured (a) and simulated (b) extinction spectra of arrays of gold nano-rings on quartz with. Red curve: $t = 220$ nm, $R_{out} = 305$ nm, $R_{in} = 195$ nm and $s = 20$ nm; Blue curve: $t = 350$ nm, $R_{out} = 285$ nm, $R_{in} = 190$ nm and $s = 30$ nm; Black curve: $t = 350$ nm, $R_{out} = 310$ nm, $R_{in} = 210$ nm and $s = 50$ nm; Green curve: $t = 420$ nm, $R_{out} = 330$ nm, $R_{in} = 190$ nm and $s = 15$ nm.

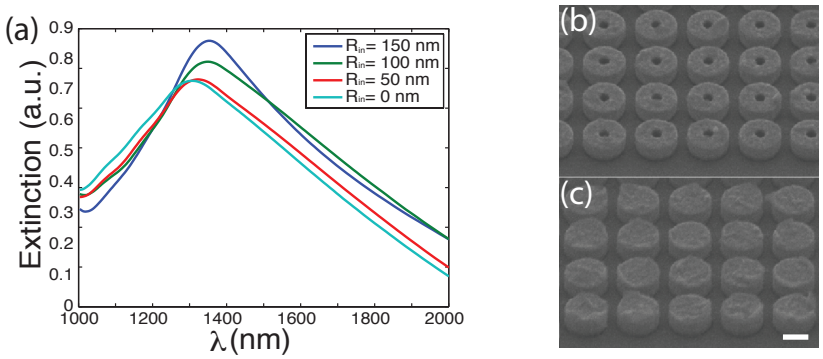

Figure 5.24: (a) Measured extinction spectra of different nano-ring arrays as a function of the inner radius R_{in} with $t = 175$ nm, $R_{\text{out}} = 325$ nm and $s = 120$ nm (nominal values). Scanning electron microscope images of fabricated samples with (b) $R_{\text{in}} = 50$ nm and (c) $R_{\text{in}} = 0$ nm. The scale bar is 400 nm.

The measurements were performed at *Valencia Nanophotonics Technology Center*. A Bruker Vertex 80 Fourier-Transform Interferometer (FTIR) spectroscopy system was used to experimentally measure the absorption spectra of the samples, Fig. 5.23(a). For the sake of comparison, the simulated absorption responses are depicted in Fig. 5.23(b). The measured resonances are broader than the simulated ones. This is attributed to multiple nano-rings with slightly different dimensions resonating at marginally different frequencies. Likewise, the two samples with equal thickness (blue and black curves) approximately resonate at the same wavelength, as suggested by Fig. 5.21(c). Our measurements confirm that the magnetic resonance

strongly red-shifts for increasing t [18]. This distinctive feature can be exploited for discriminating between electric and magnetic resonances.

A second set of samples with vaying $R_{\text{in}} = 0$ - 150 nm was likewise fabricated. The measured results are summarized in Fig. 5.24(a). SEM images of the samples can be seen in Fig. 5.24(b)-5.24(c). The measured spectra clearly exhibit a slight red-shift of the resonance for increasing R_{in}. This suggests that R_{in} can be used to fine tune the resonant wavelength, in addition to the coarse tuning provided by R_{out}.

5.4 Conclusions

Understanding the interaction between optical radiation and nano-particles is crucial for the advancement of nanophotonics and its application to imaging [16], cloaking [59], [60], sensing [61] and, more importantly, nano-antennas [60]. Plasmonic modes not being considered by traditional antenna design guidelines may result in unwanted effects that degrade the performance of the designed nano-antennas. In order to avoid or at least mitigate these, it is essential to fully understand their causes, effects and relation to the geometry. The results presented in this chapter aim to expand our understanding of LSPs supported by 2D arrangements of nano-particles, motivated by the abnormal response of the PRS of the Leaky-Wave (LW) antenna designed in chapter 5. To this end, we initially considered an infinite waveguide with circular cross-section (section 5.2.1). The waveguiding problem had to be revisited to accommodate effects derived from the metal's complex permittivity when plasmonic materials were employed. In section 5.2.2, we showed that nano-rods act as resonators for SPPs, supporting FP cavity resonances associated with the waveguide modes. However, the condition for constructive interference has to be adequately modified to account for the effective lengthening of the nano-rods, a typical situation encountered in nano-antennas [31, 62]. In section 5.2.3, we considered the case in which the waveguide is sufficiently short for these modes to be purely evanescent, i.e. a nano-disk. In this scenario, EPs highly confined to the nano-disk ridges, become predominant. Experimental results recently reported in [4], indicate that nano-disks' EPs can be exactly mapped to the modes of a straight edge and were accurately described from a standing wave perspective, which is in excellent agreement with our simulations. Our results showed that light coupling to EPs strongly depends on

the symmetries of the problem. For instance, only the 1st order EP couples to a normal incident plane-wave. Higher order EPs remain dark. On the contrary, off-normal illumination may enable their excitation, thanks to the symmetry breaking introduced by phase retardation. Therefore, no additional bright mode is required for their coupling to free-space light, compared to other localized modes appearing in similar structures [33, 35].

The case in which the nano-disks were not isolated but arranged forming 2D arrays (section 5.3) was considered next. Such an assembly benefits from additional degrees of freedom for tailoring light interaction (e.g. filling-factor, lattice symmetries and periodicity), broadening the range of potential applications [40, 41]. The EPs supported by the array of nano-disks were analysed in section 5.3.1 [J6, C4]. These showed a strong dependence on the lattice symmetries, which may serve to enable/disable certain modes. This feature may be exploited for realising novel à la carte optical polarisers and filters with low frequency dispersion. Similarly to the couple-bonding mode of nano-disk dimers, arrays can also exhibit FP LSPs confined to the gap between sufficiently close neighbouring elements. A thorough analysis of these modes, including both simulations and experimental measurements, can be found in section 5.3.2 [J7]. There, we showed that arrays of thick nano-rings are capable of converting incoming light into highly localized magnetic hot-spots with over 250 intensity enhancement. Such an array constitutes a very dense array of magnetic nano-antennas, each one formed by two closely spaced nano-rings whose performance resembles that of a loop antenna [63] with perimeter $p = 2(t + s)$ although, in our case, the resonant wavelength is about 1.5 - 2 times higher than expected from traditional antenna design ($\sim p$). This effective loop lengthening can be attributed to field penetration into the metals and the dielectric substrate [31,62]. The proposed structure constitutes a new building block to achieve magnetism in the optical domain [64]. Compared to previously reported magnetic antennas, such as horizontal parallel nano-plates, our structure does not require any dielectric spacing [55] making the region of magnetic field localization easily accessible which makes it suitable for sensing [8, 23, 24] or trapping [41], among other applications. Moreover, it enables probing the magnetic near-field in the gap region using appropriate techniques [65].

References

[1] A. Alù, G. D'Aguanno, N. Mattiucci, and M. J. Bloemer, "Plasmonic Brewster Angle: Broadband Extraordinary Transmission through Optical Gratings," *Phys. Rev. Lett.*, vol. 106, no. 12, p. 123902, Mar. 2011.

[2] K. Q. Le, C. Argyropoulos, N. Mattiucci, G. D'Aguanno, M. J. Bloemer, and A. Alù, "Broadband Brewster transmission through 2D metallic gratings," *J. Appl. Phys.*, vol. 112, no. 9, p. 094317, 2012.

[3] C. Argyropoulos, G. D'Aguanno, N. Mattiucci, N. Akozbek, M. J. Bloemer, and A. Alù, "Matching and funneling light at the plasmonic Brewster angle," *Phys. Rev. B*, vol. 85, no. 2, p. 024304, Jan. 2012.

[4] F.-P. Schmidt, H. Ditlbacher, U. Hohenester, A. Hohenau, F. Hofer, and J. R. Krenn, "Universal dispersion of surface plasmons in flat nanostructures," *Nat. Commun.*, vol. 5, p. 3604, 2014.

[5] W. Wan, W. Zheng, Y. Chen, and Z. Liu, "From fano-like interference to superscattering with a single metallic nanodisk," *Nanoscale*, vol. 6, pp. 9093–9102, 2014.

[6] H. Raether, *Surface Plasmons on Smooth and Rough Surfaces and on Gratings*. Springer, 1988.

[7] N. Fang, H. Lee, C. Sun, and X. Zhang, "Sub–diffraction-limited optical imaging with a silver superlens," *Science*, vol. 308, no. 5721, pp. 534–537, 2005.

[8] P. Zijlstra, P. M. Paulo, and M. Orrit, "Optical detection of single non-absorbing molecules using the surface plasmon resonance of a gold nanorod," *Nature nanotechnology*, vol. 7, no. 6, pp. 379–382, 2012.

[9] A. Alù and N. Engheta, "Achieving transparency with plasmonic and metamaterial coatings," *Phys. Rev. E*, vol. 72, p. 016623, Jul 2005.

[10] S. A. Maier, *Plasmonics: Fundamentals and applications*. Springer, 2007.

[11] M.-K. Kim, H. Sim, S. J. Yoon, S.-H. Gong, C. W. Ahn, Y.-H. Cho, and Y.-H. Lee, "Squeezing photons into a point-like space," *Nano Lett.*, vol. 15, no. 6, pp. 4102–4107, 2015.

[12] J. B. Khurgin, "How to deal with the loss in plasmonics and metamaterials," *Nat. Nanotechnol.*, vol. 10, no. 1, pp. 2–6, 2015.

[13] J. Aizpurua, P. Hanarp, D. Sutherland, M. Käll, G. Bryant, and F. García de Abajo, "Optical Properties of Gold Nanorings," *Phys. Rev. Lett.*, vol. 90, no. 5, p. 057401, Feb. 2003.

[14] S. Zou and G. C. Schatz, "Silver nanoparticle array structures that produce giant enhancements in electromagnetic fields," *Chem. Phys. Lett.*, vol. 403, no. 13, pp. 62 – 67, 2005.

[15] R. Ortuño, C. García-Meca, F. Rodríguez-Fortuño, J. Martí, and A. Martínez, "Role of surface plasmon polaritons on optical transmission through double layer metallic hole arrays," *Phys. Rev. B*, vol. 79, no. 7, p. 75425, 2009.

[16] Z. Huang, J. Xue, Y. Hou, J. Chu, and D. Zhang, "Optical magnetic response from parallel plate metamaterials," *Phys. Rev. B*, vol. 74, no. 19, pp. 1–4, Nov. 2006.

[17] W. Cai, U. K. Chettiar, H.-K. Yuan, V. C. de Silva, A. V. Kildishev, V. P. Drachev, and V. M. Shalaev, "Metamagnetics with rainbow colors," *Opt. Express*, vol. 15, no. 6, pp. 3333–3341, Mar 2007.

[18] T. Feng, Y. Zhou, D. Liu, and J. Li, "Controlling magnetic dipole transition with magnetic plasmonic structures," *Opt. Lett.*, vol. 36, no. 12, pp. 2369–2371, Jun 2011.

[19] C. A. Pfeiffer, E. N. Economou, and K. L. Ngai, "Surface polaritons in a circularly cylindrical interface: Surface plasmons," *Phys. Rev. B*, vol. 10, pp. 3038–3051, Oct 1974.

[20] U. Leonhardt, "Optical metamaterials: Invisibility cup," *Nat. Photon.*, vol. 1, no. 4, pp. 207–208, 2007.

[21] H. A. Atwater and A. Polman, "Plasmonics for improved photovoltaic devices," *Nat. Mater.*, vol. 9, no. 3, pp. 205–213, 2010.

[22] M. Kauranen and A. V. Zayats, "Nonlinear plasmonics," *Nat. Photon.*, vol. 6, no. 11, pp. 737–748, 2012.

[23] J. N. Anker, W. P. Hall, O. Lyandres, N. C. Shah, J. Zhao, and R. P. Van Duyne, "Biosensing with plasmonic nanosensors," *Nat. Mater.*, vol. 7, no. 6, pp. 442–453, 2008.

[24] K. M. Mayer and J. H. Hafner, "Localized surface plasmon resonance sensors," *Chem. Rev.*, vol. 111, no. 6, pp. 3828–3857, 2011.

[25] J. A. Stratton, *Electromagnetic Theory.* McGraw-Hill, New York, 1941.

[26] P. Johnson and R. Christy, "Optical constants of the noble metals," *Phys. Rev. B*, vol. 6, p. 4370, 1972.

[27] "Lumerical Solutions, Inc." [Online]. Available: http://www.lumerical.com/tcad-products/mode/

[28] S. Sun, H.-T. Chen, W.-J. Zheng, and G.-Y. Guo, "Dispersion relation, propagation length and mode conversion of surface plasmon polaritons in silver double-nanowire systems," *Opt. Express*, vol. 21, no. 12, pp. 14 591–14 605, Jun 2013.

[29] E. Cubukcu and F. Capasso, "Optical nanorod antennas as dispersive one-dimensional Fabry-Pérot resonators for surface plasmons," *Appl. Phys. Lett.*, vol. 95, no. 20, 2009.

[30] R. Paschotta, "Article on mode matching," in *Encyclopedia of Laser Physics and Technology, 1st ed.* Wiley-VCH, 2008.

[31] L. Novotny, "Effective wavelength scaling for optical antennas," *Phys. Rev. Lett.*, vol. 98, p. 266802, Jun 2007.

[32] P. Berini, "Plasmon-polariton waves guided by thin lossy metal films of finite width: Bound modes of symmetric structures," *Phys. Rev. B*, vol. 61, pp. 10 484–10 503, Apr 2000.

[33] B. Gallinet and O. J. F. Martin, "Influence of electromagnetic interactions on the line shape of plasmonic fano resonances," *ACS Nano*, vol. 5, no. 11, pp. 8999–9008, 2011.

[34] Z. Ruan and S. Fan, "Superscattering of light from subwavelength nanostructures," *Phys. Rev. Lett.*, vol. 105, p. 013901, Jun 2010.

[35] R. Taubert, M. Hentschel, J. K´astel, and H. Giessen, "Classical analog of electromagnetically induced absorption in plasmonics," *Nano Lett.*, vol. 12, no. 3, pp. 1367–1371, 2012.

[36] J. Nelayah, M. Kociak, O. Stephan, F. J. Garcia de Abajo, M. Tence, L. Henrard, D. Taverna, I. Pastoriza-Santos, L. M. Liz-Marzan, and C. Colliex, "Mapping surface plasmons on a single metallic nanoparticle," *Nat. Phys.*, vol. 3, no. 5, pp. 348–353, 2007.

[37] O. Nicoletti, F. de la Peña, R. K. Leary, D. J. Holland, C. Ducati, and P. A. Midgley, "Three-dimensional imaging of localized surface plasmon resonances of metal nanoparticles," *Nature*, vol. 502, no. 7469, pp. 80–84, 2013.

[38] J. F. Li, Y. F. Huang, Y. Ding, Z. L. Yang, S. B. Li, X. S. Zhou, F. R. Fan, W. Zhang, Z. Y. Zhou, W. Yin, B. Ren, Z. L. Wang, and Z. Q. Tian, "Shell-isolated nanoparticle-enhanced raman spectroscopy," *Nature*, vol. 464, no. 7287, pp. 392–395, 2010.

[39] K. Wang, E. Schonbrun, P. Steinvurzel, and K. B. Crozier, "Trapping and rotating nanoparticles using a plasmonic nano-tweezer with an integrated heat sink," *Nat. Commun.*, vol. 2, p. 469, 2011.

[40] A. F. Koenderink, "Plasmon nanoparticle array waveguides for single photon and single plasmon sources," *Nano Lett.*, vol. 9, no. 12, pp. 4228–4233, 2009.

[41] S. Mokkapati, F. J. Beck, A. Polman, and K. R. Catchpole, "Designing periodic arrays of metal nanoparticles for light-trapping applications in solar cells," *Appl. Phys. Lett.*, vol. 95, no. 5, 2009.

[42] W. Rechberger, A. Hohenau, A. Leitner, J. Krenn, B. Lamprecht, and F. Aussenegg, "Optical properties of two interacting gold nanoparticles," *Opt. Commun.*, vol. 220, no. 13, pp. 137 – 141, 2003.

[43] R. Wood, "XLII. On a remarkable case of uneven distribution of light in a diffraction grating spectrum," *Philos. Mag.*, vol. 4, no. 21, pp. 396–402, 1902.

[44] R. W. Wood, "Anomalous diffraction gratings," *Phys. Rev.*, vol. 48, pp. 928–936, Dec 1935.

[45] M. Meier, A. Wokaun, and P. F. Liao, "Enhanced fields on rough surfaces: dipolar interactions among particles of sizes exceeding the Rayleigh limit," *J. Opt. Soc. Am. B*, vol. 2, no. 6, pp. 931–949, 1985.

[46] F. J. Rodríguez-Fortuño, C. García-Meca, R. Ortuño, J. Martí, and A. Martínez, "Modeling high-order plasmon resonances of a u-shaped nanowire used to build a negative-index metamaterial," *Phys. Rev. B*, vol. 79, p. 075103, 2009.

[47] P. Nordlander, , C. Oubre, E. Prodan, K. Li, , and M. I. Stockman, "Plasmon hybridization in nanoparticle dimers," *Nano Lett.*, vol. 4, no. 5, pp. 899–903, 2004.

[48] C.-Y. Tsai, J.-W. Lin, C.-Y. Wu, P.-T. Lin, T.-W. Lu, and P.-T. Lee, "Plasmonic Coupling in Gold Nanoring Dimers: Observation of Coupled Bonding Mode." *Nano Lett.*, vol. 12, no. 3, pp. 1648–1654, Feb. 2012.

[49] I. H. Malitson, "Interspecimen comparison of the refractive index of fused silica," *J. Opt. Soc. Am.*, vol. 55, no. 10, pp. 1205–1209, 1965.

[50] R. Near, C. Tabor, J. Duan, R. Pachter, and M. El-Sayed, "Pronounced Effects of Anisotropy on Plasmonic Properties of Nanorings Fabricated by Electron Beam Lithography." *Nano Lett.*, vol. 12, no. 4, pp. 2158–64, Mar. 2012.

[51] D. Li, L. Qin, D.-X. Qi, F. Gao, R.-W. Peng, J. Zou, Q.-J. Wang, and M. Wang, "Tunable electric and magnetic resonances in multilayered metal/dielectric nanoplates at optical frequencies," *J. Phys. D: Appl. Phys.*, vol. 43, p. 345102, Sep. 2010.

[52] A. Sarychev, G. Shvets, and V. Shalaev, "Magnetic plasmon resonance," *Phys. Rev. E*, vol. 73, no. 3, pp. 1–10, Mar. 2006.

[53] J. Fan, C. Wu, K. Bao, J. Bao, R. Bardhan, N. Halas, V. Manoharan, P. Nordlander, G. Shvets, and F. Capasso, "Self-assembled plasmonic nanoparticle clusters," *Science*, vol. 328, no. 5982, pp. 1135–1138, 2010.

[54] C. García-Meca, J. Hurtado, J. Martí, A. Martínez, W. Dickson, and A. Zayats, "Low-loss multilayered metamaterial exhibiting a negative index of refraction at visible wavelengths," *Phys. Rev. Lett.*, vol. 106, no. 6, p. 67402, 2011.

[55] T. Pakizeh, M. S. Abrishamian, and N. Granpayeh, "Magnetic-field enhancement in gold nanosandwiches," *Opt. Express*, vol. 14, no. 18, pp. 8240–8246, 2006.

[56] C. Ciraci, R. T. Hill, J. J. Mock, Y. Urzhumov, A. I. Fernandez-Dominguez, S. A. Maier, J. B. Pendry, A. Chilkoti, and D. R. Smith, "Probing the Ultimate Limits of Plasmonic Enhancement," *Science*, vol. 337, no. 6098, pp. 1072–1074, Aug. 2012.

[57] K. J. Savage, M. M. Hawkeye, R. Esteban, A. G. Borisov, J. Aizpurua, and J. J. Baumberg, "Revealing the quantum regime in tunnelling plasmonics," *Nature*, vol. 491, no. 7425, pp. 574–577, 2012.

[58] A. Alù and N. Engheta, "The quest for magnetic plasmons at optical frequencies." *Opt. Express*, vol. 17, no. 7, pp. 5723–5730, 2009.

[59] T. Ergin, N. Stenger, P. Brenner, J. B. Pendry, and M. Wegener, "Three-dimensional invisibility cloak at optical wavelengths," *Science*, vol. 328, pp. 337–339, 2010.

[60] E. R. Encina and E. A. Coronado, "Plasmonic nanoantennas: Angular scattering properties of multipole resonances in noble metal nanorods," *J. Phys. Chem. C*, vol. 112, no. 26, pp. 9586–9594, 2008.

[61] S. M. Marinakos, S. Chen, , and A. Chilkoti, "Plasmonic detection of a model analyte in serum by a gold nanorod sensor," *Anal. Chem.*, vol. 79, no. 14, pp. 5278–5283, 2007.

[62] P. Mühlschlegel, H. J. Eisler, O. Martin, B. Hecht, and D. Pohl, "Resonant optical antennas," *Science*, vol. 308, no. 5728, p. 1607, 2005.

[63] C. A. Balanis, *Antenna Theory, 3rd ed.* John Wiley and Sons: Hoboken, NJ, 2005.

[64] F. Shafiei, F. Monticone, K. Q. Le, X.-X. Liu, T. Hartseld, A. Alù, and X. Li, "A subwavelength plasmonic metamolecule exhibiting magnetic-based optical fano resonance," *Nat. Nanotechnol.*, vol. 8, pp. 95–99, Feb. 2013.

[65] M. Burresi, D. van Oosten, T. Kampfrath, H. Schoenmaker, R. Heideman, A. Leinse, and L. Kuipers, "Probing the magnetic field of light at optical fre-

quencies." *Science*, vol. 326, no. 5952, pp. 550–553, 2009.

The most exciting phrase to hear in science, the one that heralds new discoveries, is not "Eureka!" but "That's funny..."

Isaac Asimov

6

Surface plasmons in hole-arrays

6.1 Introduction

The study presented in the previous chapter encompassed Localised Surface Plasmons (LSPs) including Edge Plasmons (EPs), cavity modes and Fabry-Pérot (FP) resonances. Here, the scope of the investigation is extended to analyse the scattering properties of 2D hole-arrays. This study will put forward the close relation between these and the arrays of nano-particles considered in chapter 5, often allowing to associate the modes excited in both configurations. In addition to LSPs, the presence of sub-wavelength apertures in metallic plates is suited for the excitation of propagating surface plasmons. These modes can be exploited in a wide range of applications in nanophotonics and plasmonics [1–3]. Among these applications, Extraordinary Optical Transmission (EOT), which produces transmission levels greatly exceeding those predicted from classical Bethe's theory [4], has attracted special interest since it was first observed [5]. There are several competing theories about the origins

of EOT. While some authors attribute it to coupling between propagating Surface Plasmon Polaritons (SPPs) via Bragg scattering, others point at coupling of the incident light to cavity resonances as being ultimately responsible [6]. Moreover, whether SPPs contribute to enhance or, contrarily, suppress light transmission has also been discussed [7]. We can firmly say that light transmission through hole arrays is with no doubt a complex phenomenon involving coupled effects. Throughout this chapter we aim to bring light to the role of LSPs and propagating SPPs by considering them individually.

To accomplish this, the chapter is structured in two main parts, depending on the level of localization of the modes investigated. The first part (section 6.2) focuses on LSPs. Initially, only an isolated nano-hole drilled in a metallic film (section 6.2.1) is considered [J8]. Our results indicate that nano-holes support EPs circling around their edges, resembling whispering galleries. Such EPs are closely related to those of nano-disks (chapter 5). Their differences and similarities are highlighted in section 6.2.1. Subsequently, a 2D periodic array of nano-holes is examined (section 6.2.2) [J8] with the aim of gaining a better insight into the EOT phenomenon. The effect that the geometrical features of the array play on the behaviour of EPs is likewise investigated, as well as its potential application in sensing.

The second part of the chapter (section 6.3) focuses on propagating SPPs. We initially introduce SPPs propagating across the planar interface formed between two semi-infinite media, being one of them plasmonic. The derivation of the dispersion relation in this case is well known and has been included for comparison. In section 6.3.1, the case of a finite thin metallic film is considered. The dispersion relation in this case is substantially different and must be solved numerically. Nonetheless, by considering the Long Range (LR-) and Short Range (SR-)SPPs separately and with the appropriate approximations, accurate analytical solutions are derived. An approximate closed-form expression for the LR-SPPs can be found in [8]. In this thesis, we extend this work by reporting a simple and accurate analytical solution to the dispersion relation of the SR-SPPs [J9], aiming to speed-up and simplify the design of SR-based applications [9–13]. Our solution will allow, for instance, to calculate the resonant frequencies at which light couples to SR-SPPs. In section 6.3.2, we successfully applied it to predict the resonant frequencies of an array of sub-wavelength holes. Full-wave simulations validate our approach. Lastly, conclusions

are summarized in section 6.4.

6.2 Edge plasmon whispering gallery modes

Whispering Gallery Modes (WGMs) are standing waves formed when a propagating mode loops around a cavity, typically with circular or spherical shape, due to continuous total internal reflection [14]. Optical WGMs have been widely used across the whole electromagnetic spectrum [15–17] and can be found in a wide range of applications, from on-chip photonic filters and biosensors to ultra-low-threshold lasers [18]. SPPs are a special type of electromagnetic wave confined to the surface of conductors and, as such, can also appear in the form of WGMs [19, 20]. EPs may exhibit an analogous behaviour.

A detailed study of the EPs supported by nano-disks was presented in section 5.2.3 and 5.3.1. As discussed, *Schmidt et al* experimentally showed that nano-disk's EPs were related to the EPs of a straight edge [21], Fig. 5.7. However, it has so far been overlooked that bending the edge may lead to a complementary scenario: the creation of a nano-hole, Fig. 6.1; suggesting that nano-disks and nano-holes can be understood as particular cases of convex and concave bends, respectively. Previous experimental evidence of the similarities in the optical response of nano-disks and nano-holes can be found in [22, 23]. According to Babinet's principle, transmission and reflection, electric and magnetic fields, as well as the two polarisation directions exchange their roles in such complementary structures [24] which are thus closely related. EP-WGMs circling along the ridges of nano-holes may be expected, owing to the results presented in the previous chapter. The observation of a dipole mode localised to the edge of an isolated nano-hole by *Degiron et al* [25] as well as later

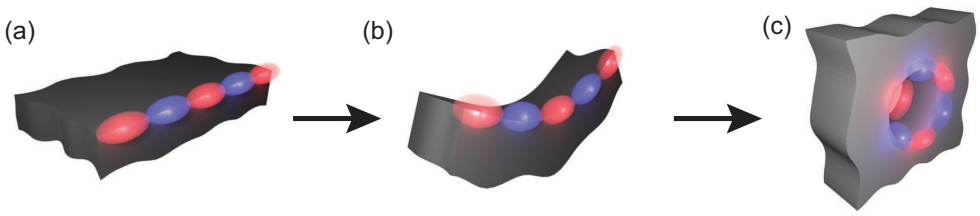

Figure 6.1: Transformation from (a) a straight metallic edge to a (c) nano-hole following a (b) concave bend.

related studies [23, 26] support this idea. Such a mode corresponds to the lower order EP-WGM of the nano-hole, as will be shown next.

6.2.1 Individual nano-holes

Without loss of generality, a nano-hole with radius $r = 160$ nm drilled into a free-standing silver film with thickness $t = 30$ nm and infinite extent is initially considered, Fig. 6.2. Its optical response is studied via Finite-Difference Time-Difference (FDTD) simulations using Lumerical [27], which allows frequency dispersive materials intersecting the boundaries of the simulation domain. A Total-Field Scattered-Field (TFSF) source acts as the excitation. Such a source emits plane waves whilst enabling the automatic separation of the scattered field from the total field. From this, obtaining the scattering cross-section σ_s is straightforward.

Fig. 6.3(a) shows σ_s normalized to the surface $S = 2\pi r(t+r)$ of the nano-hole when illuminated by a Transverse Magnetic (TM) polarised plane wave, which strongly resembles the nano-disk's response in Fig. 5.8(b). The main difference is that the scattering peaks are weaker and broader in the nano-hole case due to the shorter lifetime (increased damping) of the resonances [22, 23]. This effect is not predicted by Babinet's principle which assumes the complimentary structures are made of infinitely thin Perfect Electric Conductor (PEC) sheets [28] contrarily to ours. For $\theta = 0°$, a single maximum arises at 340 THz. Fig. 6.4(a) illustrates the corresponding magnitude scattered magnetic field distribution H_s at the film input interface, with $H_s = H_w - H_{w/o}$, H_w and $H_{w/o}$ being the total magnetic field with and without hole, respectively. The field is concentrated at the edges of the hole and exhibits

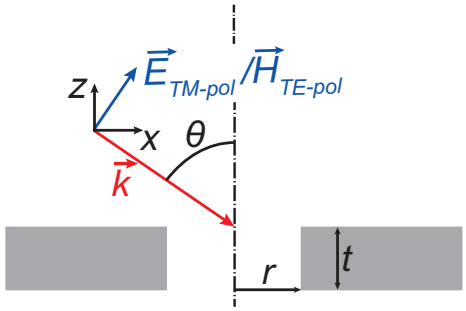

Figure 6.2: Structure under consideration and field polarisation. The blue arrow represents the E-field for TM polarisation and the H-field for TE polarisation.

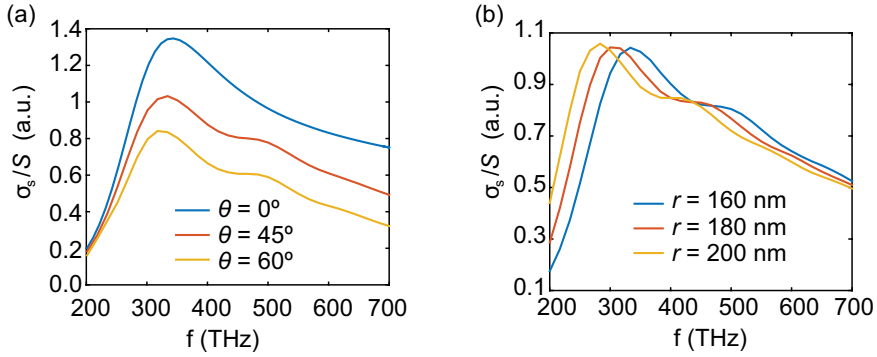

Figure 6.3: Normalized scattering cross-section for the $t = 30$ nm case when (a) $r = 160$ nm and $\theta = 0°$ - $60°$; (b) $\theta = 45°$and $r = 160$ - 200 nm.

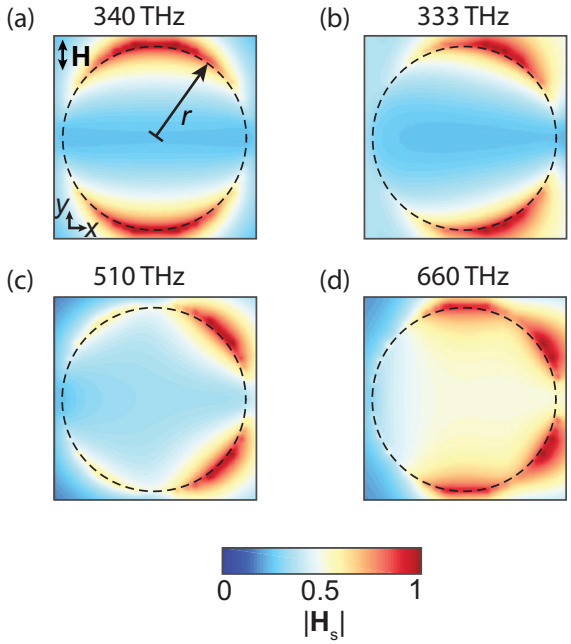

Figure 6.4: H_s at the input interface at the indicated resonant frequencies. The angle of incidence is: (a) $\theta = 0°$ and (b)-(d) $\theta = 45°$.

a dipole distribution. In analogy to the nano-disk case, as the angle of incidence increases, new resonances arise in the spectrum, Fig. 6.3(a) which correspond to higher order multipoles, Fig. 6.4(b)-6.4(d). The dipole resonates at approximately the same frequency as in the $\theta = 0°$ case (Fig. 6.4(b)). A second and a considerably weaker third maxima arise at 510 THz and 660 THz as a result of the excitation of a quadrupole and a hexapole, Fig. 6.4(c) and 6.4(d). Along the same line, higher order modes are expected at higher frequencies. These results suggest that these resonances correspond to different orders of an EP-WGM. The observed asymmetry in the field profiles can be attributed to the oblique illumination.

The wavelength λ_m of the m-th order EP-WGM is related to the perimeter of the nano-hole by $\lambda_m = 2\pi r/m$, where m is an integer number. To verify this property, a parametric study of the nano-hole response when $\theta = 45°$ and varying r is presented in Fig. 6.3(b). As can be seen, the various scattering peaks red-shift for increasing r. Despite the higher order resonances are broader in frequency due to higher losses, the condition for constructive interference along the hole perimeter is satisfied.

6.2.2 2D hole arrays

Nano-holes are often found forming arrays, e.g. for EOT- and metamaterials-based applications [29–31]. Hence, the analysis of EP-WGMs in this scenario is particularly interesting.

A 2D square lattice of nano-holes with period $a = 400$ nm is considered next.

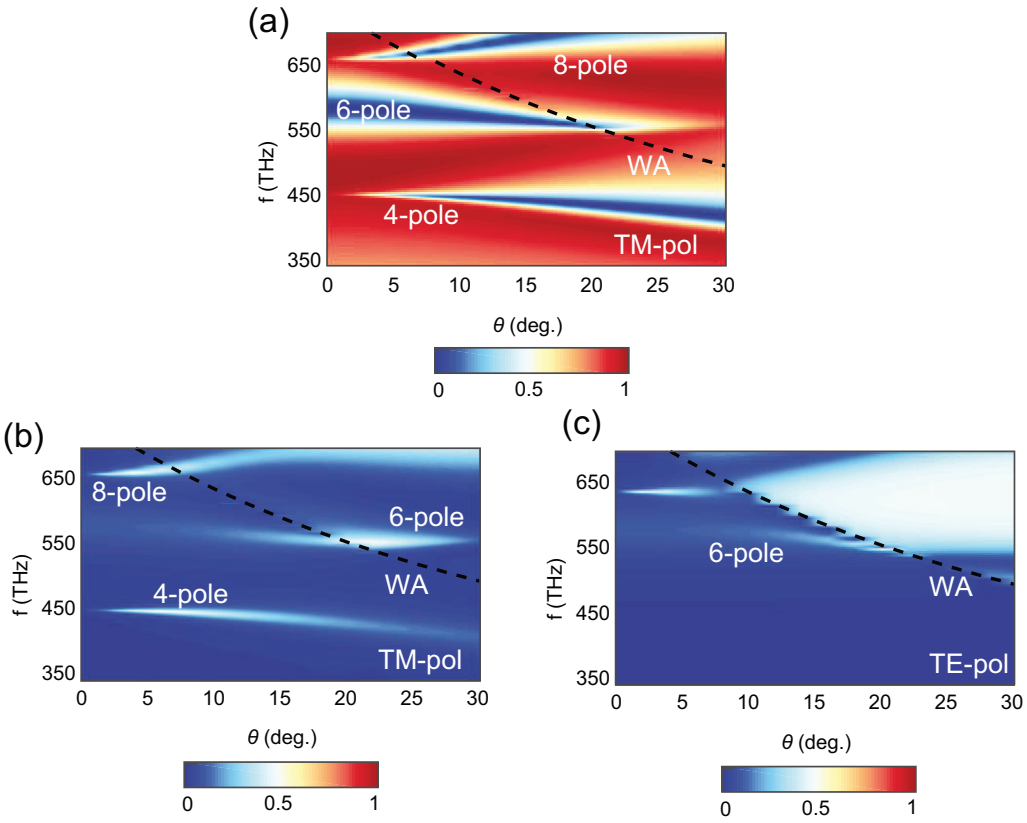

Figure 6.5: Optical response of a periodic hole array with a = 400 nm. (a) TM polarisation transmittance, (b) TM polarisation absorption, and (c) TE polarisation absorption. WA is indicated with dashed lines.

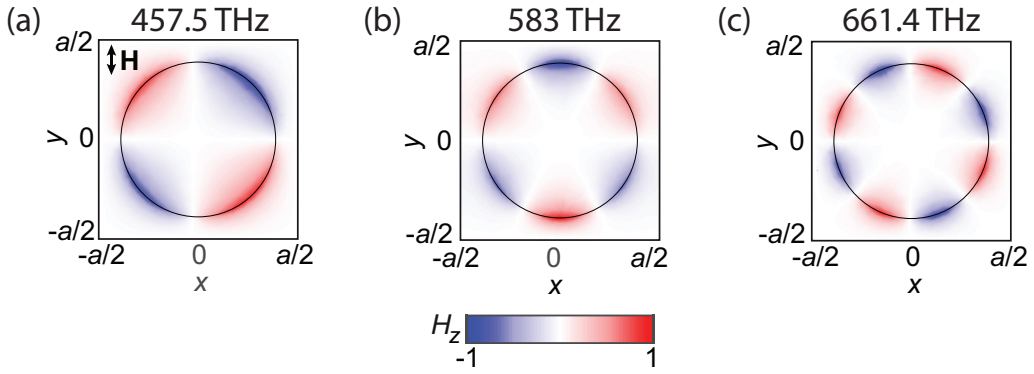

Figure 6.6: Normalized H_z at the hole centre for $\theta = 5^\circ$ TM polarised incidence at the indicated frequencies.

Fig. 6.5(a) and Fig. 6.5(b) show the angular transmittance and absorption spectra simulated with the Frequency Domain (FD) solver of CST Microwave Studio when a TM polarised plane wave impinges the structure. When $\theta \neq 0^\circ$, three different modes, causing minima (maxima) in the transmission (absorption) spectra, can be distinguished. These are the 2nd, 3rd and 4th order WGMs, which resonate at 460, 585 and 660 THz, respectively. Fig. 6.6 shows the corresponding normalized H_z at a mid-plane for $\theta = 5^\circ$, which exhibits the expected multipole patterns. These results are in good agreement with those obtained in the previous section for isolated holes, although slightly red-shifted due to near-field coupling [22, 32, 33].

Role of the lattice symmetries

In the previous chapter, the symmetries of the lattice where shown to play a key role in enabling/disabling light coupling to particular mode orders in nano-disk arrays, section 5.3.1. Nano-holes EP-WGMs sharing a similar feature follows from Babinet's principle. This can be verified by analysing Fig. 6.7. The field distribution of the EP-WGMs when the lattice is square (4-fold symmetry) and hexagonal (3-fold symmetry) are respectively shown in Fig. 6.7(a) and 6.7(b). As in the nano-disks case, the 4-fold symmetry enables the odd-order modes (e.g. the hexapole) to become bright at normal incidence but not the even-order modes. Similarly, the 3-fold symmetry prevents the excitation of even-order modes (double reflection symmetry), in addition to the hexapole, which shares the same symmetries as the lattice (equivalent to the quadrupole - square lattice case). The symmetry breaking

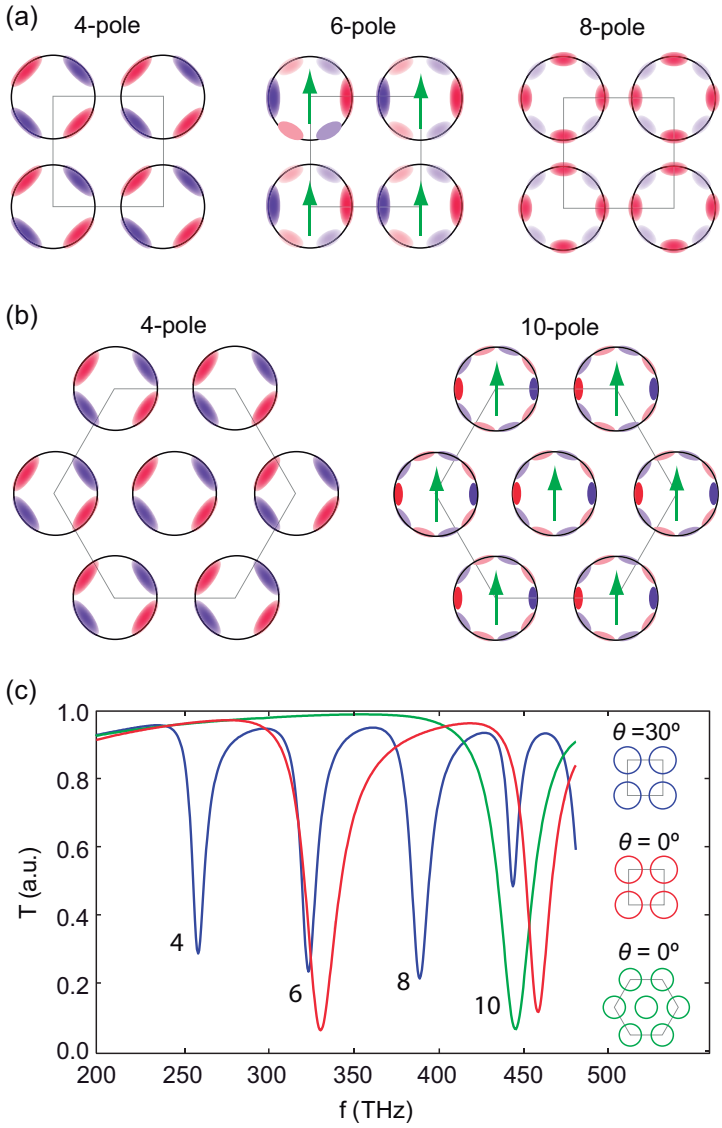

Figure 6.7: Influence of the lattice symmetries on the hole array optical response. The H_z distribution that may arise from the interactions between adjacent holes is shown for different EP-WGM orders in a (a) square and (b) hexagonal lattice. Red areas correspond to positive magnitudes whilst blue indicate negative values. The appearance of a dipole moment is indicated with a green arrow. (c) Transmittance spectra of a hole array with $t = 5$ nm, $r = 160$ nm, and $a = 400$ nm for different lattice/angle configurations. The number of poles is indicated next to each resonance.

introduced by oblique incident light is required for the remaining dark modes to become bright, as shown in the transmittance response in Fig. 6.7(c).

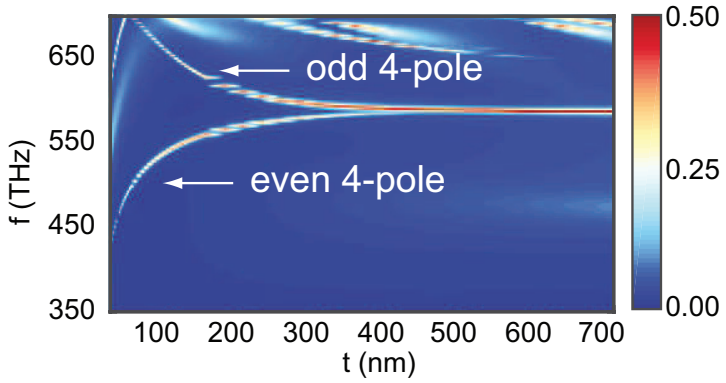

Figure 6.8: Absorption spectra versus t for $\theta = 2°$ TM incidence.

Effect of the film thickness

Fig. 6.8 shows the absorption spectra of a hole array with $a = 400$ nm, $r = 160$ nm and varying t. The angle of incidence is $\theta = 2°$. The effect of the film thickness is also equivalent to the nano-disk case. For sufficiently thick films, a unique EP-WGM highly confined to the edge of the input interface is excited; in particular, for $t > 400$ nm. This mode gives $T = 0$, $A \sim 0.5$ and a very low frequency dispersion, making it suitable for implementing single layer zero transmission absorbers (zero transmission absorbers usually require two metallic films, one of them patterned, separated by a dielectric [34]) which may additionally offer polarisation selectivity by choosing the appropriate EP-WGM order. For films with medium thickness (50 nm $< t <$ 400 nm), the input and output interfaces are close enough for an EP-WGM to evanescently excite the other one, resulting in mode hybridization. Lastly, for thin films ($t < 50$ nm), there is a unique mode whose resonant frequency rapidly decreases with decreasing t. This could be exploited for realising low frequency compact resonators. The case of $t \to 0$ is especially interesting. Recent studies on the plasmonic properties of 2D sheets of monolayer graphene perforated with anti-dots arrays report a close relation between these and ultra-thin hole-arrays [35]. This suggests that anti-dots may support similar EP-WGMs.

Application to sensors with very high figures of merit

WGMs are particularly well suited for sensing applications thanks to the high Q-factors of their corresponding resonances [18]. The EP-WGMs investigated in this thesis also offer high Q-factors. For instance, Fig. 6.9 shows the transmittance

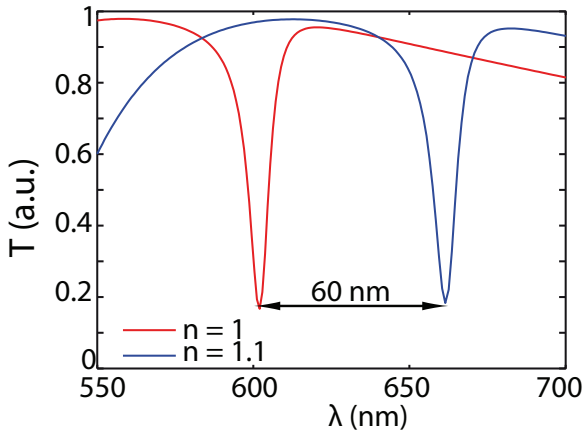

Figure 6.9: Sensing with EP-WGM. We show the variation in the transmittance of a square hole array with $t = 50$ nm, $r = 160$ nm, and $a = 400$ nm as the refractive index of the background medium changes from 1 to 1.1.

of an array of nano-holes with $t = 50$ nm, $r = 160$ nm and $a = 400$ nm. The resonance in that case exhibits Q = 81 and a line-width as narrow as 7.3 nm. Higher Q-factors are very challenging to achieve, the few cases in which this value is exceeded often rely on much larger micro-structures [20, 36], whilst line-widths below 10 nm are considered as ultra-narrow [37]. Additionally, EP-WGMs are very sensitive to the environment, a sought after feature for Localised Surface Plasmon Resonance (LSPR) sensors, which are becoming increasingly popular due to their simplicity, low fabrication cost and ability to probe nano scale sensing volumes and even observe nearby molecular interactions [38–40].

The quality of a sensor is usually measured via its Figure of Merit (FOM), which is defined as the ratio of sensitivity to line-width, being below 5-10 in most cases [39, 40]. In the case depicted in Fig. 6.9, the resonance undergoes a 60 nm shift in wavelength upon a variation of $\Delta n = 0.1$ refractive index units (from 1 to 1.1) in the index of the background medium. Since the sensitivity can be obtained as the ratio between the wavelength and the refractive index variation $S = \Delta\lambda/\Delta n$, this corresponds to a 600 nm per refractive index unit sensitivity. The combination of the narrow line-width and high sensitivity provided results in a very efficient sensor with FOM = 82, which is among the highest values reported to date for plasmonic sensors [38–40] and the highest for a pure LSPR (higher values were obtained for coupled localized and distributed modes [41]), with the advantage that no additional bright mode is required for its excitation.

Experimental observation of a quadrupole

Since nano-disks and nano-patches studied in chapter 5 exhibited similar EPs, EP-WGMs are also expected in nano-holes with non-circular shapes. An EP-WGM was experimentally measured in a metamaterial consisting of a periodic array of square holes [31]. However, that work was focused on a different optical band displaying a negative refractive index and the EP-WGM was overlooked. The zero-transmission band appearing at approximately 1.6 eV (774 nm) in the band diagram shown in Fig. 4 of [31] corresponds to a quadrupole EP-WGM. The simulated H-field shows a quadrupole confined to the hole edges, Fig. 6.10. Note that the zero-transmission band splits into two as the incidence angle increases. The reason for this is that the structure presented in [31] consists of two metallic hole arrays ($t = 35$ nm) separated by a 30 nm dielectric spacer. As a consequence, the EP-WGM of each hole array hybridizes resulting in symmetric and antisymmetric modes resonating at different frequencies. This analysis explains the results reported in [31] which in turn experimentally validate the theory of EP-WGMs proposed in this thesis. Moreover, the band diagram shows EP-WGMs and waveguide modes. In particular, the first-order waveguide mode corresponds to the transmission band at 667 nm, i.e. the waveguide is at cut-off at the resonant frequency of the quadrupole EP-WGM.

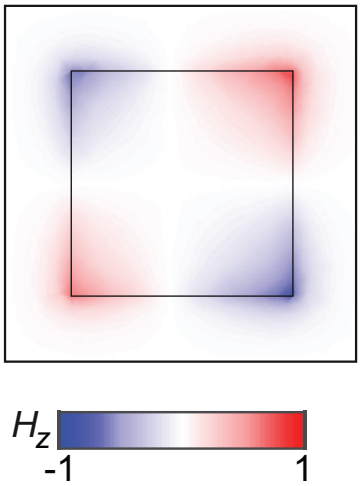

Figure 6.10: Quadrupole EP-WGM supported by a square array ($a = 400$ nm) of square holes of side $l = 250$ nm milled in a film with $t = 35$ nm.

6.3 Propagating surface plasmons

In addition to LSPs, it is well documented that hole-arrays can also support SPPs propagating along and confined to the metallo-dielectric interface. Light coupling to these modes is known to originate EOT in sub-wavelength hole-arrays [5]. In fact, grating coupling is, together with prism coupling, among the techniques traditionally used for the excitation of SPPs in such planar interfaces, which cannot be directly excited by a light beam. The periodicity introduced by the hole-array enables momentum matching between light and SPPs which is not possible otherwise.

This can be illustrated by considering the interface formed between two semi-infinite media with permittivities ϵ_1 and ϵ_2, Fig. 6.11. Without loss of generality, the interface is parallel to the x-axis and normal to $\hat{z}$. Light propagates across the dielectric medium ($\epsilon_1 \in \mathbb{R}$) towards the metal ($\epsilon_2 \in \mathbb{C}$). Assuming a time dependence of the form $\exp[j\omega t]$, the dispersion relation of the SPPs in such a source free scenario can be obtained from the following Maxwell's equation in phasor form

$$\nabla \times \vec{H} = j\omega \vec{D}. \tag{6.1}$$

Since SPPs are TM in nature (Transverse Electric (TE) solutions don't allow field confinement to the interface [42, 43]), they are better described by their in-plane magnetic field component

$$H_y = H_0 f(z) \exp[-jk_x x], \tag{6.2}$$

where k_x is the in-plane complex propagation constant, H_0 is a normalization constant and the propagation is assumed to be along $\hat{x}$. The term $f(z)$ describes the z dependence of the magnetic field so that it exponentially decays with increasing

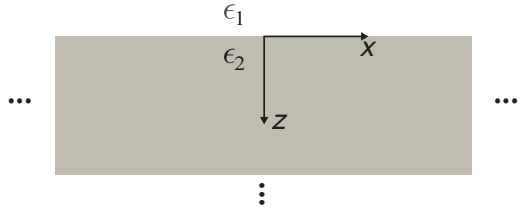

Figure 6.11: Metallo-dielectric interface.

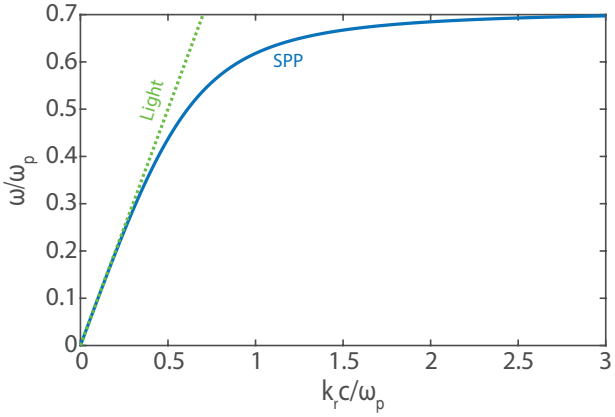

Figure 6.12: Dispersion relation of a SPP propagating across a flat air-silver interface. The light line is shown in green.

distance to the interface. Additionally, $f(z)$ must guarantee that H_y is continuous at the interface ($z = 0$). Therefore, $f(z)$ can be written as

$$f(z) = \begin{cases} \exp[k_{z_1} z], & z < 0 \\ \exp[-k_{z_2} z], & z > 0 \end{cases} \tag{6.3}$$

where k_{z_i} with $i = 1, 2$ are the wavevectors in the two media and fulfil the equality

$$k_{z_i}^2 = k_x^2 - \epsilon_i k_0^2. \tag{6.4}$$

Combining (6.1) and (2.7), the non-zero components of the electric field are

$$E_x = \frac{j}{\omega \epsilon_0 \epsilon_i} \frac{\partial H_y}{\partial z}, \tag{6.5}$$

$$E_z = -\frac{k_x}{\omega \epsilon_0 \epsilon_i} H_y. \tag{6.6}$$

After some simplification, the tangential component of the E-field in each medium can be written as

$$E_x = \begin{cases} \frac{j}{\omega \epsilon_0 \epsilon_1} k_{z_1} H_y, & z < 0 \\ \frac{-j}{\omega \epsilon_0 \epsilon_2} k_{z_2} H_y, & z > 0 \end{cases} \tag{6.7}$$

Enforcing continuity of E_x across the interface yields

$$\frac{k_{z_1}}{k_{z_2}} = \frac{-\epsilon_1}{\epsilon_2}. \tag{6.8}$$

Finally, the dispersion relation of SPPs can be obtained combining (6.4) and (6.8). This is [43]

$$k_x = k_0 \sqrt{\frac{\epsilon_2 \epsilon_1}{\epsilon_2 + \epsilon_1}}. \tag{6.9}$$

The dispersion relation in the real $k - \omega$ plane of the SPPs supported by an air-silver interface given by (6.9) is depicted in Fig. 6.12. The dispersion curves of the SPPs lie at the right of the light-line, prohibiting momentum matching and in turn coupling.

6.3.1 Thin metallic films in asymmetric environments

The dispersion relation of SPPs may be dramatically different when considering a bounded thin finite metal film instead [44]. If the thickness of the film is smaller than the attenuation length, coupling between the SPPs on the upper- and lower-interfaces results in the formation of two hybrid modes with thickness-dependent dispersion relation and opposite field distributions, termed the LR- and the SR-SPP, respectively. For thick films, these modes become degenerate and their dispersion relation tends towards that of the SPP of a single flat interface which is described by (6.9) [43].

A finite thin film of thickness d and complex permittivity ϵ_2 bounded by semi-infinite dielectric media of real permittivity ϵ_1 and ϵ_3 is considered, inset of Fig. 6.13(a). The associated dispersion relation shows a complex behaviour and cannot be solved analytically. For the symmetric case ($\epsilon_1 = \epsilon_3$), the LR- and SR- modes can be studied separately [43]. An approximate solution for the LR-SPPs dispersion relation can be found in [8]. However, a simple closed-form solution to analyse SR-SPPs is yet to appear. If such a solution is to be available, the spectral position of the SR-SPP resonances could be readily obtained. These resonances have been recently exploited in a wide variety of applications [9–13]. For instance, it has been recently reported that SR-SPPs play a key role in EOT and in the design of absorbers [45], polarisers [7] and colour filters [46, 47]. Likewise, they have also shown promise

in biosensing [48] and for implementing plasmonic waveguides [49]. Therefore, the solution reported in this thesis has the potential to significantly simplify and speed-up the design process of these devices while providing an intuitive understanding of the effect of the geometry on the excitation of these plasmons.

Simple analytical solution to short-range surface plasmons

In the following and without loss of generality, the example presented in the inset of Fig. 6.13(a) is considered. The magnetic tangential component of SPPs propagating along x is described by (6.2), whilst the non-vanishing E-field components are given by (6.5) and (6.6). As before, the term $f(z)$ describes the z dependence of the magnetic field. This has to be chosen so that a) the fields are confined to the interface and b) the boundary conditions are satisfied. Therefore, $f(z)$ can be written as [50]

$$f(z) = \begin{cases} \exp[k_{z_1} z], & z < 0 \\ \cosh(k_{z_2} z) + \frac{k_{z_1}\epsilon_2}{k_{z_2}\epsilon_1} \sinh(k_{z_2} z), & 0 > z > d \\ \left[\cosh(k_{z_2} d) + \frac{k_{z_1}\epsilon_2}{k_{z_2}\epsilon_1} \sin(k_{z_2} d)\right] \exp[-k_{z_3}(z-d)], & z > d \end{cases} \tag{6.10}$$

where $j = 1, 2, 3$ indexes the three media.

Forcing continuity of the tangential electric component, the following dispersion relation is obtained [50]

$$\tanh(k_{z_2} d)(\epsilon_1 \epsilon_3 k_{z_2}^2 + \epsilon_2^2 k_{z_1} k_{z_3}) = -k_{z_2}\epsilon_2(\epsilon_1 k_{z_3} + \epsilon_3 k_{z_1}). \tag{6.11}$$

This transcendental equation can only be solved numerically. If the thickness is small enough so that $|k_{z_2} d| \ll 1$, by means of a Taylor series expansion up to first order, the hyperbolic tangent in (6.11) can be simplified to

$$k_{z_2} d(\epsilon_1 \epsilon_3 k_{z_2}^2 + \epsilon_2^2 k_{z_1} k_{z_3}) = -k_{z_2}\epsilon_2(\epsilon_1 k_{z_3} + \epsilon_3 k_{z_1}). \tag{6.12}$$

For a fixed frequency, the propagation constant of the SR-SPPs is far smaller than that of the SPP of each single flat interface, which is given by (6.9). That is, SR-SPPs satisfy the inequality $k_x \ll k_{x_j}^{SPP}$ for $j = 1, 3$. This inequality can be

expressed as $k_{z_2}/\epsilon_2 \ll k_{z_j}/\epsilon_j$. As a result, the first term of the left hand side of (6.12) becomes negligible and it can be reduced to

$$d\epsilon_2^2 k_{z_1} k_{z_3} = -\epsilon_2(\epsilon_1 k_{z_3} + \epsilon_3 k_{z_1}). \tag{6.13}$$

A similar reasoning can be applied to the LR-SPPs, where the term $\epsilon_1\epsilon_3 k_{z_2}^2$ may be neglected.

Assuming $\epsilon_1 \neq \epsilon_3$, the wavevector in medium 3 can be written as a function of that in medium 1, i.e.

$$k_{z_3} = \sqrt{k_{z_1}^2 + k_0^2\Delta}, \tag{6.14}$$

where $\Delta = \epsilon_1 - \epsilon_3$ may take any real value. In this sense, (6.13) can be expressed as a function of a single variable, k_{z_1}. Additionally, if $|k_0^2\Delta/k_{z_1}^2| < 1$, a further simplification of the square root in (6.14) can be performed by means of a Taylor series expansion up to first order. Subsequently, a monic cubic equation, (6.15), with coefficients $p = (2\epsilon_1 - \Delta)/(d\epsilon_2)$, $q = k_0^2\Delta/2$ and $r = k_0^2\Delta\epsilon_1/(2d\epsilon_2)$ is obtained

$$k_{z_1}^3 + pk_{z_1}^2 + qk_{z_1} + r = 0. \tag{6.15}$$

Such an equation can be solved analytically using the cubic formula. The associated root corresponding to the SR-SPP is given by

$$k_{z_1}^{SR} = -\frac{p}{3} + A - \frac{3q - p^2}{9A}, \tag{6.16}$$

where

$$A = \frac{(-2p^3 + 9pq - 27r + B)^{1/3}}{3\sqrt[3]{2}}, \tag{6.17}$$

and

$$B = 3\sqrt{3}\left(-p^2q^2 + 4q^3 + 4p^3r - 18pqr + 27r^2\right)^{1/2}. \tag{6.18}$$

Finally, the complex propagation constant of the SR-SPPs can be obtained via the combination of (6.4) and (6.16)

$$k_x^{SR} = \sqrt{\left(k_{z_1}^{SR}\right)^2 + \epsilon_1 \left(\frac{\omega}{c}\right)^2}. \tag{6.19}$$

Numerical example: short-range plasmons of a thin silver film

Next, a numerical example is studied. The dispersion relation of a $d = 15$ nm silver film when a vacuum superstrate ($\epsilon_3 = 1$) and a glass substrate are considered ($\epsilon_1 = 2.25$) is depicted in Fig. 6.13(a). Additionally, the free-standing case ($\epsilon_1 = \epsilon_3 = 1$) is shown in Fig. 6.13(b), and a higher contrast case ($\epsilon_3 = 1$ and $\epsilon_1 = 11$) in Fig. 6.13(c).

For the sake of comparison, the approximate solution of the dispersion relation of the SR-SPPs according to (6.16)-(6.19) appears superimposed to the numerical solution of (6.11). In the short-k range, the agreement is excellent for both the asymmetric ($\epsilon_1 \neq \epsilon_3$) and the symmetric ($\epsilon_1 = \epsilon_3$) environments, even when the contrast is as high as $\Delta = 10$. The second mode arising at higher frequencies corresponds to the LR-SPP. The dispersion curves of both the LR- and SR-SPPs lie at the right of the light-lines and hence, cannot be directly excited by normally incident light impinging from the dielectrics [43]. The required extra momentum can be provided via grating coupling [51], as in the case considered later in section 6.3.2. To further evaluate the accuracy of the derived closed-form, the insets of Fig. 6.13(b) and 6.13(c) show the percentage deviation of the approximate analytical solution from that obtained by numerically solving (6.11) in each case. Small discrepancies arise towards the long-k range, where $|k_{z_2} d| \ll 1$ is not perfectly fulfilled. The maximum error, which corresponds to the case $\Delta = 10$ is below 11%.

The symmetric case, Fig. 6.13(b), is merely a special case of the most general asymmetric configuration. In this scenario, the dispersion relation can be directly obtained by simplification of the cubic equation (equating Δ to zero); (6.15) becomes linear and the solution simplifies to

$$k_{z_1}^{SR} = \frac{-2\epsilon_1}{d\epsilon_2}. \tag{6.20}$$

As in the asymmetric case, the wavevector can be substituted in (6.19) to obtain

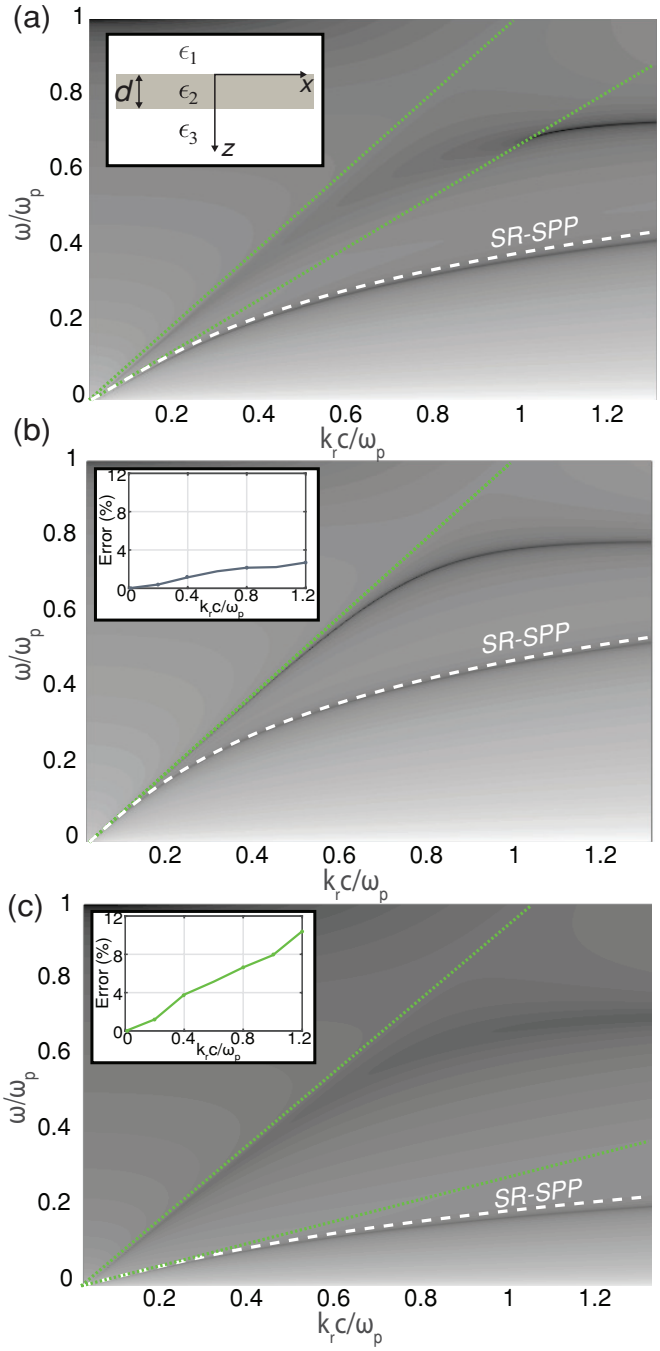

Figure 6.13: Dispersion relation of a 15-nm-thick silver film (gray scale) when the film is (a) sandwiched between dielectrics with $\epsilon_1 = 2.25$ and $\epsilon_3 = 1$, (b) free-standing ($\epsilon_1 = \epsilon_3 = 1$), and (c) when $\epsilon_1 = 11$ and $\epsilon_3 = 1$. Darker colours correspond to the roots of the dispersion relation. The light lines in the different dielectrics are shown as green dotted lines. The approximate solution for the SR-SPP is indicated by the white dashed line. Inset (a): Metallic film with thickness d and permittivity ϵ_2 sandwiched between two semi-infinite dielectric media with ϵ_1 and ϵ_3. Inset (b)-(c): Percentage deviation from the numerical solution in each case.

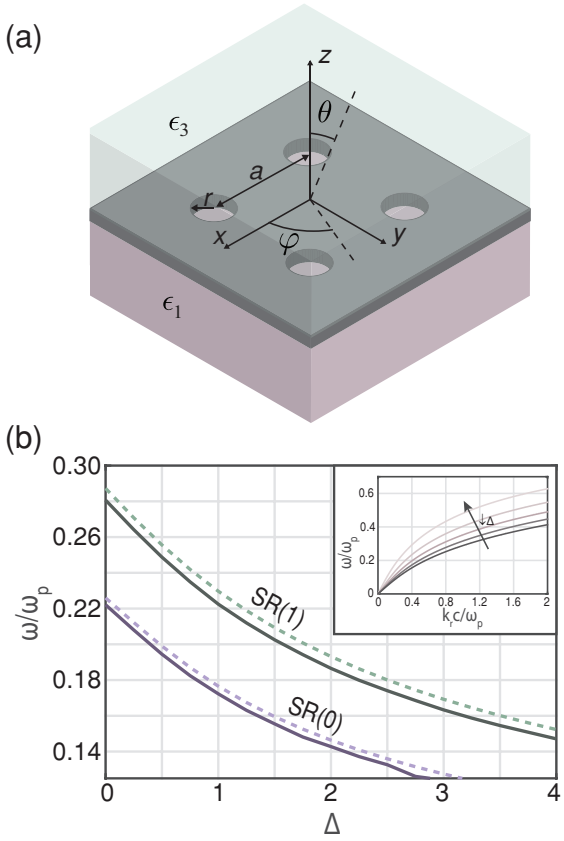

Figure 6.14: (a) Proposed geometry. The plane-wave impinges from $-\hat{z}$. (b) Closed-form (dashed lines) and simulated (solid lines) resonance frequencies of the lower order modes when the superstrate is vacuum ($\epsilon_3 = 1$) and the contrast between this and the substrate is $\Delta = 0 - 4$. The geometrical parameters are: $d = 15$ nm, $r = 20$ nm and $a = 500$ nm. Inset: approximate dispersion relation of the SR-SPP modes for $\Delta = 0 - 4$. Lighter shades correspond to smaller contrasts.

the propagation constant of the SR-SPPs, Fig. 6.13(b). Note that (6.20) agrees with that reported by *Raether* in [43] after approximating the hyperbolic tangent by its Taylor expansion.

6.3.2 Short-range plasmons in hole arrays

A square grating of sub-wavelength holes with radius $r = 20$ nm and periodicity $a = 500$ nm perforated in a $t = 15$ nm film is considered next, Fig. 6.14(a). Such periodic array imparts the necessary additional momentum to the impinging light

for the excitation of SPPs yet supports the propagation of SR-SPPs. The in-plane component of the momentum is

$$|k_{||}| = |(k_{L_x} \pm nG)\hat{x} + (k_{L_y} \pm mG)\hat{y}|, \tag{6.21}$$

where $G = 2\pi/a$ is the reciprocal lattice constant and k_{L_x} and k_{L_y}, the x and y components of the incident light momentum. Considering that the equality $k_x = k_{||}$ must be satisfied in order to excite SPPs, and that (6.16) holds, the frequencies at which an incoming TM polarised plane wave will couple to the SR-SPPs can be obtained analytically by the solution of the two simultaneous equations.

To illustrate this, Fig. 6.14(b) shows the resonant frequencies of the two lower order SR-modes for different permittivity contrasts Δ, maintaining $\epsilon_3 = 1$. To validate the approximation, the SR-SPP resonances calculated using (6.16)-(6.19) are superimposed to the simulated ones. The simulated resonant frequencies are obtained from the spectral position of the absorption maxima as given by CST Microwave Studio. The cut-off frequency of the holes can be calculated from (5.9), by simply exchanging the roles of the dielectric and the metal. For $r = 20$ nm empty holes, $\omega_{co}/\omega_p = 1.62$, which is far above the upper frequency limit considered here. Therefore, the holes do not support any propagating modes and it is reasonable to consider them as weak scatterers. As shown in Fig. 6.14(b), the derived solution predicts accurately the spectral position of the absorption peaks independently of the permittivity contrast between both surrounding dielectric media. Increasing the contrast leads to a red-shift on the mode resonances, which can be explained by looking at the inset of Fig. 6.14(b). There, it can be seen how for a fixed propagation constant, higher Δ results in the mode arising at lower frequencies.

The same 2D square grating is subsequently embedded in a symmetric environment ($\epsilon_1 = \epsilon_3$). Such a configuration can be experimentally realized by fabricating symmetric samples or, more commonly, including index matching liquids [52–54]. Fig. 6.15(a) shows the simulated angular absorption spectra when a plane wave is impinging from ($\varphi = 0°$, $\theta = 0 - 30°$). There, it can be observed that the derived solution is also accurate in the case of oblique illumination. Owing to the oblique incidence, there is an extra in-plane component to the wavevector and the SR-SPPs hybridize into even and odd order modes, as shown in the scattering spectra. To

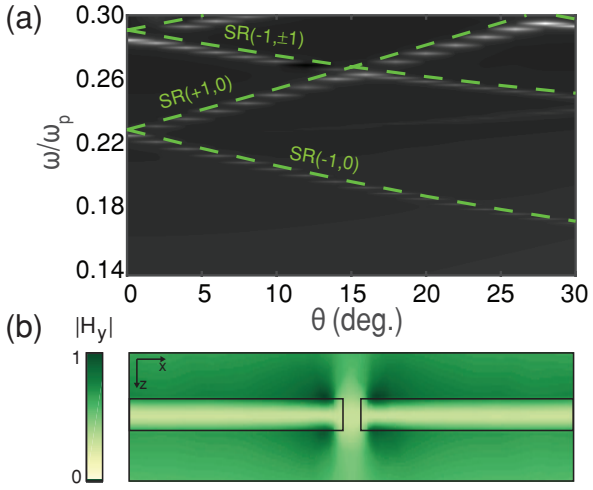

Figure 6.15: (a) Simulated angular absorption spectra at the $\varphi = 0°$ plane. Lighter colours correspond to higher values of absorption. The superimposed green lines indicate the theoretical resonance frequencies of the (n, m) order SR-SPP. (b) Normalized $|H_y|$ distribution at the xz plane for $\omega/\omega_p = 0.22$ and normal incidence. (a)-(b) $d = 15$ nm, $a = 500$ nm and $r = 20$ nm

verify that the excited SPP is indeed the SR-SPP, Fig. 6.15(c) shows the magnitude of the parallel component of the magnetic field, H_y, normalized to its maximum at $\omega/\omega_p = 0.22$ and normal incidence. As expected for the SR-SPPs, H_y is zero at the center the metal film.

Thus far, any effects due to the holes, other than providing a mechanism for the excitation of SPPs, have been neglected. The effect of increasing the size of the apertures is investigated in Fig. 6.16(a). As it can be seen, for larger holes, the simulations increasingly deviate from the theory due to the limited validity of the empty lattice approximation. The red-shift of the resonances with respect to the predictions has been extensively studied in the literature [55–57] and is out of the scope of this thesis.

The thickness of the metal film plays a key role in the dispersion relation of thin films and thus, in the excitation of SR-SPPs. Moreover, the approximation derived in this work is thickness-dependent and remains valid as long as $|k_{z_2} d| \ll 1$. Therefore, the estimated spectral position where resonance occurs is more accurate for thinner films, as confirmed by Fig. 6.16(b). Above a critical thickness, the SR- and LR-SPPs are uncoupled and converge to the SPP mode of the single interface, (6.9), which

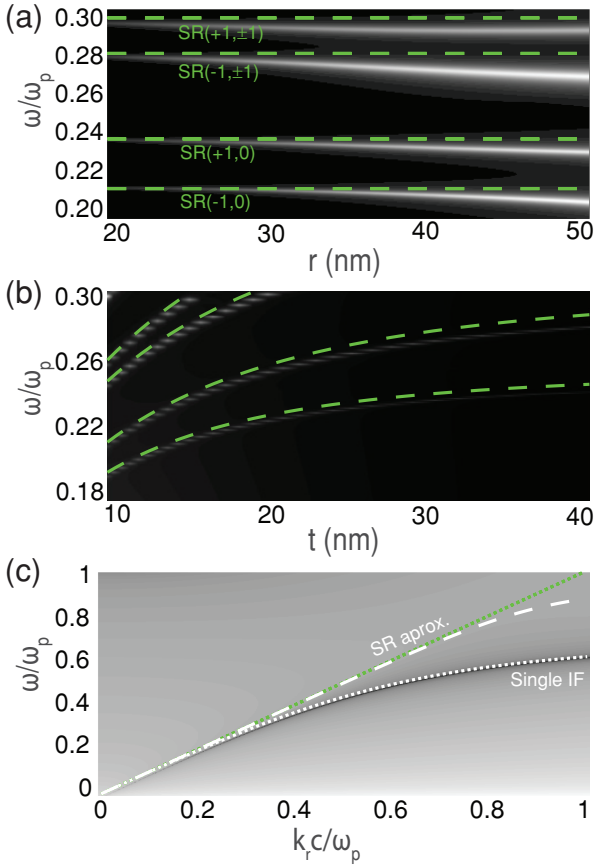

Figure 6.16: Absorption at ($\varphi = 0°$, $\theta = 5°$) incidence for a grating with $a = 500$ nm (a) vs. hole radius when $d = 15$ nm; (b) vs. film thickness when $r = 20$ nm. The predicted dispersion curves are shown as green dashed lines. (c) Dispersion relation of a 300-nm-thick silver film. The light line is shown as a green dotted line. The approximate solution is indicated by the white dashed line and that of the single interface by the white dotted line.

is not well described by (6.20). To illustrate this, the dispersion relation given by (6.11) is solved for a $t = 300$ nm film. The predicted normalized dispersion curve of the SR-SPP according to (6.20) and that of the single interface appear superimposed to the numerical solution of (6.11) in Fig. 6.16(c). The LR- and SR-SPPs are degenerate in this case and (6.9) is more accurate for describing the overall behaviour.

6.4 Conclusion

Metallic apertures have been intensively studied since the first observation of EOT. They can provide a negative index of refraction [31], which may be employed in turn for perfect imaging [58] or light storage [59]. The results presented in section 6.2 provide new insight into the fundamental physics behind the unique optical response of both individual nano-holes and 2D arrays. We showed that nano-holes can support EP-WGMs [J8]. Despite such modes can strongly influence the spectral response and allow explaining previous experimental results found in metamaterials, they had been overlooked so far. As an example, by including the EP-WGMs, we were able to fully interpret the band diagram of the fishnet structure reported in [31]. Therefore, understanding EP-WGMs is crucial to better explain the optical response of nano-hole based plasmonic devices, as well as to prevent interference that may degrade their intended performance. Our results suggest a close relation between these modes and the nano-disks' EPs investigated in chapter 5. Their potential applications include zero-transmittance absorbers with only a single metal layer and high performance sensors for detecting nanoscale analytes and/or observing molecular interactions.

In section 6.3, we focused on propagating SR-SPPs and derived a simple expression for calculating their dispersion relation in both symmetric and asymmetric environments [J9]. The proposed closed-form can be used to predict the resonances associated with this type of modes and hence ease and speed-up the design of SR-SPPs based applications [9–13]. The dispersion curves estimated with the proposed approximation and those obtained by numerically solving the transcendental equation for finite metal slabs found an excellent agreement in the short-k region. The derived equation was subsequently applied to calculating the resonant frequencies of a 2D array of sub-wavelength holes (section 6.3.2). Within the empty lattice approximation limitations, the estimated and simulated resonant frequencies were in very good agreement for normal and oblique incident light. Our solution remains valid as long as $|k_{z_2}d| \ll 1$. Above a critical thickness, the SR- and LR- modes become degenerate and the dispersion curves converge to that of a single smooth interface, as suggested by the simulations.

References

[1] S. Yokogawa, S. P. Burgos, and H. A. Atwater, "Plasmonic color filters for CMOS image sensor applications," *Nano Lett.*, vol. 12, no. 8, pp. 4349–4354, 2012.

[2] K. Konishi, T. Higuchi, J. Li, J. Larsson, S. Ishii, and M. Kuwata-Gonokami, "Polarization-controlled circular second-harmonic generation from metal hole arrays with threefold rotational symmetry," *Phys. Rev. Lett.*, vol. 112, p. 135502, Apr 2014.

[3] S. Jeon, J.-H. Lee, J.-H. Jeong, Y. S. Song, C.-K. Moon, J.-J. Kim, and J. R. Youn, "Vacuum nanohole array embedded phosphorescent organic light emitting diodes," *Sci. Rep.*, vol. 5, no. 8685, Mar 2015.

[4] H. A. Bethe, "Theory of diffraction by small holes," *Phys. Rev.*, vol. 66, pp. 163–182, Oct 1944.

[5] T. W. Ebbesen, H. J. Lezec, H. F. Ghaemi, T. Thio, and P. A. Wolff, "Extraordinary optical transmission through sub-wavelength hole arrays," *Nature*, vol. 391, no. 6668, pp. 667–669, 1998.

[6] C. Genet and T. Ebbesen, "Light in tiny holes," *Nature*, vol. 445, no. 7123, pp. 39–46, 2007.

[7] J. Braun, B. Gompf, G. Kobiela, and M. Dressel, "How Holes Can Obscure the View: Suppressed Transmission through an Ultrathin Metal Film by a Subwavelength Hole Array," *Phys. Rev. Lett.*, vol. 103, no. 20, p. 203901, Nov. 2009.

[8] F. Yang, J. Sambles, and G. Bradberry, "Long-range surface modes supported by thin films," *Phys. Rev. B*, vol. 44, no. 11, 1991.

[9] S. Xiao and N. A. Mortensen, "Surface-plasmon-polariton-induced suppressed transmission through ultrathin metal disk arrays." *Opt. Lett.*, vol. 36, no. 1, pp. 37–9, Jan. 2011.

[10] Y. Alaverdyan, B. Sepúlveda, L. Eurenius, E. Olsson, and M. Käll, "Optical antennas based on coupled nanoholes in thin metal films," *Nature Phys.*, vol. 3, no. 12, pp. 884–889, Nov. 2007.

[11] S. G. Rodrigo, L. Martín-Moreno, A. Y. Nikitin, A. V. Kats, I. S. Spevak, and F. J. García-Vidal, "Extraordinary optical transmission through hole arrays in optically thin metal films," *Opt. Lett.*, vol. 34, no. 1, pp. 4–6, Jan 2009.

[12] B. Zeng, Y. Gao, and F. J. Bartoli, "Ultrathin nanostructured metals for highly transmissive plasmonic subtractive color filters." *Sci. Rep.*, vol. 3, p. 2840, Jan. 2013.

[13] B. Zeng, Z. H. Kafafi, and F. J. Bartoli, "Transparent Conducting Electrodes based on 1D and 2D Ag Nanogratings for Organic Photovoltaics," *ArXiv e-prints*, Dec. 2014.

[14] Lord Rayleigh, "CXII. The problem of the whispering gallery," *Philos. Mag. 6*, vol. 20, no. 120, pp. 1001–1004, 1910.

[15] C. Liu and J. A. Golovchenko, "Surface trapped X rays: Whispering-gallery modes at $\lambda = 0.7$ å," *Phys. Rev. Lett.*, vol. 79, pp. 788–791, Aug 1997.

[16] B. Gayral, J. M. Gérard, A. Lemaître, C. Dupuis, L. Manin, and J. L. Pelouard, "High-Q wet-etched GaAs microdisks containing InAs quantum boxes," *Appl. Phys. Lett.*, vol. 75, no. 13, 1999.

[17] P. L. Stanwix, M. E. Tobar, P. Wolf, M. Susli, C. R. Locke, E. N. Ivanov, J. Winterflood, and F. van Kann, "Test of Lorentz invariance in electrodynamics using rotating cryogenic sapphire microwave oscillators," *Phys. Rev. Lett.*, vol. 95, p. 040404, Jul 2005.

[18] K. J. Vahala, "Optical microcavities," *Nature*, vol. 424, 2003.

[19] S. I. Bozhevolnyi, V. S. Volkov, E. Devaux, J.-Y. Laluet, and T. W. Ebbesen, "Channel plasmon subwavelength waveguide components including interferometers and ring resonators," *Nature*, vol. 440, 2006.

[20] B. Min, E. Ostby, V. Sorger, E. Ulin-Avila, L. Yang, X. Zhang, and K. Vahala, "High-Q surface-plasmon-polariton whispering-gallery microcavity," *Nature*, vol. 457, 2009.

[21] F.-P. Schmidt, H. Ditlbacher, U. Hohenester, A. Hohenau, F. Hofer, and J. R. Krenn, "Universal dispersion of surface plasmons in flat nanostructures," *Nat. Commun.*, vol. 5, p. 3604, 2014.

[22] J. Prikulis, P. Hanarp, L. Olofsson, D. Sutherland, and M. Kll, "Optical spectroscopy of nanometric holes in thin gold films," *Nano Lett.*, vol. 4, no. 6, pp. 1003–1007, 2004.

[23] T. Rindzevicius, Y. Alaverdyan, B. Sepulveda, T. Pakizeh, M. Käll, R. Hillenbrand, J. Aizpurua, and F. J. García De Abajo, "Nanohole plasmons in optically thin gold films," *J. Phys. Chem. C*, vol. 111, no. 3, pp. 1207–1212, 2007.

[24] M. Hentschel, T. Weiss, S. Bagheri, and H. Giessen, "Babinet to the half: Coupling of solid and inverse plasmonic structures," *Nano Lett.*, vol. 13, no. 9, pp. 4428–4433, 2013.

[25] A. Degiron, H. Lezec, N. Yamamoto, and T. Ebbesen, "Optical transmission properties of a single subwavelength aperture in a real metal," *Opt. Commun.*, vol. 239, no. 1-3, pp. 61–66, Sep. 2004.

[26] T. Coenen and A. Polman, "Optical properties of single plasmonic holes probed with local electron beam excitation," *ACS Nano*, vol. 8, no. 7, pp. 7350–7358, 2014.

[27] "Lumerical Solutions, Inc." [Online]. Available: http://www.lumerical.com/tcad-products/fdtd/

[28] D. Lee and D.-S. Kim, "Light scattering of rectangular slot antennas: parallel magnetic vector vs perpendicular electric vector," *Sci. Rep.*, vol. 6, p. 18935, 2016.

[29] C. García-Meca, R. Ortuño, F. Rodríguez-Fortuño, J. Martí, and A. Martínez, "Negative refractive index metamaterials aided by extraordinary optical transmission," *Opt. Express*, vol. 17, no. 8, pp. 6026–6031, Apr 2009.

[30] R. Ortuño, C. García-Meca, F. J. Rodríguez-Fortuño, A. Hakansson, A. Griol, J. Hurtado, J. A. Ayucar, L. Bellieres, P. J. Rodríguez, F. López-Royo, J. Martí, and A. Martínez, "Midinfrared filters based on extraordinary optical transmission through subwavelength structured gold films," *J. Appl. Phys.*, vol. 106, no. 12, p. 124313, 2009.

[31] C. García-Meca, J. Hurtado, J. Martí, A. Martínez, W. Dickson, and A. V. Zayats, "Low-loss multilayered metamaterial exhibiting a negative index of refraction at visible wavelengths," *Phys. Rev. Lett.*, vol. 106, p. 067402, Feb 2011.

[32] A. Y. Nikitin, F. J. García-Vidal, and L. Martín-Moreno, "Surface electromagnetic field radiated by a subwavelength hole in a metal film," *Phys. Rev. Lett.*, vol. 105, p. 073902, Aug 2010.

[33] J. Parsons, E. Hendry, C. P. Burrows, B. Auguié, J. R. Sambles, and W. L. Barnes, "Localized surface-plasmon resonances in periodic nondiffracting metallic nanoparticle and nanohole arrays," *Phys. Rev. B*, vol. 79, p. 073412, Feb 2009.

[34] C. M. Watts, X. Liu, and W. J. Padilla, "Metamaterial electromagnetic wave absorbers," *Adv. Mater.*, vol. 24, no. 23, pp. OP98–OP120, 2012.

[35] A. Y. Nikitin, F. Guinea, and L. Martin-Moreno, "Resonant plasmonic effects in periodic graphene antidot arrays," *Appl. Phys. Lett.*, vol. 101, no. 15, p. 151119, 2012.

[36] X. Zhang, Z. Ma, H. Yu, X. Guo, Y. Ma, and L. Tong, "Plasmonic resonance of whispering gallery modes in an Au cylinder," *Opt. Express*, vol. 19, no. 5, pp. 3902–3907, Feb 2011.

[37] S. H. Lee, T. W. Johnson, N. C. Lindquist, H. Im, D. J. Norris, and S.-H. Oh, "Linewidth-optimized extraordinary optical transmission in water with template-stripped metallic nanohole arrays," *Adv. Funct. Mater.*, vol. 22, no. 21, pp. 4439–4446, 2012.

[38] J. N. Anker, W. P. Hall, O. Lyandres, N. C. Shah, J. Zhao, and R. P. Van Duyne, "Biosensing with plasmonic nanosensors," *Nat. Mater.*, vol. 7, pp. 442–453, 2012.

[39] K. M. Mayer and J. H. Hafner, "Localized surface plasmon resonance sensors," *Chem. Rev.*, vol. 111, no. 6, pp. 3828–3857, 2011.

[40] L. Tong, H. Wei, S. Zhang, and H. Xu, "Recent advances in plasmonic sensors," *Sensors*, vol. 14, no. 5, pp. 7959–7973, 2014.

[41] A. A. Yanik, A. E. Cetin, M. Huang, A. Artar, S. H. Mousavi, A. Khanikaev, J. H. Connor, G. Shvets, and H. Altug, "Seeing protein monolayers with naked eye through plasmonic Fano resonances," *Proc. of the Natl. Acad. of Sci. USA*, vol. 108, no. 29, pp. 11 784–11 789, 2011.

[42] S. A. Maier, *Plasmonics: Fundamentals and applications*. Springer, 2007.

[43] H. Raether, *Surface Plasmons on Smooth and Rough Surfaces and on Gratings*. Springer, 1988.

[44] E. Economou, "Surface plasmons in thin films," *Phys. Rev.*, vol. 182, no. 2, 1969.

[45] W. Bai, Q. Gan, G. Song, and L. Chen, "Broadband short-range surface plasmon structures for absorption enhancement in organic photovoltaics," *Opt. Express*, vol. 18, no. November, pp. 620–630, 2010.

[46] L. Sun, X. Hu, Y. Xu, Q. Wu, B. Shi, M. Ye, L. Wang, J. Zhao, X. Li, Y. Wu, S. Yang, R. Tai, H. Fecht, J. Jiang, and D. Zhang, "Influence of structural parameters to polarization-independent color-filter behavior in ultrathin Ag films," *Opt. Commun.*, vol. 333, pp. 16 – 21, 2014.

[47] L. B. Sun, X. L. Hu, B. Zeng, L. S. Wang, S. M. Yang, R. Z. Tai, H. J. Fecht, D. X. Zhang, and J. Z. Jiang, "Effect of relative nanohole position on colour purity of ultrathin plasmonic subtractive colour filters," *Nanotechnology*, vol. 26, no. 30, p. 305204, 2015.

[48] R. Wan, F. Liu, and Y. Huang, "Ultrathin layer sensing based on hybrid coupler with short-range surface plasmon polariton and dielectric waveguide," *Opt. Lett.*, vol. 35, no. 2, pp. 244–246, Jan 2010.

[49] R. Wan, F. Liu, X. Tang, Y. Huang, and J. Peng, "Vertical coupling between short range surface plasmon polariton mode and dielectric waveguide mode," *Appl. Phys. Lett.*, vol. 94, no. 14, p. 141104, 2009.

[50] J. Burke, G. I. Stegeman, and T. Tamir, "Surface-polariton like waves guided by thin, lossy metal films," *Phys. Rev. B*, vol. 33, no. 8, 1986.

[51] R. H. Ritchie, E. T. Arakawa, J. J. Cowan, and R. N. Hamm, "Surface-plasmon resonance effect in grating diffraction," *Phys. Rev. Lett.*, vol. 21, pp. 1530–1533,

Nov 1968.

[52] A. Krishnan, T. Thio, T. Kim, H. Lezec, T. Ebbesen, P. Wolff, J. Pendry, L. Martin-Moreno, and F. Garcia-Vidal, "Evanescently coupled resonance in surface plasmon enhanced transmission," *Opt. Commun.*, vol. 200, pp. 1 –7, 2001.

[53] L. Pang, K. A. Tetz, and Y. Fainman, "Observation of the splitting of degenerate surface plasmon polariton modes in a two-dimensional metallic nanohole array," *Appl. Phys. Lett.*, vol. 90, no. 11, p. 111103, 2007.

[54] M. J. A. de Dood, E. F. C. Driessen, D. Stolwijk, and M. P. van Exter, "Observation of coupling between surface plasmons in index-matched hole arrays," *Phys. Rev. B*, vol. 77, p. 115437, Mar 2008.

[55] "Diffracted evanescent wave model for enhanced and suppressed optical transmission through subwavelength hole arrays." *Opt. Express*, vol. 12, no. 16, pp. 3629–51, Aug. 2004.

[56] D. Pacifici, H. J. Lezec, L. a. Sweatlock, R. J. Walters, and H. a. Atwater, "Universal optical transmission features in periodic and quasiperiodic hole arrays," *Opt. Express*, vol. 16, no. 12, p. 9222, Jun. 2008.

[57] H. Liu and P. Lalanne, "Microscopic theory of the extraordinary optical transmission." *Nature*, vol. 452, no. 7188, pp. 728–31, Apr. 2008.

[58] J. B. Pendry, "Negative refraction makes a perfect lens," *Phys. Rev. Lett.*, vol. 85, pp. 3966–3969, Oct 2000.

[59] K. L. Tsakmakidis, A. D. Boardman, and O. Hess, "Trapped rainbow storage of light in metamaterials," *Nature*, vol. 450, pp. 397–401, 2007.

El que resiste, gana.

Camilo José Cela

7

Conclusion

This thesis has aimed to be used as a tool for researchers dealing with the electromagnetic response of 2D periodic arrays of passive elements in both the mm- and nm- wavelength range. Novel configurations (form-birefringent waveplates including those exploiting Gradient Index (GRIN) optics and conformed to curved surfaces, optical Partially Reflecting Surfaces (PRSs) for Leaky-Wave (LW) nano-antennas and frequency selective arrays of nano-particles and nano-holes) and analysis methods (Jones' and Berreman's formalisms, an adaptation of classical thin films theory, numerical simulations using CST Microwave Studio and Lumerical and derived analytical approximations) of these structures have been presented driven by different requirements and contributing to the development of future antenna systems.

Motivated by the different response of materials and the requirements of the intended applications in this two frequency regimes, the thesis has been structured in two main parts; chapters 2 and 3 focus on mm-waves, whilst chapters 4-6 deal with nm-waves. Similarly, dielectric structures for high power systems are reported in chapters 2 and

3, whilst metallic structures are studied in chapters 4-6.

At low frequencies, all-dielectric structures are more suitable for high power applications than their metallic counterparts, whilst simultaneously addressing oxidation and corrosion problems intrinsic to metallic structures. Motivated by the utilisation of periodic arrays in antenna systems for Ka-band satellite communications, where the abovementioned constrains constitute real problems, in chapter 2, we set up the theoretical framework necessary for their synthesis and analysis in the shape of form-birefringent all-dielectric waveplates. We have further provided guidelines to evaluate the most appropriate analytical method to use, based on the complexity of the design and the desired accuracy. The proposed artificial waveplates enable similar performance to optical waveplates but in the microwave regime, where the availability of natural birefringent materials and the exhibited level of birefringence are restricted. Two topologies of a Linear Polarisation (LP)-to-Circular Polarisation (CP) polarisation converter have been proposed: a) based on periodically cascading 2 dielectric media (chapter 2) and b) based on periodically cascading a GRIN media (chapter 3). The latter allow up to 70% lateral size reduction compared to those in chapter 2, without compromising the realised Axial Ratio (AR), bandwidth and Insertion Loss (IL). Several techniques are currently available for fabricating such GRIN waveplates, among which only the index discretisation has been explored here. Future work shall focus on exploring other manufacturing alternatives (e.g. additive manufacturing [W1]). Likewise, the utilisation of asymmetric GRIN profiles may be particularly interesting since they would ease integrating the waveplates with other devices, such as dielectric lenses.

A report of the experimental results of a) was published in [J1, C1], whilst the analytical and numerical results of b) were published in [J3]. The limitation of the single layered structures comes in the form of a limited bandwidth; this was addressed by combining several waveplates with tailored values of thickness and relative rotations. We reported a novel structure proving a 2-fold bandwidth broadening. The proposed design and its corresponding experimental results are being prepared for publication in [J2]. Similar multilayer solutions may be adopted for obtaining different frequency responses to those explored here, e.g. dual- or multi-band. Likewise, the proposed analytical models may be extended to account for off-normal wave propagation providing a straightforward tool for the evaluation of the angular sta-

bility. Additionally, the waveplates can be easily modified to operate in reflection by the introduction of a Ground Plane (GP), which is particularly interesting for their integration with reflector antennas.

The proposed LP-to-CP polarisation converter was conformed onto half of the surface of a discretised hemispherical LL. The system has proved to offer high directivity, high polarisation purity, low SLL and compactness within the 26.5–40 GHz frequency range (AR $<$ 3 dB). The results included in the initial study reported in this thesis suggest that this type of integrated antennas are a promising alternative to current CP reflectors and will be the focus of a future publication [J4]. Further investigations in this respect may be of high interest.

The second part of this dissertation consists of three chapters comprising a detailed analysis of the spectral response of nm-scale particles arranged in a 2D planar configuration. The principles used to design mm-scale structures have been revisited to account for the fundamental differences caused by the change in the electromagnetic response of metals at Near Infrared (NIR) frequencies (e.g. losses, field penetration and Surface Plasmon Polaritons (SPPs)). The studies presented here were primarily driven by the current demand to increase/control the radiation of optical sources. In this context, chapter 4 serves as a guideline to introduce a novel LW nano-antenna whose response is not bound to plasmonic effects, whereas chapters 5-6 present fundamental investigations that may contribute towards setting up the basics of future nano-antenna designs.

In this sense, in chapter 4, a novel Fabry-Pérot (FP) LW nano-antenna was demonstrated through numerical simulations combined with the reciprocity theorem. The proposed nano-antenna has been miniaturised to operate in the NIR. Of particular importance in the design process were the reduction in cavity height and the specific response of the PRS, which may exhibit bands of minimum reflectivity. These band-scan significantly degrades the performance of the nano-antenna. Depending on the polarisation of the source, our study has identified the plasmonic Brewster's angle and the excitation of Edge Plasmons (EPs) as being ultimately responsible for this unwanted effect. Appropriate considerations can be taken during the synthesis process to avoid this issue. In preparation for a practical realisation, we also investigated effects coming from asymmetric dielectric environments. The designed LW nano-antenna still offers a good performance in this scenario. These results are

intended to provide guidelines for frequency tuning the nano-antenna in preparation for its integration with real optical sources (e.g. quantum dots). The results of this study were published in conference [C3] and journal [J5].

Driven by the abnormal response of the PRS reported in chapter 4, the electromagnetic properties of plasmonic nano-particle gratings were further investigated in chapter 5. There, the Localised Surface Plasmons (LSPs) supported by nano-rods, nano-disks and nano-rings were considered. Despite there are numerous studies dealing with the plasmonic response of such nano-particles, most of them focus on isolated elements or limit to normal incident light excitation [1–4]. Our results indicated that the symmetry breaking introduced by off-normal illumination and/or the presence of the lattice are key mechanisms for light coupling to certain modes. Three different types of LSPs dominating the electromagnetic response of the arrays were identified: a) cavity modes related to waveguide modes, b) EPs highly concentrated to the nano-particles' ridges and c) FP modes. The latter are particularly important since they can produce very high electric and magnetic field enhancements (strongly resembling magnetic loop antennas), a sought-after feature in optics, where typical materials are magnetically inactive. Initial results of b) were reported in conference [C4], and a more detailed analysis has been recently submitted for its publication in [J6]. The results of c) were featured in journal [J7].

In chapter 6, our study was extended to analyse the electromagnetic response of individual nano-holes and 2D hole-arrays. Depending on their degree of localisation, two different types of modes were identified: a) EP-Whispering Gallery Modes (WGMs) showing a close relation with nano-disks EPs analysed in chapter 5; and b) propagating SPPs enabled by the connecting metallic film. EP-WGMs were shown to strongly dominate the scattering properties of hole-arrays. For instance, they allowed us to re-interpret previous experimental results found in metamaterials. The potential applications investigated included zero-transmittance absorbers and high performance sensors.

Propagating SPPs supported by thin metallic films, as those considered in this thesis, hybridize in Long Range (LR-) and Short Range (SR-)SPPs. Whereas an analytical solution for solving the dispersion relation of LR-SPPs is available in [5], in the case of SR-SPPs, it had to be solved numerically. We extended that work by deriving a simple and accurate approximated closed-form for rapidly solving the

relation dispersion of SR-SPPs with the aim of easing the design of future SR-SPPs based devices. The validity range of the assumptions used throughout the derivation was also studied and discussed. Comparison with numerical simulations suggested that the proposed closed-form provides an accurate and fast tool for calculating the frequencies at which light couples to SR-SPPs supported by a 2D array of sub-wavelength holes. A report of the results of a) has been submitted to journal [J8], whilst the derivation of the closed-form of the SR-SPPs dispersion relation was published in [J9].

Overall the results of this thesis have been well embraced by the scientific community, as evidenced by the 5 peer-reviewed journal publications in IEEE Wireless and Microwave Component Letters, IEEE Photonics Journal, Nano Letters and Applied Physics Letters, together with the 4 peer-review international conferences in the frame of metamaterials and antennas.

7.1 Future work

To conclude, several areas of this thesis into which further studies may be promising for the development of high frequency antenna systems are summarised.

7.1.1 All-dielectric gratings for mm-wave applications

The all-dielectric form-birefringent waveplates presented in this thesis (chapter 2) were designed to operate solely in transmission. Nonetheless, the use of reflector antennas, where energy radiated by a feed (e.g. a horn) is focused and redirected by a reflecting surface, is very common for long range communications, as they can offer medium to high directivity values. Metal-based polarisation converters operating in reflection, enabling their integration with reflecting surfaces, can be found in the literature. A comparison of some of these designs with our all-dielectric form-birefringent waveplates was given earlier in this thesis. It has been stressed that, depending on the specifications of each particular application, the use of metallic or all-dielectric polarisation converters may be desirable. Nonetheless, a third alternative that has not been investigated to date is the modification of our form-birefringent all-dielectric waveplates to include a ground plane so that they can

operate in reflection. To this end, extending the analytical models presented here, would be of particular interest.

Regarding the use of gradient index materials for circularly polarised antennas (chapter 3), the two structures reported, namely a compact gradient index linear-to-circular polarisation converter and a circularly polarised Luneburgh lens, have yet to be realised experimentally. In preparation for this, the discretisation of both the waveplate and the lens has been considered in this thesis. A different approach which may ease fabricating such devices would consist in 3D printing the structures. A gradual index distribution could be obtained by drilling, or directly 3D printing, a lattice of empty holes on the dielectric so that the effective index of the material would be proportional to the filling fraction. Spatially varying the filling fraction could be achieved by simply changing the radius of the holes or the period of the lattice. Investigating further in this direction may be promising.

7.1.2 Metallic grating for nm-wave applications

The performance of the leaky-wave nano-antenna reported in chapter 4 was only validated numerically. Special emphasis was made on the effect that varying its geometrical features has on the antenna performance, with the aim of providing guidelines for frequency tuning the nano-antenna to other operating frequencies in preparation for an experimental realisation. To this end, the next step would be adapting the antenna to available optical sources, e.g. group III-IV quantum dots or vacancy centre defects on diamond.

As per the arrays of nano-particles and complementary hole-arrays (chapters 5 and 6), it would be of most interest to analyse in further detail the role of the lattice in enabling/disabling certain localised surface plasmon modes. Having a theoretical framework describing the interaction in between lattice and unit-cell symmetries would allow us to make accurate predictions on light coupling to those modes, and hence on the electromagnetic response of the arrays. This is not to say that there are not other areas that could be explored further, e.g. regarding the application of the hole-arrays as sensors or absorbers; nonetheless, due to its wider applicability and generality, the author is of the opinion that such a theoretical model would be of particular relevance.

References

[1] Y. B. Zheng, B. K. Juluri, X. Mao, T. R. Walker, and T. J. Huang, "Systematic investigation of localized surface plasmon resonance of long-range ordered Au nanodisk arrays," *Journal of Applied Physics*, vol. 103, no. 1, p. 014308, 2008.

[2] G. X. Du, T. Mori, M. Suzuki, S. Saito, H. Fukuda, and M. Takahashi, "Evidence of localized surface plasmon enhanced magneto-optical effect in nanodisk array," *Applied Physics Letters*, vol. 96, no. 8, p. 081915, 2010.

[3] F.-P. Schmidt, H. Ditlbacher, U. Hohenester, A. Hohenau, F. Hofer, and J. R. Krenn, "Universal dispersion of surface plasmons in flat nanostructures," *Nat. Commun.*, vol. 5, p. 3604, 2014.

[4] W. Wan, W. Zheng, Y. Chen, and Z. Liu, "From fano-like interference to superscattering with a single metallic nanodisk," *Nanoscale*, vol. 6, pp. 9093–9102, 2014.

[5] F. Yang, J. Sambles, and G. Bradberry, "Long-range surface modes supported by thin films," *Phys. Rev. B*, vol. 44, no. 11, 1991.